QUANTITATIVE NMR STUDIES OF PERFUSED BRAIN SLICES

By

JONATHAN D. BUI

A DISSERTATION PRESENTED TO THE GRADUATE SCHOOL
OF THE UNIVERSITY OF FLORIDA IN PARTIAL FULFILLMENT
OF THE REQUIREMENTS FOR THE DEGREE OF
DOCTOR OF PHILOSOPHY

UNIVERSITY OF FLORIDA

2000

ACKNOWLEDGMENTS

Even for someone who has owed so much to so many, it is not difficult to single out Professor M. Ian Phillips for his unwavering support, guidance, and tremendous patience over the past decade. He is not only chair of my supervisory committee but is also a father and mentor who has steadfastly stood by my side, unselfishly encouraging me to follow my passions. I owe Prof. Phillips more then I can ever convey in words or in action. Dr Stephen J. Blackband serves as co-chair of my committee, sharing his expertise in NMR microscopy and teaching me a great deal about science; Steve has yet to succeed in teaching me to play snooker! Many thanks Steve – very much for everything. I am very grateful to Prof. Colin Sumners for his support and encouragement over the years; in fact, it was his lecture more than a decade ago that first gave me the notion that one could make a living as a scientist – asking questions of nature. Dr Thomas H. Mareci introduced me to NMR and gave me a second home in his laboratory; I appreciate Tom's down to earth perspective on life and his many kind efforts on my behalf. I worked in Dr Edwin M. Meyer's laboratory while a medical student and Dr Meyer provided an opportunity to combine molecular biology with behavioral studies; I shall always remember the hours spent with the Morris water maze. I am indebted to him for his encouragement, support and friendship. Thanks also to Dr Douglas K. Anderson for his support and guidance; he was an original member of the thesis committee and would still be were it not for red tape and paper work mix-up.

I should also like to recognise Dr David L Buckley – my partner in crime who made the many long hours at the magnet very enjoyable! I thank Dr Tibor Zelles for his friendship and help with the brain slice preparation.

Thanks also to my friends in various laboratories including Birgitta Kimura, Robert Gyurko, Ben Inglis, Clare Zhang, Cecile Mohr, Alan Freeman, Beth Bossart, David Hogarty, Liz Speakman, Xeve Silver, Dia Nammari, Emma Mercer, Sam Wang, Leipeng Sheng, Craig Meyers, Zaher Elmer and Shamir Shahi. I owe you all very much; space limitations prevent me from the page long acknowledgement which each of you so deserve. I also thank Dr Sara Galli and Dr David Evans for their support. Many thanks also go to Dr Weihong Tan for his friendship and for introducing me to the fascinating field of near-field optics.

Sincere gratitude must go to the late Professors Melvin Fregly and Heinz Eichhorn for their support, insight, and lessons over the years. Many thanks also to Professors Arthur Otis, Sid Cassin, and Raymond Andrew for their wise council and insights into the history of science.

My family, especially my parents, has shown unbelievable patience with a very difficult son; thank you for your unconditional love.

Any acknowledgement section will inevitably be incomplete. For those dear friends, family and mentors whose names have not been mentioned here, please know that you are in my thoughts and have not been forgotten.

I should like to close by dedicating to Prof Phillips and Dr Blackband the following quote by Sir Hans Krebs:

"Scientists aren't so much born as are made by those who teach them research."

TABLE OF CONTENTS

ACKOWLEDGEMENTS ii

ABSTRACT vi

CHAPTERS

1 INTRODUCTION 1

2 NUCLEAR MAGNETIC RESONANCE 4

- Nuclear Spin 5
- RF Excitation 10
- The Bloch Equations 11
- Relaxation Mechanisms 13
- The spin echo 15
- The Inversion Recovery 16
- NMR Imaging 17
- Water Diffusion 24

3 CEREBRAL ISCHEMIA, CELL SWELLING AND THE BRAIN SLICE PREPARATION 30

- Cerebral Ischemia and Stroke 30
- Cell Swelling 32
- Brain Slice Preparation 35
- Results 39
- Discussion 39

4 EFFECT OF TONICITY CHALLENGES ON WATER DIFFUSION AND CELL VOLUME IN PERFUSED HIPPOCAMPAL SLICES 43

- Introduction 43
- Methods 43
- Results 47
- Discussion 49
- Conclusions 54

5 EFFECT OF OUABAIN ON WATER DIFFUSION IN THE PERFUSED HIPPOCAMPAL SLICE 55

- Introduction 55
- Methods 57

Results 61
Discussion 65

6 THE EFFECT OF NMDA INDUCED EXCITOTOXICITY ON WATER DIFFUSION IN THE PERFUSED HIPPOCAMPAL SLICE 74

Introduction 74
Experimental Procedure 77
Results 79
Discussion 81

7 GADODIAMIDE ENHANCED NMR IMAGING MEASUREMENT OF INTRACELLULAR VOLUME IN THE PERFUSED HIPPOCAMPAL SLICE 86

Introduction 86
Materials and Methods 87
Results 91
Discussion 94

8 COMPARTMENTAL WATER DIFFUSION IN PERFUSED HEART SLICES 99

Introduction 99
Materials and Methods 101
Results 104
Discussion 107

9 WATER DIFFUSION MEASUREMENTS IN A MIDDLE CEREBRAL ARTERY OCCLUSION MODEL OF FOCAL ISCHEMIA 113

Introduction 113
Materials and Methods 114
Results 119
Discussion 121

10 CONCLUSIONS 127

REFERENCES 130

CURRICULUM VITAE 138

BIOGRAPHICAL SKETCH 142

Abstract of Dissertation Presented to the Graduate School
of the University of Florida in Partial Fulfillment of the
Requirements for the Degree of Doctor of Philosophy

QUANTITATIVE NMR STUDIES OF PERFUSED BRAIN SLICES

By

Jonathan D. Bui

August 2000

Chair: M. Ian Phillips
Cochair: Stephen J. Blackband
Major Department: Physiology

Nuclear magnetic resonance (NMR) imaging adds greatly to the diagnosis of soft tissue diseases. However, diagnostic MR imaging is still largely dependent upon the physician's clinical impressions based on qualitative NMR signal changes. We believe that a quantitative understanding of the physiological basis for clinically observed NMR signals will provide the information necessary to link signal changes to specific disease processes. A quantitative understanding of MR signals requires understanding of the cellular basis for these signals. The work herein utilizes high field NMR imaging to quantitatively study the origins of NMR contrast in biological tissue, particularly water diffusion behavior in the central nervous system following various physiological stressors using an isolated perfused brain slice preparation. The results indicate that the relative sizes of tissue water compartments change with physiologic/pharmacologic challenges but the individual apparent diffusion coefficients (ADC) of the water compartments do not change. These data help to characterize the underlying mechanisms for ADC changes seen in clinical MR imaging following such neuropathological insults as ischemic stroke. This work describes the construction of a tissue slice perfusion chamber fitting into a standard 10mm NMR tube for experiments done on a 14.1 Tesla narrow bore magnet. It reports for the first time high resolution NMR microimages of isolated hippocampal slices with anatomic architecture discernable at 15 μm resolution. Furthermore, with adequate perfusion the slices could be maintained for physiologically relevant studies. Initial experiments with 20% tonicity challenges indicated that diffusion weighted NMR imaging was sensitive to these changes. Subsequently, quantitative diffusion measurements revealed a bi-exponential water diffusion behavior in the slices with fast and slow diffusing components. Furthermore, after ouabain blockade of the Na+/K+ ATPase and NMDA excitotoxicity, there was a significant change in the relative sizes of the water compartments but the individual apparent diffusion coefficients remained constant. The change in compartment sizes is consistent with cytotoxic edema seen following ischemic stroke or ouabain and NMDA induced toxicity. Experiments using gadodiamide enhanced NMR imaging provided another way to measure cell volume sizes. Following a hypertonic perturbation, the changes observed with gadodiamide enhanced imaging were consistent with those measured with diffusion NMR. Experiments on heart slices also revealed bi-exponential water diffusion. These experiments provide added confidence that the fast and slow diffusing components represent true physiological water compartments. Finally, *in vivo* experiments in a middle cerebral artery (MCA) occlusion model indicate that following focal ischemia the average water ADC decreases in a fashion that may be explained mechanistically by compartmental changes as measured in the perfused slice preparation. The data collected thus far have been useful in interpreting ADC measurements made in the clinical setting. We anticipate that the brain slice model will contribute to the development of quantitative models that, in turn, will support the examination of a variety of neurological disease states.

CHAPTER 1
INTRODUCTION

The work presented in this dissertation describes the development of an isolated perfused brain slice preparation for NMR imaging studies. This preparation is then utilized to study the origins of NMR contrast in biological tissue. NMR imaging has become an important part of the clinical armamentarium and yet, the origins of NMR contrast *in situ* are not fully understood. Recent developments in high-resolution NMR imaging provide an opportunity to make detailed quantitative studies of the cellular basis for NMR tissue contrast. The rationale for the studies presented herein is that a better understanding of the physiological basis for clinically observed NMR signals will provide the information necessary to link NMR signal changes to specific disease processes. Previous studies with NMR microscopy on isolated perfused cells revealed significant differences in the NMR characteristics of cell nucleus and cytoplasm. An inherent limitation of single cell studies is the absence of a realistic extracellular space.

In order to provide a physiological extracellular space and thus, bridge the gap between single cell studies and *in vivo* clinical MR imaging, an isolated perfused brain slice preparation was developed and optimized for NMR microimaging studies. The hippocampal slice was chosen over other slice preparations as it has been extensively examined, especially in the field of cerebral ischemia and stroke. Moreover, its characteristic structure and size are well suited for high field NMR microimaging experiments. This dissertation describes quantitative measurements of water diffusion and cellular compartmental changes with an emphasis on the pathophysiological changes occurring during the development of ischemic stroke.

Chapter 2 is a brief description of nuclear magnetic resonance theory, focusing on topics essential for interpretation of the data presented herein. It begins with the basic concepts of spin, nuclear inductance and relaxation mechanisms. This is followed by a description of NMR imaging. Finally, it closes with a discussion of water diffusion and considers the Stejskal-Tanner diffusion sensitization technique widely used in NMR.

Chapter 3 reviews the brain slice preparation and describes the construction of a perfusion chamber for NMR microimaging studies. It ends with baseline brain slice viability experiments.

In chapter 4, we use NMR microscopy to study the hippocampal brain slice preparation described in chapter 3. It describes the first study of perfused brain slices using NMR microscopy and moves on to indicate that upon 20% tonicity change, there were significant changes in the diffusion weighted NMR signal.

Subsequently, the first quantitative measurements of water diffusion in brain slices with high resolution NMR imaging were carried out which showed that they exhibit bi-exponential diffusion behavior (chapter 5). Further, after ouabain induced cell swelling, the diffusion coefficients of the compartments remain constant but the relative fractions change.

As the glutamate NMDA receptor is shown to be a component of ischemic cell injury, we studied the effects of NMDA on the perfused hippocampal slice and measured compartmental ADCs (chapter 6). The NMDA receptor antagonist, MK-801, attenuated the effects of NMDA on water diffusion.

In order to complement compartmental size measurements done with quantitative diffusion weighted NMR imaging, chapter 7 describes another method to measure cell volume using gadolinium enhanced dynamic imaging. The two methods are in good agreement. We also reported cell volume changes after the addition of 60mM mannitol (a 20% tonicity increase).

To further extend the utility of the brain slice model and provide further evidence of the origins of bi-exponential water diffusion, quantitative diffusion measurements of myocardial slices and isolated perfused heart preparations are described (chapter 8) The results indicate that like brain, the heart exhibits bi-exponential water diffusion. Furthermore, diffusion anisotropy may be appreciated with diffusion tensor imaging.

Chapter 9 discusses related experiments on an *in vivo* animal model of focal ischemia. ADC measurements of animals with middle cerebral artery occlusion were carried out. The results are consistent with the interpretation afforded by previous single cell studies and the isolated perfused brain slice experiments described in the preceding chapters. We further applied diffusion weighted and T2 weighted NMR imaging to study the potential neural protective effects of estrogen.

Chapter 10 summarizes the general conclusions of dissertation. We believe that the perfused brain slice model represents a novel way to study *in vivo* NMR signal changes at the cellular level and may also be applied to study cellular responses to various neurological challenges, particularly neurovascular insults. A quantitative understanding of NMR signals requires understanding of the cellular basis for these signals and future studies will aim to construct a model of tissue contrast to include intracellular, intranuclear, and extracellular contributions to D, T1 and T2.

CHAPTER 2
NUCLEAR MAGNETIC RESONANCE

The phenomenon of nuclear magnetic resonance (NMR) has been extensively considered in the literature (Andrew, 1956; Slichter, 1989) and thus, this chapter describes only the basic concepts of NMR, emphasizing those particularly relevant for interpretation of the results presented in subsequent chapters.

NMR was first observed by Rabi et al. (1939) in molecular beams and subsequently observed in bulk matter at the end of 1945 independently by Bloch et al. (1946) and Purcell et al. (1946). The discovery of NMR in bulk matter provided a new method to study nuclear properties, which resulted in a shared Nobel Prize in 1952 for Bloch and Purcell. In the early 1950s, chemical shifts and coupling were discovered and NMR rapidly became important in chemistry for molecular structural determination. In 1971 Damadian (1971) suggested the use of NMR for tumor detection based on his finding that cancerous and normal tissues had different NMR characteristics. Shortly thereafter, NMR imaging was developed through the pioneering experiments of Mansfield (Mansfield, Grannell, 1973) on NMR diffraction and Lauterbur (1973) on NMR zeumatography, both employing linear field gradients to spatially encode information. The first *in vivo* human NMR image was achieved in 1976 (Mansfield, 1977). Currently, NMR imaging has been established as an essential addition to the modern diagnostic armamentarium.

NMR phenomena is rooted at the atomic nucleus level and so a discussion of NMR necessarily begins with the concept of nuclear spin and spin behavior in a magnetic field.

Nuclear Spin

Atomic nuclei consist of charged protons and non-charged neutrons, known together as nucleons, each with spin numbers ½. The sum of nucleons in a nucleus is defined as the mass number A; the number of protons determines the electric charge number Z of the nucleus. Nuclei with non-zero spin can be induced to exhibit NMR phenomenon. When both A and Z are even, the nucleus of interest has a zero spin quantum number, I=0, and thus no net angular momentum, rendering it incapable of exhibiting NMR. In biological samples, there are several relevant nuclei with spin such as ^{1}H, ^{31}P, ^{23}Na. ^{1}H NMR is widely used in biological systems because of its high physiological concentration, which is on the order of 50 molar. The ^{1}H nucleus contains a single proton and hence I=1/2. Experiments described herein are all based on ^{1}H NMR.

The properties of nuclear spin and magnetic moment were first described by Pauli (1924) to account for the hyperfine structure of atomic spectra. Since then, it is well recognized that certain atomic nuclei possess non-zero nuclear spin or intrinsic angular momentum, **J**, with magnitude:

$$|J| = \sqrt{I(I+1)}\hbar \qquad [2.1]$$

where I is the spin quantum number and $\hbar$ is planck's constant h divided by 2π. Note that vectors are represented with bold font. The angular momentum **J** has 2I+1 possible projections onto an arbitrary z axis. The z component of **J**, denoted J_z, can be described as:

$$J_z = m\hbar \qquad [2.2]$$

where m is the magnetic quantum number with 2I+1 eigenvalues in integral steps between +I and –I. Thus, there is a space quantization, where only certain orientations of **J** are possible.

Since atomic nuclei have charge, by Faraday's Law of electromagnetism, a spinning nucleus generates a minute magnetic field called the magnetic moment, μ, which is proportional to **J**, given by:

$$\mu = -\frac{e}{2m_p}\mathbf{J} \qquad [2.3]$$

where m_p is the mass of the proton. The μ has random directions in the absence of an external magnetic field. Note that since the proton has a much larger mass than an electron, nuclear magnetic moments are much smaller than the magnetic moments of electrons. The relationship between μ and **J** also defines a nucleus specific constant known as the gyromagnetic ratio which is:

$$\gamma = \frac{\boldsymbol{\mu}}{\mathbf{J}} \qquad [2.4]$$

Spin Behavior in a Magnetic Field

When a nucleus with magnetic moment, μ, *and* spin I is placed in a magnetic induction field, **B,** it may reside in certain allowed eigenstates with (2I+1) eigenvalues given by:

$$\mu_z = -\frac{e\hbar}{2m_p}m = -\mu_B m \qquad [2.5]$$

where μ_z is the magnetic moment along z and μ_B is defined as the Bohr magneton. The energy of μ is quantized and given by the scalar product of the two vectors:

$$E = -\mu\mathbf{B} \qquad [2.6]$$

In a strong magnetic field, the axis z coincides with the field direction such that E can be written as:

$$E = -\mu_z B \qquad [2.7]$$

where B is the magnitude of the vector **B**.

From eqns 2.2 and 2.4, E can be rearranged as follows:

$$E = -m\hbar\gamma B \qquad [2.8]$$

The gap between adjacent Zeeman energy states is $\hbar\gamma B$ and since the selection rule for NMR is $\Delta m = \pm 1$, the resonance condition given by Planck's equation is:

$$\Delta E = h\nu = \hbar\gamma B \qquad [2.9]$$

Solving for ν we arrive at:

$$\nu = \frac{\gamma B}{2\pi} \qquad [2.10]$$

Spin behavior may be described also using classical mechanics, leading to an equivalent expression. When μ is placed in an external magnetic field it experiences a torque τ:

$$\tau = \gamma \times \mathbf{B} \qquad [2.11]$$

aligning it with the field such that it precesses about the field. This precessional frequency, ω, is proportional to the applied field **B**, as described by the classical Larmor equation:

$$\omega = \gamma B \qquad [2.12]$$

where ω is in radians and given by $\omega = 2\pi\nu$. The Larmor equation is equivalent to the frequency equation 2.10 described above.

As discussed previously, experiments described herein are based on ^{1}H NMR and thus we focus our subsequent discussion on the ^{1}H nucleus. The ^{1}H nucleus with a single proton and I = $^{1}/_{2}$ may exist in one of two states in an external magnetic field. It may be in the lower energy "spin-up" state, aligned parallel with the field, corresponding to the eigenvalue $m = +^{1}/_{2}$ with energy given by:

$$E = -\frac{\gamma\hbar B}{2} \qquad [2.13]$$

Or it may exist in the higher energy "spin-down" state, anti-parallel to the field, corresponding to $m = -^{1}/_{2}$ with energy given by:

$$E = \frac{\gamma\hbar B}{2} \qquad [2.14]$$

The energy difference between the two spin states is a linear function of the magnetic field B:

$$\Delta E = \gamma\hbar B \qquad [2.15]$$

Transitions from the spin-up state to the spin-down state occur when the sample absorbs a photon with energy equal to this energy difference. At absolute zero, all spins in a sample would align with the magnetic field, but as the temperature increases, a larger proportion of spins may exist in the higher energy spin-down state. The ratio of these populations is given by the Boltzmann ratio:

$$\frac{n_-}{n_+} = e^{\frac{-\gamma\hbar B}{kT}} \qquad [2.16]$$

where n_+ and n_- are the total number of spins aligned with and against the field respectively. At room temperature there will be a small net excess of spins aligned with the field. This fraction of spins aligned with the field results in a net macroscopic magnetization, ***M***, which has angular momentum described by the Bloch equations.

RF Excitation

Since nuclear magnetic moments precess about an external field at the Larmor frequency as described by eqn. 2.10, it is convenient to describe ensemble spin behavior in a frame of reference rotating at the Larmor frequency. As indicated above, when spins, for example in a biological sample, are placed within an external magnetic field, $\mathbf{B}_0$, the spins align with $\mathbf{B}_0$ resulting in a net macroscopic magnetization vector **M**. To observe NMR phenomenon, **M** is perturbed away from the main field $\mathbf{B}_0$ with a oscillating magnetic field $\mathbf{B}_1$ generated by a radiofrequency (RF) excitation pulse at the Larmor frequency of the nuclei of interest, thus resulting in absorption of photons as described by eqn. 2.15 and resonance occurs. With the addition of a fixed $\mathbf{B}_1$, **M** is rotated away from $\mathbf{B}_0$ at some tip angle alpha given by,

$$\alpha = \gamma \mathbf{B}_1 t_\alpha \qquad [2.17]$$

where $t\alpha$ is the duration that $\mathbf{B}_1$ is on.

Application of a 90^0 or pi/2 pulse with respect to **B** results in complete flip of **M** onto the transverse plane. Through photon exchange between protons in the sample and electrons in the RF coil, an electromotive force (EMF) is induced within the RF coil used to excite the sample in the first place; so in this instance, the coil may be used to detect the NMR signal. The EMF results in current flow within the coil and is the origin of the NMR signal. This induced current decays away exponentially following the termination of the $\mathbf{B}_1$ field and is called the free induction decay (FID). The signal decays as the spins lose phase coherence due to spin-spin relaxation processes described later.

The Bloch Equations

In his early classical description of NMR, Bloch formulated a set of differential equations to characterize the motion of the bulk magnetization in an NMR experiment. These phenomenological equations adequately describe spin behavior in a sample where the spins minimally interact. The basic equation of motion describing the changes of **M** in an external magnetic field $\mathbf{B}_0$ is given by:

$$\frac{\partial \mathbf{M}}{\partial t} = \gamma \mathbf{M} \times \mathbf{B}_0 \qquad [2.18]$$

At equilibrium **M** will preferentially lie parallel to the direction of $\mathbf{B}_0$ which by convention is along the z axis with an amplitude M_0. As discussed previously, application of $\mathbf{B}_1$, rotates **M** away from $\mathbf{B}_0$, introducing a component of **M** in the transverse plane. $\mathbf{B}_1$ is generally a sinusoidally varying field of the form:

$$\mathbf{B}_1(t) = (B_1 \cos \omega t)x - (B_1 \sin \omega t)y \qquad [2.19]$$

After the application of the **B**$_1$ field, relaxation mechanisms begin to influence the motion of **M** as it recovers back to z and decays away from the transverse xy plane. M$_0$ regrows exponentially:

$$\frac{dM_z}{dt} = \frac{M_0 - M_z}{T_1} \qquad [2.20]$$

where T1 is the longitudinal relaxation time constant (The basis for T1 relaxation is discussed below). Likewise, the transverse components of **M**, M$_x$ and M$_y$ lose coherence and dephase at a rate determined by the transverse relaxation time constant T2:

$$\frac{dM_x}{dt} = \frac{-M_x}{T_2} \qquad [2.21]$$

$$\frac{dM_y}{dt} = \frac{-M_y}{T_2} \qquad [2.22]$$

The mechanisms for T2 relaxation are considered later. When relaxation processes are taken into account, the general equation describing the magnetization can be rewritten as:

$$\frac{dM_x}{dt} = \left(M_y B_o - M_z B_y\right) - \frac{M_x}{T_2} \qquad \text{where } B_y = (B_1 \sin \omega t) \qquad [2.23]$$

$$\frac{dM_y}{dt} = \left(M_z B_x - M_x B_o\right) - \frac{M_y}{T_2} \qquad \text{where } Bx = (B_1 \cos \omega t) \qquad [2.24]$$

$$\frac{dM_z}{dt} = \left(M_x B_y - M_y B_x\right) + \frac{M_0 - M_z}{T_1} \qquad [2.25]$$

Relaxation Mechanisms

As stated above, the exponential decay of the signal induced in the RF coil results from two principal nuclear spin relaxation mechanisms. Both mechanisms depend on magnetic interactions, particularly dipole-dipole interaction. Since spins in a sample are subject to molecular motion, these interactions are complicated. As spins translate, rotate and vibrate in solution magnetic interactions between individual spins fluctuate and each spin undergoes a different random walk, based on its collisions with other spins. Over sufficient time, Brownian tumbling processes distribute the spins randomly and the probability of finding a component of the random motion at a particular frequency is given by a spectral density function. Molecular motion may be characterized by a correlation time, τ_c, which is a quantitative measure of the rate of a molecular motion. The rotational τ_c is roughly the time for the root-mean-square deflection to be 1 radian or ~60°. At times much greater than τ_c, molecules would be completely randomized and 'memory' of the original position is lost, and at times much less than τ_c, most molecules are close to their original positions. When molecules tumble at the NMR frequency (i.e., the Larmor frequency) where $\tau_c=1/\omega$, then the spectral density function is at maximum.

Spin-lattice (or longitudinal) relaxation giving rise to the time constant T1 results from interaction with random fluctuating local fields which induce nuclei to flip amongst their available spin states. The rate of spin-lattice relaxation, $T1^{-1}$, is proportional to the spectral density function such that $T1^{-1}$ is fastest when molecules tumble at the NMR frequency so that $\omega\tau_c=1$. For molecules tumbling much faster (i.e., $\omega\tau_c<<<1$), relaxation rate decreases as tumbling rate increases. For molecules tumbling much slower (i.e., $\omega\tau_c>>>1$), the relaxation rate increases as tumbling rate increases. Spin-lattice relaxation is essentially a process of thermal energy loss. It couples spins to the motion of the molecules that carry them and thus, provides a way for the exchange of energy between the spin system and its surroundings, the lattice. Energy exchange during the relaxation process is transferred from or to the motions of the molecules and eventually equilibrates with the lattice. Since the lattice has a greater heat capacity than the spins, energy is lost from the spin system until equilibrium is restored and spins relax with an unmeasurably small change in the temperature of the sample. From the solution to eqn. 2.20 which defines T1, it can be shown that T1 in quantitative terms is the time for 1-1/e of M0 (or ~63%) to regrow back to z after cessation of the $\mathbf{B}_1$ field. By convention, a time at least 3T1 is required for the spin system to be considered fully relaxed along z.

Spin-spin (or transverse) relaxation with the characteristic time constant T2 results primarily from loss of spin phase coherence following a $\mathbf{B}_1$ pulse, giving rise to the NMR signal decay with time. Initially after excitation, all spins undergo precession at the Larmor frequency and are in phase with each other. However as spins in high and low energy states exchange states with each other due to spin-spin interactions, the signal decays as the spins dephase according T2 relaxation defined in eqn. 2.21 and 2.22. From the solutions to these equations, T2 may be defined as the time for the transverse magnetization to decay to 1/e (or 37%) of its original magnitude. As with T1, a time at least $3T_2$ since the application of the RF pulse is required for the system to be considered fully relaxed along the transverse xy plane. True T2 relaxation is therefore a result of spin phase dispersion due to energy exchange because of intrinsic field differences between adjacent spins either intra or intermolecularly. Furthermore, random molecular motion results in fluctuating fields as different spins come into contact with each other. The out of phase components interfere destructively resulting in further signal lost. In practice, the NMR signal decays much faster than expected from spin-

spin relaxation alone because of magnetic field inhomogeneities and is characterized by time constant T2* given by:

$$\frac{1}{T_2^*} = \frac{1}{T_2} + \left(\frac{\gamma \Delta B}{2} \right) \qquad [2.26]$$

where the second term is due to inhomogeneities in the static magnetic field. This decay is due to both true T2 relaxation and lost of phase coherence due to magnetic susceptibility and limitations with static field homogeneity. T2* relaxation may be responsible for significant reductions in the NMR signal especially in biological samples. Fortunately, the effects of T2* may be separated from true T2 relaxation through pulse sequence manipulations (e.g., the Hahn spin echo). In recent years, however, pulse sequences sensitive to T2* effects have gained popularity. Because of T2* relaxation's exquisite sensitivity to magnetic susceptibility, it has been utilized for functional magnetic resonance imaging experiments whereby neuronal activity is surmised to result in blood oxygenation level changes which may be detected with T2* sensitive NMR imaging techniques.

The Spin Echo

As discussed in the previous section, the effects of T2* can be separated from true T2 relaxation using a spin echo experiment first described by Erwin Hahn in 1950 (Hahn, 1950). In a spin echo experiment, a second signal or spin echo can be generated with the application of a second RF pulse following the initial excitation pulse. The time to echo (TE) designates the time from the initial pulse to the generation of a spin echo with TE/2 being the time of application of the rephasing second pulse. Although any pair of pulses will generate an echo, in practice at 90° (or $\pi/2$) excitation pulse followed by a 180° (or π) rephasing pulse is often used because it results in the strongest spin echo. The 90° pulse applied along x rotates **M** from the z axis onto the y axis. However, inevitable inhomgeneities in the static magnetic field $\mathbf{B_0}$ make individual dipoles precess at slightly different frequencies, based on local differences in the magnetic field strength. This results in lost of phase coherence and **M** fans out in the xy plane, reducing the transverse magnetization of the sample. When a 180° pulse is applied at time TE/2, the dipoles are flipped and realigned along symmetrical positions in the transverse plane (i.e., along –y). Precession continues for another time TE/2, when spins become perfectly in phase with one another and a spin echo results (at time TE). During this time TE, spin-spin relaxation processes still result in true T2 decay and the amplitude of the signal degrades at a rate 1/T2. This lost of phase coherence is due to random molecular motions (as described above) and is not refocused by the 180° pulse. This signal reduction during TE can be described:

$$S(TE) = S(0)\exp\left(\frac{-TE}{T_2}\right) \qquad [2.27]$$

where S is the signal amplitude. This relationship is can be used to measure T2 using a number of repeated experiments employing a range of TE values. T2 may be measured more quickly using a multi-echo sequence (e.g. a Carr-Purcell sequence), which employs a series of 180° pulses which results in generation of further echoes with increasing T2 decay.

The Inversion Recovery

The spin echo is a convenient way to measure T2, while T1 may be measured using the inversion recovery experiment. This experiment involves the application of a

180° inversion pulse followed by a standard 90° RF pulse to tip the magnetization onto the transverse xy plane (y axis). The inversion pulse tips the M from the positive z to the negative z direction. After a period designated the inversion time TI, spins in the negative z direction will recover back to the positive z direction according to T1 relaxation. Subsequently, a 90^0 pulse is applied to tip the recovered M onto the xy plane. A range of TIs may be used to map out the recovery of the inverted magnetization. With exponential relaxation, the longitudinal magnetization at time TI is :

$$M(TI) = Mo\left[1 - 2\exp\left(\frac{-TI}{T_2}\right)\right] \qquad [2.28]$$

NMR Imaging

Thus far, we have described the behavior of the NMR signal within the entire sample in a relatively uniform static magnetic field. In the early 1970s, investigators employed the use of non-uniform magnetic fields to spatially encode the NMR signal in 2 dimensions. The result is the birth of NMR imaging through early experiments on NMR diffraction and NMR zeumatography, both employing linear field gradients to spatially encode the signal. NMR imaging has developed rapidly since those early experiments and currently, 2-dimensional Fourier Transform (2D-FT) pulse field NMR imaging is widely used. The following is a brief description of imaging focusing on 2D-FT NMR imaging.

An NMR image is 2-dimensional representation of the NMR signal from the spins in a slice of particular thickness within the sample (selection of slice location and thickness will be discussed below). The image can be described by an array of nxn elements or pixels. Constructing an image thus requires measurement of the NMR signal from all n^2 pixels. The steps necessary to unambiguously determine the location of spins as a function of space using magnetic field gradients is described below.

The Magnetic Field Gradient

For imaging, the magnet is equipped with gradient coils, which can produce 3 orthogonal filed gradients. The field strength experienced by the sample in a linear field gradient will vary as a linear function of its position:

$$B = B_0 + G \cdot r \qquad [2.29]$$

where G is the gradient applied and r represents the location of spins of interest along the applied gradient. The gradients in 3 orthogonal directions are:

$$G_z = \frac{dB_z}{dz};\ G_x = \frac{dB_x}{dx};\ G_y = \frac{dB_y}{dy} \qquad [2.30]$$

A gradient in any direction can be attained through the simultaneous application of these 3 gradients which will change the effective field experienced by spins as a function of position. Thus, the precessional frequency of spins will be a function of position:

$$\omega = \gamma B \text{ or } \omega = \gamma\left(B_0 + G \cdot r\right) \qquad [2.31]$$

In order to construct a 2D image from linear field gradients, first a slice or thin slab of the sample must be selected; this is referred to as slice selection. Subsequently spins within the slice must be localized using frequency and phase encoding.

Slice Selection

A 2D slice may be selected by excitation of only those spins within a narrow section of the sample through the application of the slice select gradient G_z. If a spectrally-shaped RF pulse (e.g., a sinc pulse) is applied when this gradient is on then only a narrow range of frequencies is excited, representing a slab of some thickness. Thus, by changing the characteristics of the RF pulse, the position and thickness of the slice can be shifted along the gradient axis as follows:

$$\Delta z = \frac{\Delta\omega}{\gamma G_z} \qquad [2.32]$$

where Δz is the slice thickness and $\Delta\omega$ is the RF transmitter bandwidth. Therefore, if an RF pulse with a particular center frequency and bandwidth is applied, then only spins experiencing the appropriate effective magnetic field (along the gradient axis) will resonate in this frequency band according to the Larmor equation (eqn. 2.31). In this way, only a particular slice is excited and selected. Now, the application of gradients causes spins to dephase in addition to the dephasing due to relaxation discussed previously. In order to rephase gradient-induced loss of coherence, another gradient must be reapplied immediately following the RF pulse but in a negative sense. This principle can be extended to each imaging gradient contributing to signal generation to maintain phase coherence.

Frequency Encoding

With the slice selected, the signal within the selected 2D plane must be spatially encoded to form an image. Frequency encoding allows for spatial separation of spins in one of these dimensions using another gradient conventionally applied along the x-axis.

As mentioned previously, an image is composed of an array of nxn pixels in space which contain a fixed number of spins. Thus, the signal within each pixel is proportional to the spin density, ρ(x,y), within that pixel. Immediately following excitation, the signal from the sample is the sum of signal from individual pixels:

$$s(t) = \iint \rho(x,y)dxdy \tag{2.33}$$

This equation holds in the absence of relaxation. However, since T2 relaxation is occurring during this time, the equation can be modified to include a T2 decay exponential:

$$s(t) = e^{\frac{-t}{T_2}} \iint \rho(x,y)dxdy \tag{2.34}$$

Now in order to separate spins or pixels according to their spatial positions in one dimension, a gradient G_x must be applied which modifies the equation as follows:

$$s(t) = e^{\frac{-t}{T_2}} \iint \rho(x,y)e^{-i\gamma G_x xt}dxdy \tag{2.35}$$

This equation describes the signal as a function of time. To form a 1D image or profile, this time domain function can be transformed into frequency domain using the inverse FT of this equation. Inverse FT results in a one-dimensional spatial projection of the selected slice onto the x-axis. In older projection-reconstruction imaging algorithms, 1D projections at different angles, which traverse the sample in a polar coordinate system, is used and a 2D image can be reconstructed. However, the advent of 2D FT imaging, has made this technique obsolete.

Phase Encoding

Encoding the second in-plane dimension is not a trivial application of a second frequency-encoding gradient because the information obtained would not be unambiguous in space and so phase encoding becomes necessary. This is achieved using a third orthogonal gradient, the phase-encoding gradient, conventionally along the y axis. This introduces a second time dimension called "pseudo-time" and enables a 2D image to be generated using a 2D FT. This gradient is applied before the frequency-encoding gradient and imparts a phase shift on the signal. The equation above can now be rewritten to include the addition of phase-encoding:

$$s(t) = e^{\frac{-(t+t_y)}{T_2}} \iint \rho(x,y) e^{-i\gamma(G_x xt + G_y t_y y)} dxdy \qquad [2.36]$$

where G_y and t_y correspond to the amplitude and duration of the phase-encoding gradient respectively. By linearly incrementing the amplitude G_y with each excitation the signal can be sampled at a series of pseudo-time points with n_y phase encoding steps. Likewise, n_x frequency encoding steps or points are collected for each signal acquisition. This provides a 2 dimensionally encoded signal with an $n_x x n_y$ matrix:

$$s(n_x, n_y) = e^{\frac{-(n_x t+t_y)}{T_2}} \iint \rho(x,y) e^{-i\gamma(n_x G_x xt + n_y G_y t_y y)} dxdy \qquad [2.37]$$

This equation is commonly referred to as the imaging equation. Taking the inverse 2D FT of it will yield a 2D image; this type of imaging is called spin-warp imaging. A typical image may sample the echo with 256 points for each phase encode and 256 phase encoding steps, giving a 256x256 square matrix.

Retracing the steps necessary to generate an image, it is apparent that there are four steps involved. Here, a spin echo imaging sequence is discussed for illustrative purposes. First, slice selection is required which involves application of a 90° excitation pulse containing a specific band of frequencies in the presence of the slice select gradient, Gz. In the second step, as discussed above, gradient induced dephasing is corrected with an appropriate negative rephasing gradient. During this time, the phase encoding gradient Gy is also turned on. It is also here that a “dephasing” gradient is applied which is required to compensate for phase changes due to application of the frequency-encoding gradient. This gradient is positive because it occurs before the 180 refocusing pulse which is applied during the 3rd step. In the 4th step, an echo is generated at time TE (time to echo) which is sampled in the presence of the frequency encoding gradient, Gx. The total time requirement is called the repetition time TR.

k-Space

The imaging equation may also be stated in terms of k-space. The concept of k-space was first articulated in 1983 and is helpful in understanding the influence of gradients on the NMR signal in a graphical manner before Fourier transformation. It allows visualization of the data as a function of time. k-space may be thought of as having an inverse relationship to real space which is the domain of the image. In other words, the FT of k-space produces an image. Mathematically k is defined:

$$k(t) = \gamma \int G(t)dt \qquad [2.38]$$

where t is the duration that the gradient G is on. Therefore in terms of k, the imaging equation above can be written:

$$s(t) = e^{\frac{-(t+t_y)}{T_2}} \iint \rho(x,y) e^{-i(k_x(t)x + k_y(t)y)} dxdy \qquad [2.39]$$

Now writing this as a 2 dimensional function:

$$s(k_x, k_y) = e^{\frac{-(t+t_y)}{T_2}} \iint \rho(x,y) e^{-i(k_x x + k_y y)} dxdy \qquad [2.40]$$

The 2D FT of this equation is the image. Graphing the data in terms of k on a 2-dimensional grid yields information that is useful for development of pulse sequences. This is because it allows generation of appropriate k-space sampling schemes to be sensitive to object dependent parameters. For example, sampling the center of k-space would result in an image that is weighted towards general shapes and contours because it corresponds to low spatial frequencies. Conversely, data near the periphery of k-space would yield information about edges and details corresponding to high spatial frequencies. Which to sample is dependent on the detail required and the time allotted. It should be stated that each element in k-space does not directly correlate to a pixel within the NMR image. In fact, each k-space element contains information about every pixel within the image and each pixel contains information about every element in the k-space grid.

Water Diffusion

With the basic concepts of NMR imaging presented in the previous sections, it is now possible to consider translational water diffusion, which is central to the NMR experiments presented in this dissertation. *In vivo* proton NMR is essentially a measure of protons in water molecules since water is 50 molar and accounts for nearly all of the proton signal *in vivo*. It is therefore conceivable to design NMR experiments which are sensitive to translational water diffusion. The general expression for diffusion is Fick's second law of diffusion or the diffusion equation:

$$\frac{\partial c}{\partial t} = D\frac{\partial^2 c}{\partial x^2} \qquad [2.41]$$

where c is concentration, t time, x the displacement and D the diffusion coefficient. This equation states that the rate of change of concentration is proportional to the curvature or second derivative of the concentration with respect to distance. Solutions to eqn 2.41 yield exponential equations, which are useful in the determination of diffusion coefficients. For example, in the capillary technique the change of concentration of a solute within a capillary tube immersed in solvent is measured at a series of times. From the solution to eqn 2.41, D may be determined.

A successful technique to measure water diffusion with NMR was first described in 1965 by Stejskal and Tanner (1965). Stejskal and Tanner measured diffusion in liquids spectroscopically by applying a pair of diffusion gradients to the standard pulse gradient spin echo or Hahn echo. The addition of diffusion gradients sensitizes the Hahn echo to incoherent phase dispersion by random translational diffusion, resulting in signal intensity attenuation as described by the exponential equation:

$$S(b) = S_0 \exp(-bD) \qquad [2.42]$$

where S(b) is the measured signal intensity, S_0 is the signal intensity in the absence of diffusion weighting, b represents the integrated effect of all gradients upon the signal, and D is the apparent diffusion coefficient (ADC). In a standard Hahn echo experiment with matched diffusion gradients, b can be written (Stejskal, Tanner, 1965):

$$b = \gamma^2 G^2 \delta^2 (\Delta - \delta / 3) \qquad [2.43]$$

where γ is the gyromagnetic ratio, G is the amplitude and δ the duration of each gradient, and Δ is the time between the application of the two gradients. The period Δ - $\delta/3$ is referred to as the diffusion time, τ_D. The relationship described in eqn. 2.43 holds in a NMR spectroscopic experiment without imaging gradients. In the presence of imaging gradients, b is not a simple function as described in eqn. 2.43 but must include the effects of imaging gradients and cross terms. This is because imaging gradients, particularly large ones used herein, cause selective attenuation of fast diffusing spins. The degree of attenuation is a function of the duration and strengths of the slice-select and frequency encoding gradients. For single compartment diffusion, this is not a consideration. However, for multicompartment systems such as biological systems, this can significantly affect the measured diffusion coeficent, such that there is over representation of slow moving spins. Furthermore, there are cross terms between diffusion gradients and imaging gradients that influence signal decay rates. Cross term effects are particularly relevant in high resolution NMR imaging experiments where large imaging gradients are employed with relatively small diffusion gradients. Ignoring cross terms under these circumstances would result in overestimation of the diffusion coefficients (Neeman et al., 1990). To account for imaging gradient and cross term contributions to signal decay the diffusion factor b in eqn. 2.42 can be written as:

$$b = b_{st} + b_i + b_{ct} \qquad [2.44]$$

where b_{st} is the standard Stejskal-Tanner term, b_i the term contributed by imaging gradients and b_{ct} the contribution from cross terms. b_{st} is a function of G, δ, Δ as described in eqn 2.43, while b_i is dependent upon the magnitude and duration of the slice-select gradient and the frequency-encoding gradients. b_{ct} is a function of G, δ, Δ, and the amplitude and duration of the imaging gradient parallel to the diffusion gradients. To address these issues, the effects of all imaging gradients including cross terms were included in the calculation of b in the experiments described in this herein.

The self diffusion coefficient (D) described in the early experiments of Stejskal and Tanner has been replaced by the concept of apparent diffusion coefficient (ADC) when applied to biological systems since in these complex systems the measured D is a function not only of thermal molecular motion (Brownian motion), but may be dependent upon intracellular barriers, cellular streaming, and membrane permeability. Intracellular barriers to diffusion include intracellular components such as organelles, cytosketal structures, and macromolecules. Thus, diffusing spins in biological systems may experience both diffusion restrictions intracellularly and diffusion anisotropy with preferential diffusion in one or another direction. When considering restricted regimens, it is useful to consider the root mean squared displacement of a spin during the diffusion measurement. From the Einstein relation, it can be shown that:

$$\left\langle x^2 \right\rangle^{1/2} = \left(2D\tau_D\right)^{1/2} \qquad [2.45]$$

where the root mean squared displacement of a spin in the direction of the applied gradient is a function of the diffusion time τ_D and is a measure of the spread of spins. This is especially important when one considers diffusion at biological barriers such as cytoskeletal structures or biological membranes.

Multiexponential Diffusion

The monoexponential decay function characterized by eqn. 2.42, as indicated above, is valid when there is a single diffusing compartment. However, when there are multiple distinct diffusing species in a system, the observed signal attenuation may be given by a superposition of the contributions from individual diffusing populations:

$$S(b) = \sum_i f_i \exp(-bD_i) \qquad [2.46]$$

Biological systems present potential barriers to diffusion which may result in distinct populations of diffusing spins (water populations). However, limitations in gradient strengths have hindered dissection of these multiple diffusing compartments in the past. Monoexponential diffusion curves have been fitted to the data with relatively small b values (less than 1500 s/mm^2) (Moseley et al., 1990; Szafer et al., 1995a). The development of higher field magnets with stronger gradients has allowed investigators to achieve high b values which provide an opportunity to study the slower diffusing species. The higher the b value the greater sensitivity to slower diffusing spins, as the signal from the fast diffusing spins are completely attenuated. At these higher b values and short diffusion times, monoexponential equations cannot be adequately fitted to the data and a multiexponential analysis is warranted (Niendorf et al., 1996; Buckley et al., 1999; Bui et al., 1999). Conceptually, biological tissues (e.g., brain tissue) contain at least two diffusing compartments – intracellular and extracellular water compartments. There are also contributions from the nuclear and intravascular compartments; although these compartment comprise a small percent of the total water at least in brain and thus, will not be considered for simplicity. With two compartments, the signal attenuation measured is, thus, dependent upon the rate of water exchange between these compartments (Stanisz et al., 1997) and is related to the residence time within each compartment. In the limit of fast exchange, when the diffusion time, τ_D is much longer then the residence time (i.e. when all of the water molecules within a voxel have diffused through both compartments during τ_D), D can be written:

$$D = f_1 D_1 + f_2 D_2 \qquad [2.47]$$

and:

$$f_1 = 1 - f_2 \qquad [2.48]$$

where f_1 and f_2 are the volume fractions of the 2 compartments; in this case, 1 and 2 may represent intracellular and extracellular compartments. Similarly, D_1 and D_2 are the ADCs of water in each compartment. Therefore, in the fast exchange regime, signal decay is a monoexponential:

$$S(b) = S_0 \left[\exp - b(f_1 D_1 + f_2 D_2)\right] \qquad [2.49]$$

In the limit of slow exchange (when the water molecules remain in one or other of the compartments during τ_D), signal attenuation is a superposition of exponentials as described in eqn 2.46. In this case, a biexponential function:

$$S(b) = S_0\left[f_1 \exp(-bD_1) + f_2 \exp(-bD_2)\right] \qquad [2.50]$$

In most experimental designs, neither the fast nor slow exchange regime is encountered, but rather an intermediate condition. Kärger et al. (Kärger et al., 1988) have described an analytical solution for this condition. Unfortunately, the solution may be overparameterized without knowledge of either water exchange rates or compartmental ADCs (Pilatus et al., 1997). Although intermediate exchange regimes described by the Kärger model contain a greater number of unknowns, the solution is, like the slow exchange regime, a superposition of two exponentials. During intermediate exchange, however, the volume fractions and the diffusion rates are mixtures of the rates found in the short time limit due to the exchange of water between the two compartments (Kärger et al., 1988). Most experiments described herein employ a short diffusion time τ_D and approaches the slow exchange regime. Hence, ADC measurements are made fitting a biexponential as in eqn. 2.50 to the data.

CHAPTER 3
CEREBRAL ISCHEMIA, CELL SWELLING, AND THE BRAIN SLICE PREPARATION

This chapter considers the broad field of cerebral ischemia and stroke, particularly the mechanisms underlying ischemia induced cell damage. The resultant cell swelling which occurs secondary to energy failure is discussed. The utility of the brain slice preparation is also considered and modifications for NMR microimaging studies are described. The chapter ends with some preliminary NMR imaging studies of perfused hippocampal slices.

Cerebral Ischemia and Stroke

Stroke remains a major cause of death and disability in adults of industrialized countries. It is the third leading cause of death and the most common cause of adult disability with more than 500,000 new cases each year (Choi 1990; Choi and Rothman 1990). Approximately 85% of strokes are ischemic in nature (Mohr et al., 1978) and the majority result from acute focal ischemia. Global ischemia, for example, due to cardiac arrest is less common. Ischemic stroke is an irreversable neurological deficit which may arise from thrombosis or thromboembolism of extracranial and intracranial arteries or from emboli from the heart or nonatheroslerotic vasculopathies which may occlude flow within large vessels or small vessels of the brain. Occlusion of a major cerebral artery produces an immediate reduction in cerebral blood flow (CBF) to brain areas within its distribution. The ischemic core or center of the artery's territory has the greatest CBF reduction and ischemia becomes progressively less away from the core. The area where flow reduction is less severe has been termed the ischemic penumbra which is believed to be supplied from collateral branches of other vessels. Obviously, the severity and extent of ischemia induced deficits are dependent upon the degree and duration of CBF reduction. Hence, the ischemic core will be more heavily affected than the penumbra. Numerous therapeutic approaches have been aimed at rescuing the areas of brain within the penumbra (del Zoppo et at. 1997).

Cerebral ischemia induces a complicated pathophysiologic cascade within the highly susceptible CNS cells. These include expression of early immediate genes, heat shock proteins, cytokines and other mediators of acute necrosis. In addition, there is evidence that apoptosis or programmed cell death may play an important role in stroke and ishemia related cell injury. Thus, the mechanisms underlying ischemic brain damage are varied and the temporal course covers damage from minutes to hours to days (Choi 1990).

Energy failure

Reduction in CBF results initially in hypoxia and energy failure. Neurons become unable to maintain ionic gradients secondary to Na+/K+ ATPase failure, resulting in cytotoxic edema. Energy failure leads to free radical formation, increases in intracellular Ca2+, glutamate release, acidosis and derailments of other cellular processes (Choi and Rothman 1990). Currently, the working hypothesis incorporates glutamate excitotoxicity, Ca2+ overload and free radical damage. The view is that ischemia induced glutamate release activates excitatory amino acid receptors (particularly the NMDA receptor) resulting in cytosolic Ca2+ accumulation from both intra and extracellular stores. This results in a number of Ca2+ dependent cellular responses integral to ischemic cell injury. Among these include increases in fatty acid metabolism, resulting in formation of oxygen free radicals (Chan 1996). A shift to anaerobic glycolysis also results in lactic acidosis with pH in the range of 6.4 – 6.7 (Lascola and Kraig 1997). This further exacerbates ischemia induced cell damage. The cytokine mediated inflammatory reaction also injures the cell. Leukocytosis may cause microembolisation of small vascular beds (del zoppo et al., 1991). The inflammatory response also results in leaky vessels, producing a vasogenic edema. Following acute ischemic injury, there may be delayed cell injury associated with apoptosis as evidenced by DNA fragmentation (MacManus et al., 1995), and apoptosis related gene products are expressed following ischemia (Asahi et al., 1997). The mechanisms of cell injury in ischemia and stroke are complicated and their understanding is continually evolving.

Cell swelling

As discussed above, initially energy failure leads to an inability to maintain ionic gradients, which lead to cellular swelling or cytotoxic edema; the cells can no longer maintain a constant internal environment. Claude Bernard formulated the concept of homeostasis many years ago to describe the cell's ability to maintain a constant internal milieu despite fluctuations in the external environment (Bernard, 1865). In a simplistic sense, cells are a collection of anionic macromolecules enclosed by a semipermeable lipid bilayer, which has the ability to self-replicate. In addition, cells have developed energy dependent mechanisms to maintain a steady state away from Donnan equilibrium. Without these energy dependent mechanisms and selective permeability, cells would be in equilibrium such that the concentrations of permeable ions would equilibrate. However, for this to occur the cell would have to be a size such that the concentration of the impermeant anions is exceedingly small; in other words the cell would burst! Cells obviously have evolved mechanisms to prevent this type of Donnan swelling. Plant cells have a rigid cell wall, which effectively addresses this issue. Animal cells have evolved energy dependent pumps and selectively permeable membranes to maintain ionic gradients. The major pump is the Na/K ATPase which utilizes ATP to pump 3 Na+ ions out and 2 K+ ions inside the cell. Thus, this is an electrogenic pump, which contributes to the membrane potential. The extracellular Na+ is kept outside, preventing Donnan swelling. The cellular phospholipid bilayer itself is relatively impermeant to all ions but permeable to water. Selective permeability in cells came about with the incorporation of transmembrane ion channels which are ion specific. The animal cell is very permeable to K+ with open K+ channels while it is very impermeant to Na+ (Na+ channels are closed) under resting conditions. Hence, the cell membrane potential as described by Katz and others (Katz, 1966), is closest to the equilibrium potential for K+ as characterized by the Nersnt equation (Hille, 1992). In addition to the Na+/K+ ATPase, there are secondary active transport systems which are dependent upon the gradient created by selective permeability and the Na+/K+ ATPase which provide for uptake of substances such as glutamate and glucose. These systems are also important for maintaining cellular pH and Ca2+ concentration.

Under ischemic conditions, energy failure prevents proper functioning of the Na+/K+ ATPase leading to Na+ accumulation and derailments in the cellular concentrations of substances dependent upon Na+ gradients. This results in further cell swelling. For example, glutamate can induce cell swelling separate from the excitatory mechanisms discussed above by a purely co-transport mechanism (Lehre et al., 1995). Furthermore, ischemia induced compromises in pH balance may lead to cell swelling. Accumulation of CO2 in the face of decreased function of the Na+/K+ ATPase lead to activity of transport systems such as Cl-/HCO3 and Na+/H+ resulting in cell swelling as Na+ entry exceeds Na+/K+ ATPase ability to expel Na+. Finally, cell swelling may also result from hypoxia induced generation of free radicals and free fatty acids which cause breakdown of the selective permeability of the cell membrane as discussed above. Free radical formation may also contribute to vasogenic edema which occur later during ischemia by compromising the integrity of the blood-brain barrier.

Measurement of Cell Volume and Swelling

A number of techniques have been developed over the years to measure cell swelling since it is one of the earliest manifestations of energy failure and thus, ischemia-induced cell injury. Electron microscopy of ischemic cells reveal cell swelling and allow for an *in vitro* mesurement of cell volume (Van Harreveld and Fifkova 1971). However, the preparation may make quantitative interpretation difficult. Cell cultures have been studied using the Coulter Counter – a light scattering technique to measure cell volume (Olson et al., 1986). [^{14}C-]3-O-methylglucose (3-OMG) has frequently been used to measure astrocytic cell volume in culture (Martin and Shain 1979). Electrical impedance measurements under ischemic conditions reveal signficant increases in tissue impedance consistent with decreases in extracellular volume (Hossmann, 1974). Trimethylammonium (TMA+), an impermeant extracellular cation has also been used to measure extracellular space under various conditions (Nicholson and Sykova, 1998). TMA+ activity increases with ischemia consistent with a decrease in extracellular space. In recent years, diffusion sensitive NMR spectroscopy has allowed measurement of cell volume changes under ischemic conditions (Niendorf et al., 1996).

NMR Imaging and Cerebral Ischemia

Using diffusion weighted NMR imaging, Moseley et al. (1990) showed that cerebral ischemia is associated with a significant decrease in the apparent diffusion coefficient (ADC) of water. However, the mechanisms underlying this decrease in ADC is not fully understood and is topic of much debate in the literature. This dissertation provides data, which has helped to elucidate some of the underlying mechanisms for

ADC changes following ischemia, and stroke (which will be discussed in the chapters to follow). NMR microscopy on isolated perfused cells, has been utilized to study the basis for NMR constrast including ADC changes. Osmotic perturbation studies on isolated cells suggest that water redistribution contributes significantly to NMR signal intensity changes (Hsu et al., 1996). Since isolated cells lack a physiologic extracellular compartment, a brain slice preparation may serve to bridge the gap between previous work on isolated single neurons and clinical NMR imaging.

The hippocampal slice in particular has been extensively studied in the field of ischemia and stroke, which make it ideal for the diffusion measurements described herein. The information gathered may be applied with previous single cell and clinical ADC measurements to arrive at a quantitative understanding of the mechanisms underlying diffusion changes following cerebral ischemia and stroke.

Brain Slice Preparation

The brain slice model, pioneered by Henry McIlwain in the 1950s (McIlwain et al., 1951), is an established model to investigate numerous aspects of the cellular and molecular biology of the nervous system including neural structure, metabolism and function (Collingridge, 1995 and Aitken et al., 1995). It provides an accessible layer of tissue that is similar in many of its characteristics to intact brain which has afforded significant insights into the cellular basis of brain function. Brain slices have been examined using a variety of methods, including optical, radiological, electrochemical and histological techniques (Collingridge, 1995). Brain slices have also been examined collectively in a bath of using magnetic resonance spectroscopy (MRS) to study basic metabolism (Bachelard et al., 1994 and Pirttila, Kauppinen, 1994).

The hippocampal slice in particular has been extensively studied in the field of ischemia and stroke. Numerous cell volume measurements have been made on the slices (Nicholson and Sykova, 1998). Newman et. al. (1995) measured cell volumes in the hippocampal slice using a radiotracer (^{14}C-PEG) technique while Perez-Pinzon et. al. (1995) used an iontophoresis (TMA+) technique. These considerations make the hippocampal slice ideal for the diffusion measurements described herein.

These methods of measuring cell volume have yielded a better understanding of the processes that regulate cellular homeostasis. Furthermore, cell and molecular biology techniques applied to the brain slice preparation provide unrivaled details about the cellular basis of disease. The advantage of NMR over most other techniques is the possibility of extending measurements directly to the *in vivo* clinical setting in a noninvasive fashion. The information gathered maybe applied with previous single cell and clinical ADC measurements to arrive at a quantitative understanding of the mechanisms underlying diffusion changes following cerebral ischemia and stroke.

We believe that the perfused brain slice preparation represents a novel way to study *in vivo* NMR signal changes at the cellular level and may also be applied to study cellular responses to a variety of neuropathologies. In the following pages we describe the brain slice preparation and specific modifications for NMR imaging studies in isolated perfused hippocampal slices. Finally, initial baseline stability studies on perfused hippocampal slices are reported.

Sample Preparation and NMR Microscopy

Male Sprague-Dawley rats (150-200g) were anaesthetized with Metofane. Following decapitation, the brain was rapidly excised and placed into ice-cold artificial cerebrospinal fluid (aCSF in mM: 120 NaCl, 3 KCl, 10 glucose, 26 $NaHCO_3$, 2 $CaCl_2$, 1.5 KH_2PO_4, 1.4 $MgSO_4$), gassed with 95% O_2/5% CO_2, pH 7.4. The hippocampus was removed and sliced into 500 μm thick coronal sections with a McIlwain tissue chopper.

Perfusion Chamber Construction

A perfusion chamber was constructed from Delrin and consisted of a hollow cylindrical support arrangement consisting of three parts with a central ring holding the brain slice between gauze sections. The gauze sections were made of nylon monofilament with a 0.25 mm mesh opening. Input and output perfusion tubes were connected to a peristaltic pump. Two output tubes were used in the chamber to ensure that the magnet was not flooded. This construct was then placed in a 10 mm NMR tube and NMR measurements were carried out on a 14.1T magnet with a Varian Unity Console (Figure 3.1).

All experiments were carried out using a commercial Doty microimaging probe (Doty Scientific Inc.; Columbia, SC) interfaced to a Varian 600 MHz narrow bore instrument and Unity console (Varian Associates; Palo Alto, CA). Images were acquired at room temperature (18-19 ^{0}C) using a standard spin echo imaging sequence with diffusion gradient lobes placed on either side of the refocusing pulse.

To determine slice stability, hippocampal slices were monitored over an 8 hour period. Slices were placed in the perfusion chamber that was filled with isotonic aCSF. Images were acquired every 35 minutes (TR=3 s, TE= 22 ms, b=1000 s/mm^2 , 2 averages, resolution: 80 x 80 x 300 μm,). Signal intensity as a function of time was recorded. In separate experiments, 3 sets of images were acquired followed by a 5 minute perfusion of aCSF and this cycle repeated every 1.5 hours.

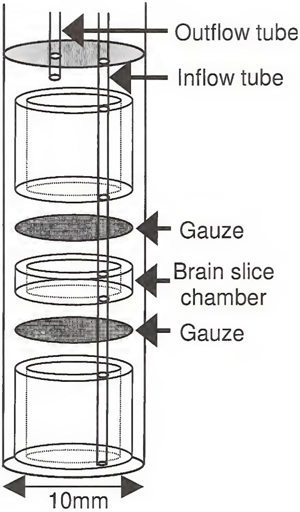

Figure 3.1 a. Brain slice perfusion chamber (expanded for illustration).

Results

NMR microimages have been collected at resolutions ranging from 15x15 μm to 120x230 μm in plane resolution. Figure 3.2a shows a high-resolution image acquired in 14 hours while figure 3.2b is a rapidly acquired image (4.3 minutes) used with live perfused brain slices.

Baseline stability studies were carried out. Thirteen hippocampal slices from 13 different rats were imaged over an 8 hour period each. The data show that signal intensity significantly increased as a function of time when the slices were bathed in aCSF without perfusion (n=7). Perfusion with aCSF for 5 minutes every 1.5 hours, resulted in stable signal intensity over the experimental time. (n=6). Figure 3.3 summaries these results.

Discussion

This chapter describes cerebral ischemia and stroke and the resultant cell swelling. It also reviews the brain slice preparation and it's utility for the study of cellular processes particularly during ischemia. The chapter then focuses on NMR imaging studies of ischemia and stroke. It reports on the development of an isolated perfused hippocampal slice preparation for NMR microimaging studies. The resolutions achieved depend primarily on the acquisition time. Acquisition times of 12-14 hours yielded spatial resolutions of 15-20 μm, which would be useful for morphological studies. However, since our goal was to perform functional studies on live perfused hippocampal slices, lower spatial and faster temporal resolutions were chosen. The baseline studies indicate that without perfusion, the signal intensity in diffusion weighted images increased over several hours. This is consistent with the notion that cellular edema occurs as the slice undergoes cytopathological changes due to nutrient deprivation. We established that a

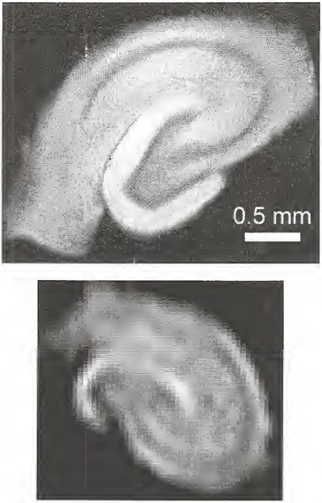

Figure 3.2 a. High resolution (15 μm in plane) image of a rat hippocampus; b. Image acquired in an experiment on live perfused brain slices

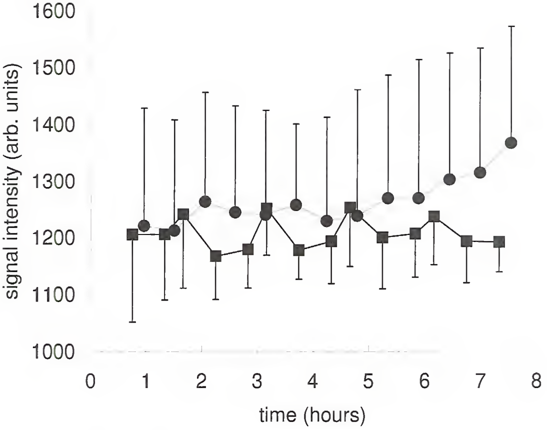

Figure 3.3 Diffusion weighted signal intensity (median, 90th percentile error bars) in perfused (•, n=6) and non perfused (•, n=7) slices. Perfusion maintains hippocampal slice viability.

short perfusion of 5 minutes every 1.5 hours was sufficient to maintain slice viability for 8 hours. The brain slice model has been used extensively and viability has been well characterized (Aitken et al., 1995) using various parameters including morphology, electrophysiology, metabolite levels, phosphorylation, and protein synthesis.

Neuronal edema is a manifestation of a wide range of neuropathologies (Joo, 1987; Schilling, Wahl, 1997) and the sensitivity of NMR to cellular water fluxes in brain slices make it ideal to study the pathogenesis of these diseases.

In summary, the experiments described in this chapter represent recent work, implementing NMR microimaging studies on the perfused brain slice model. The data demonstrate the potential of the brain slice model and may be applied to study the cellular basis for NMR contrast changes which may lead to development of realistic models of tissue compartmenation. These developments will allow a more quantitative approach to NMR and may result in an increased utility of clinical MR imaging.

CHAPTER 4
EFFECT OF TONICITY CHALLENGES ON WATER DIFFUSION AND CELL VOLUME IN PERFUSED HIPPOCAMPAL SLICES

To demonstrate the utility of the isolated perfused hippocampal slice preparation described in chapter 3, slices were challenged with a physiologically relevant osmotic perturbation. Brain slices were initially perfused in isotonic and then subjected to osmotic perturbations via perfusate exchange with 20% hypertonic and 20% hypotonic solutions. In diffusion weighted images, signal intensity changes of +16 (σ_{n-1} = 11)% (hypotonic) and -26 (σ_{n-1} = 10)% (hypertonic) were observed. No significant variation in response was observed across the slice when several subregions were examined. However, the signal to noise was a limiting factor so that there may be differences that were not discernable using the present parameters. This is the first report of NMR microimaging of the isolated brain slice. The technique will enable the correlation of NMR microimaging measurements with microscopic changes using other modalities and techniques in order to provide a better understanding of signals in clinical MR imaging.

Introduction

To date, nuclear magnetic resonance (NMR) imaging has been used primarily in a qualitative fashion, i.e. perceived changes in the signal intensity of NMR images are used to support a radiological diagnosis. Attempts to perform quantitative studies have been hampered in the main part by a large degree patient heterogeneity and inconsistent measurement techniques (Bottomley et al., 1987). In addition, the complex nature of biological systems make it difficult to perform controlled studies. Suitable tissue models are therefore required to investigate these confounding issues. Although many organs are amenable to isolation and perfusion, the brain is difficult to isolate and maintain, making it difficult to provide a realistic model of brain tissue.

To understand the signal changes observed in NMR imaging, the signal changes in the basic building blocks of tissues, i.e. single cells have to be studied. This has only recently become accessible through the development of NMR microscopy. NMR microscopy is now an established specialty of NMRI, and is being applied to a large variety of systems ranging from isolated tissues and single cells to materials applications. Recently NMR microimaging of single cells has identified large differences in the NMR characteristics of the cytoplasm and nucleus in isolated single cells (Schoeniger et al., 1994 and Hsu et al., 1996) and shown that these characteristics vary upon hypotonic perturbation (Hsu et al., 1996). However the latter studies were performed on isolated single neurons from a marine snail and lacked a realistic extracellular compartment. The isolated perfused brain slice preparation described herein serves as an intermediary between single cell and intact brain. To our knowledge, no NMR imaging has been reported on the brain slice model. In this chapter, experiments on brain slices are described in which physiologic perturbations of ±20% tonicity were used which is a range representative of *in vivo* perturbations such as those seen in a variety of neuropathological states.

Methods

A perfusion chamber was constructed from Delrin and consisted of a hollow cylindrical support arrangement (1mm thick walls) as shown in Figure 3.1. The chamber was constructed to fit within a standard 10 mm diameter NMR tube which in turn was placed within a commercial Doty microimaging probe (Doty Scientific Inc., Columbia, SC) interfaced to a Varian 600 MHz narrow bore instrument with their Unity console

(Varian Associates, Palo Alto, CA). The chamber parameters are as described in chapter 3.

Rat hippocampal slices (500 μm thick) were isolated using standard methods (Aitken et al., 1995). Briefly, male Sprague-Dawley rats (150-200g) were anaesthetized with Metofane, decapitated and the brain rapidly removed and placed into ice-cold artificial cerebrospinal fluid (aCSF). The aCSF comprised 120 mM NaCl, 3 mM KCl, 10 mM Glucose, 26 mM $NaHCO_3$, 2 mM $CaCl_2$, 1.5 mM KH_2PO_4, 1.4 mM $MgSO_4$ and was gassed with 95% O_2 and 5% CO_2 at pH 7.4. The hippocampus was then removed from the brain and sliced into 500 μm thick coronal sections using a McIlwain tissue chopper. A slice was then placed within the perfusion chamber. Care was taken to ensure that no bubbles were present in the chamber to prevent image distortion.

In preliminary experiments, slices were imaged to explore the spatial and temporal resolution issues and investigate the image contrast and structure. Subsequently a series of slices were imaged at modest spatial resolutions but relatively rapid image acquisitions times (a few minutes instead of hours) in order to investigate the effects of osmotic perturbations. One rat was sacrificed at the start of each day and multiple slices from the brain were then imaged. Imaging experiments were carried out at room temperature (18ºC). Slices were kept in aCSF on ice until required and previous studies showed that no significant sample degradation occurred during this time (up to 7 hours)(Palovcik, Phillips, 1986b), (Palovcik, Phillips, 1986a). Slices have been perfused for 30-40 hours whilst maintaining stable spontaneous action potentials indicating slice viability (Palovcik, Phillips, 1986a and Palovcik, Phillips, 1986b).

Slices were initially perfused with oxygenated isotonic aCSF at room temperature, which was then exchanged for a 20% hypotonic solution (made by adding distilled water to aCSF) followed by a 20% hypertonic solution (made by adding 60mM mannitol to

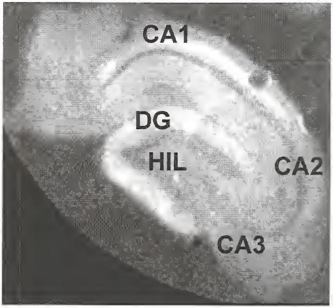

Figure 4.1. Microimage of a hippocampal slice, 40 x 40 x 300 μm resolution. Indicated are the anatomically defined subfields CA1-CA3, the hilus (HIL) and the dentate gyrus (DG). The small dark circle on the top right of the slice is due to a susceptibility artifact from a small air bubble.

aCSF). A standard diffusion weighted spin echo imaging sequence (TR=2 s, TE= 20 ms, b=700 s/mm^2 , 2 averages,) was utilized. The slices were perfused for 15 minutes between scans to allow for complete perfusion medium exchange and tissue stabilization. Perfusate flow was suspended during data acquisition to limit flow artifact (images acquired during perfusion at 2 ml/min exhibited severe artifacts). Images were collected at a resolution of 80 x 80 x 300 μm in approximately 8 minutes (128 x 128 matrix).

Results

Figure 4.1 shows a relatively high resolution image (40 x 40 x 300 μm) obtained in an hour. Fine structure is clearly evident in the image and it approaches histological quality. Similar images were obtained at 20 μm in-plane resolution but took several hours to acquire. Since the goal of this study is to investigate the effects of osmotic perturbations it was desirable to keep the scan times reasonably short and thus obtaining the highest spatial resolutions was not explored. In a preliminary study, the effects of gross hypo and hypertonic perturbations were demonstrated in three brain slices, producing signal changes of -50(8)% (mean(σ_{n-1})) during 83% hypertonicity (using 250 mM sucrose) and +63(24)% during 100% hypotonicity.

Figure 4.2a shows a representative image of a brain slice perfused in isotonic aCSF that was acquired in 8 minutes at 80 μm in-plane spatial resolution. A total of 10 separate slices were imaged over 2 days. Of these, 7 slices produced good results with similar contrast to that displayed in figure 4.2a. Data from the other 3 slices were unusable. Two slices contained significant susceptibility artifact caused by air bubbles introduced into the perfusion chamber (the technique of slice loading without trapping air improved with practice) and the remaining slice was incorrectly positioned in the chamber (trapped between the two outer halves of the chamber). In separate

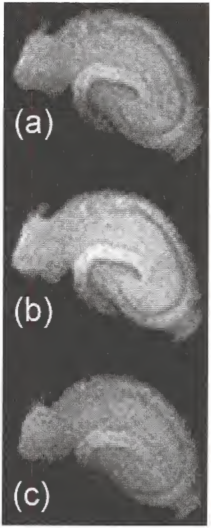

Figure 4.2. Diffusion weighted images of the same brain slice in (a) isotonic, (b) 20% hypotonic and (c) 20% hypertonic perfusate

experiments on the seven brain slices isotonic aCSF perfusate was exchanged for hypotonic and then hypertonic solutions. An example is shown in Figure 4.2. Similar image contrast changes were seen in 6 slices, i.e. signal increase with hypotonic perturbation and the converse in the hypertonic images. In one slice there was no visible change on hypotonic perturbation although there was a clear change after hypertonic perturbation.

The average signal changes measured in the whole slice are shown in Table 4.1. When referenced to the average isotonic signal intensity the data represent a mean signal increase of $16(\sigma_{n-1} = 11)\%$ for the hypotonic perturbation and a $26(\sigma_{n-1} = 10)\%$ decrease for the hypertonic. The observed changes were statistically significant ($p<0.0005$, repeated measures ANOVA).

An examination was made of the potential heterogeneity of response that may occur across the brain slice. Responses to tonicity changes were studied in isolated subregions in distinct anatomical areas of the CA1, CA2, CA3, dentate gyrus and hilus. All these subregions exhibited similar responses to the average of the whole slice and no significant difference as a function of anatomic location was observed ($p>0.6$).

Discussion

We have demonstrated that brain slices can be successfully microimaged and perturbed *in situ*, and that physiologically relevant perturbations (20% tonicity changes) cause significant signal changes in the images. These data are presented to demonstrate that this is a viable and potentially useful model for NMR imaging studies. The data presented are consistent with previous observations on humans and single cells. After an ischemic attack the diffusion coefficient of water in human and animal brains decreases, which is thought to be due to a change in the intra / extracellular compartmentation (Moseley et al., 1990a).

Table 1: Mean signal intensities (with standard deviation) for each of the seven brain slices in isotonic, 20% hypertonic and 20% hypotonic perfusion medium. The mean percentage increase or decrease is also given relative to the isotonic signal intensity

Slice number	Isotonic	Hypotonic	Hypertonic
r2	1005 (364)	1296 (410)	834 (287)
r3	1505 (333)	1485 (359)	1027 (252)
r5	1274 (395)	1597 (435)	847 (332)
r6	1146 (265)	1181 (354)	675 (215)
r7	1072 (309)	1286 (397)	813 (239)
r9	1509 (440)	1795 (482)	1154 (395)
r10	1574 (311)	1836 (373)	1350 (348)
mean change		+16(σ_{n-1} = 11)%	-26(σ_{n-1} = 10)%

These speculations are corroborated by measurements on single cells (Hsu et al., 1996). In the brain slice, the diffusion weighted signal intensity increased during hypotonic perturbation, which is also consistent with a decrease in the average diffusion coefficient potentially arising from compartmental changes. However since the data are qualitative, contributions from T1, T2 and changes in proton density could be important. To confirm these observations, we are presently quantitating the signal changes observed in the brain slice (i.e. measurements of T1, T2, apparent diffusion coefficient (ADC) and proton density) combined with measurements of cell volumes within the slices using other imaging modalities. It is unlikely that signal changes observed arise because of changes in total water content in perfused brain slices. Although a hypotonic perturbation may cause the slice to take up water resulting in an increase in the diffusion coefficient, we observed a decreased diffusion coefficient, indicating that changes in water compartmentation are the dominant mechanism of the observed signal changes.

There is an apparent asymmetry in the magnitude of the percentage signal change between the hyper and hypotonic perturbations (16 versus 26), but this is not statistically significant given the standard deviations in the measurements ($p=0.18$); improved measurement accuracy and preferably quantitative data are required to investigate this possibility. Additionally we noted that upon perfusion the slice sometimes moved a little due to flow effects which may also have contributed to measurement error. In future studies we plan to gently restrain the slice to eliminate this possibility. It is initially surprising that there was no detectable heterogeneity in the relative signal change across the brain slice upon perturbation given that it is known that different subfields of the hippocampus have varying sensitivity to ischemic attack. However this varying sensitivity may be related to a variability in the blood supply to the differing subfields of the hippocampus rather than to the sensitivity of the cells themselves in those regions. A heterogeneous response will not be as evident in the brain slice preparation where the tissue is evenly perfused. Again quantitative data are required to support this hypothesis.

Several issues now need to be addressed to fully characterize this model system. The health of the slice depends on preparation and perfusion (Aitken et al., 1995), and has been well studied. Different groups have successfully used brain slices and measured the viability of the slices by their own particular indicator, including morphology, electrophysiology, metabolite levels (determined by NMR spectroscopy), protein synthesis, and levels of phosphorylation or stress related proteins (Aitken et al., 1995). In future studies we will take the same philosophical approach, i.e. as long as the slices are stable with respect to their NMR characteristics then it will be assumed that they are 'healthy'.

The temperature of the slice is also an important concern. Preparations are easier to make at a lower temperature and tissue damage is reduced, but physiological temperatures are regarded as more desirable in many cases since they are expected to be more closely representative of the *in vivo* conditions. Coupled with this is the observation that damage occurring during slice isolation can be greatly reduced if the animal is cardiac perfused with ice cold perfusate before decapitation and slicing. Ultimately, it depends upon the information one is trying to acquire (Aitken et al., 1995), (Lipton et al., 1995). For the most part, the same characteristics are observed at room and physiological temperatures in brain slices, but changes tend to progress more slowly at the lower temperature. Consequently the majority of measurements are obtained at room temperature, especially for structural investigations. This is convenient for our NMR imaging studies since it will make maintenance of the preparations much easier. Although information related to metabolism may be better performed at physiological temperatures, studies of the relative changes in T1, T2 and ADC are unlikely to be significantly affected by a 10 to 20 degree variation in temperature.

Cell swelling occurs during the extraction procedure, as measured by increases in slice mass and light transmittance (Hosokawa et al., 1994). Since NMR imaging primarily maps water content and we are detecting NNMR changes as a response to cell swelling and shrinkage, it is crucial that the water content and distribution within the slices is well characterized and controlled. Andrew and MacVicar (Hosokawa et al., 1994) have demonstrated that the addition of a colloid such as dextran (4%) can eliminate water gain. Though the addition of dextran has an undesirable side effect of inducing severe neuronal pyknosis, this pyknosis can be eliminated by a reduction in the buffer osmolarity via adjustment of the NaCl concentration. This is particularly important at physiological temperatures. However at lower temperatures the water gain is greatly reduced and the addition of dextran may not be necessary. It has been suggested that the colloid be added only when water gain is evident (Hosokawa et al., 1994). We have the opportunity to directly examine this water gain issue with NMR imaging.

We hypothesize that the potential changes in the ratios of extracellular, cytoplasmic and nuclear volumes following cell injury and neoplastic transformation may contribute to signal intensity changes seen in clinical imaging. Moreover, an understanding of the NMR characteristics of isolated perfused brain slices will aid in the interpretation of the NMR characteristics of brain tissue in conventional neurological NMR imaging, and in particular how these characteristics vary in an mixture of conditions. NMR microscopy on brain slices offers an opportunity for examining these changes, especially since attempts to understand brain volume regulation are greatly hampered by the structural complexity of the central nervous system. For example, during normal synaptic activity neurotransmitters are released, changing the ionic composition of the extracellular space which has a direct effect on cell volume in neurons and glia. This regulation may become ineffective in a variety of conditions, and subsequent brain swelling occurs during hyperexcitability, status epilepticus, ischemia, anoxia, head trauma, hepatic encephalopathy and central pontine myelinolysis. Some of the most serious consequences of cell volume change are manifested by swelling or shrinkage of the brain, which can lead to severe neurological impairment and high mortality (Szafer et al., 1995b). Thus we believe that studies of this type will lead to an improved understanding of a variety of clinical conditions and the prevention or treatment of many neurological disorders associated with an osmotic disturbance.

Conclusions

This is the first report of NMR microimaging of individual brain slices. The prototype perfusion chamber has been designed to maintain the slices in a viable state for NMR studies. Further, the results demonstrate that images of the slices are significantly altered by physiologically relevant hypertonic and hypotonic perturbations. The studies open the way to quantitate the changes observed in terms of absolute T1, T2 and ADC, and to correlate the changes observed with measures of intra and extracellular volume changes assessed by other techniques. Together these data may be used to develop realistic models of tissues, such as that derived by Szafer et. al. (Szafer et al., 1995a). Investigations into the influence of experimental temperature and the possibility of water uptake by the slice are also required. Subsequently the model may be used to examine the effects of other types of perturbations (such as pH, temperature, and changes in membrane permeability) on the NMR signal characteristics. Hence, we expect the brain slice to become an extremely useful model for the examination of the mechanism of contrast changes in brain NMR images which ultimately will lead to an improved understanding of signal changes observed in clinical MR imaging.

CHAPTER 5
EFFECT OF OUABAIN ON WATER DIFFUSION IN THE HIPPOCAMPAL SLICE

High resolution NMR imaging of the isolated perfused rat hippocampal slice was used to quantitate ADC changes following ouabain induced cell swelling. Hippocampal slices were studied in artificial cerebrospinal fluid and then in ouabain using a 600 MHz narrow bore spectrometer and a home built perfusion chamber.

The brain slices demonstrated biexponential diffusion behavior. Following perfusion with 1 mM ouabain there was an increase in the fraction of slowly diffusing water. The ADCs of the two fractions did not change.

These data support the hypothesis that the decrease in the ADC of brain water following an ischemic attack is caused by cell swelling. The relative amplitudes of the two diffusing fractions do not match the expected ratio of intracellular and extracellular fractions. This discrepancy may be principally due to the difference in T2 relaxation rates of the two compartments.

Introduction

Diffusion weighted NMR imaging detects a significant decrease in the apparent diffusion coefficient (ADC) of water following the onset of cerebral ischemia (Moseley et al., 1990a and Benveniste et al., 1992). The physiological mechanisms underlying this change have yet to be fully determined. However, the evidence suggests that the redistribution of water between intracellular and extracellular compartments plays a significant role (Krizaj et al., 1996). During an ischemic insult oxygen deprivation inhibits the metabolic pump necessary to maintain normal ion gradients, leading to cellular swelling.

Several models have been proposed to explain the water redistribution and ADC changes observed. A widespread view is that cell swelling (cytotoxic edema) is responsible for these changes(Moseley et al., 1990a), (Benveniste et al., 1992). Rapidly diffusing water molecules in the extracellular space slow down as they move into the enlarged intracellular space thereby reducing the average ADC of the whole tissue. These conclusions are supported by both theoretical predictions (Szafer et al., 1995b) and work with an occlusive stroke model in cats (van Gelderen et al., 1994). Other groups have suggested that cellular swelling leads to an increase in the tortuosity of the extracellular space due to its reduced size. The subsequent decrease in the ADC of this compartment reduces the overall ADC of the tissue (Norris et al., 1994b). Helpern et al. (Helpern et al., 1992) have suggested that a reduction in cell membrane permeability, leading to restricted diffusion, is responsible for the observed alteration in ADC. However, theoretical predictions (Szafer et al., 1995b), evidence for restricted diffusion (Niendorf et al., 1994), and experiments on red blood cell suspensions (Latour et al., 1994) have indicated that permeability changes are unlikely to fully explain the large drop in ADC observed.

The mammalian brain slice is an established model for the measurement of water distribution and diffusion and has been used to investigate the cellular mechanism of ischemic tissue damage (Perez-Pinzon et al., 1995). We have recently demonstrated that rat hippocampal slices can be microimaged using NMR . Following osmotic perturbations there were significant changes in the signal intensity in the brain slices (chapter 4; Blackband et al., 1997). To further study these effects we hypothesized that the origin of biexponential diffusion observed in the brain (Niendorf et al., 1996) is due to tissue water compartmentation. To test this hypothesis the response of brain slices to ouabain was studied. Oxygen deprivation during ischemic stroke inhibits the Na+/K+ ATPase and disturbs normal transmembrane ion gradients causing cellular swelling.

Ouabain similarly inhibits the Na+/K+ pump prompting the use of ouabain as a model for ischemia (Benveniste et al., 1992).

Materials and Methods

Theory

Attenuation of the NMR signal in a typical diffusion weighted sequence is given by the monexponential as described in chapter 2:

$$S(b) = S_0 \exp(-bD) \qquad [5.1]$$

where S(b) is the measured signal intensity, S_0 is the signal intensity in the absence of diffusion weighting, b represents the integrated effect of all of the imaging and diffusion gradients upon the signal, and D is the ADC. In the case of a pair of matched diffusion gradients, b can be written (Stejskal, Tanner, 1965):

$$b = \gamma^2 G^2 \delta^2 (\Delta - \delta / 3) \qquad [5.2]$$

where γ is the gyromagnetic ratio, G is the amplitude and δ the duration of each gradient, and Δ is the time between the application of the two gradients. The period Δ - δ/3 is usually referred to as the diffusion time, τ. However, in experiments employing large imaging gradients (such as those used in this study), the imaging gradients and cross terms need to be included in the calculation of b (Neeman et al., 1990).

Equation 5.1 describes signal attenuation in samples with a single compartment. Brain tissue contains at least 2 compartments, typically intracellular and extracellular water (the intravascular contribution to the NMR signal is neglected in the following model). The signal attenuation measured in such tissue is dependent upon the rate of water exchange between these compartments (Stanisz et al., 1997a). In the limit of fast exchange (when all of the water molecules within a voxel have diffused through both compartments during τ), D can be written:

$$D = f_1 D_1 + f_2 D_2 \tag{5.3}$$

and:

$$f_1 = 1 - f_2 \tag{5.4}$$

where f_1 and f_2 are the volume fractions of the 2 compartments. Similarly, D_1 and D_2 are the ADCs of water in each compartment. In the limit of slow exchange (when the water molecules remain in one or other of the compartments during τ), signal attenuation becomes biexponential. That is:

$$S(b) = S_0\left[f_1 \exp\left(-bD_1\right) + f_2 \exp\left(-bD_2\right)\right] \tag{5.5}$$

and again:

$$f_1 = 1 - f_2 \tag{5.6}$$

As discussed in chapter 2, neither the fast nor slow exchange regime is encountered, but rather an intermediate condition. Kärger et al. (Karger et al., 1988) have described an analytical solution for this condition. Unfortunately, the solution may be overparameterized without knowledge of either water exchange rates or compartmental ADCs (Pilatus et al., 1997) and therefore the data reported below are summarized in terms of Eqn. 5.1 and 5.5. It is important to emphasize that although the

Kärger model contains a greater number of unknowns, the solution is, like Eqn. 5, a superposition of two exponentials.

Brain Slices

Rat hippocampii were isolated from male Sprague-Dawley rats (150 - 200 g) using standard methods (Palovcik, Phillips, 1986b) and cut into 500 μm thick coronal slices using a McIlwain tissue chopper. The brain slices were then placed in ice-cold artificial cerebrospinal fluid (aCSF) prior to imaging. The aCSF comprised 120 mM NaCl, 3 mM KCl, 10 mM Glucose, 26 mM $NaHCO_3$, 2 mM $CaCl_2$, 1.5 mM KH_2PO_4, 1.4 mM $MgSO_4$ and was gassed with 95% O_2 and 5% CO_2 at pH 7.4. During the imaging experiments both aCSF and 1 mM ouabain (added to aCSF) were perfused at room temperature (18-19°C).

NMR Imaging

The brain slice was placed in a perfusion chamber and lowered into a standard 10 mm NMR tube as previously described (chapter 3). All images were collected using a commercial Doty microimaging probe (Doty Scientific Inc.; Columbia, SC) interfaced to a Varian 600 MHz narrow bore instrument and Unity console (Varian Associates; Palo Alto, CA).

Images were acquired using a standard spin echo imaging sequence (repetition time, TR = 2 s, echo time, TE = 30 ms, 2 averages) with diffusion gradient lobes placed on either side of the 180° radiofrequency pulse. The diffusion weighting gradient was aligned with the slice selection gradient axis in all experiments and isotropic diffusion was assumed. In our previous studies imaging was carried out at microscopic resolutions (20 to 80 μm in plane resolution). By reducing this resolution the signal to noise ratio of the images was significantly improved and the imaging time reduced to enable quantitative diffusion measurements. We were not, however, able to assess individual sub-structures of the hippocampus. The images reported herein were collected at a resolution of 120 x 230 μm with a 300 μm imaging slice (128 x 64 matrix over a square 15 mm field of view). Each image was acquired in 4.3 minutes and ADCs were estimated from a series of 8 images acquired with a range of gradient amplitudes (δ = 3.5 ms, τ = 12.3 ms, g = 50 to 600 mT/m, and b=76, 187, 352, 570, 1169, 1983, 3012, 4256 s/mm^2). The influence of all imaging gradients (including cross terms) were included in the calculation of b.

Experimental Protocol

A slice was placed in the chamber and perfused (2 ml/min) with isotonic aCSF. Immediately prior to image acquisition flow was suspended and a series of 8 images, each with an increasing diffusion weighting, was collected in 35 minutes. Subsequently the slice was perfused for 15 minutes with 1 mM ouabain and the imaging sequence was repeated. Previous studies indicated that the signal from diffusion weighted images of the slice remained stable over 8 hours provided the perfusate was exchanged every 1.5 hours (chapter 3 and Bui et al., 1998b). To validate the accuracy of the technique measurements were also made in tubes containing isopropanol and dimethyl sulfoxide (DMSO).

To assess the influence of echo time on the calculated ADCs, 1 slice (bathed in aCSF) was imaged at echo times of 24.2, 30, and 100 ms. The diffusion time was fixed at 12.3 ms and all other imaging parameters remained as described above. Similarly, to assess the influence of diffusion time on the calculated ADCs another slice (bathed in 1 mM ouabain) was imaged at diffusion times, τ, of 6.5, 11.8, and 19.7 ms. To compensate for the shorter diffusion time employed in this experiment the b values used were limited to the range 50 to 2400 s/mm^2. The echo time was fixed at 30 ms for each experiment and all other imaging parameters remained as above.

Data Analysis

Two regions of interest were drawn on the diffusion weighted images. One encompassed the entire brain slice and the second was placed within the perfusate. The mean signal intensity within the region encompassing the slice in each image was fitted to Eqn. 5.5 using the Levenberg-Marquardt non-linear least squares fitting routine (Marquardt, 1963) and estimates of S_0, f_2, D_1, and D_2 were extracted. The mean signal intensity of the perfusate was fitted to Eqn. 5.1 to extract S_0 and D. In this case not all data points were used since the signal arising from the perfusate dropped to the level of the noise above a b value of approximately 1800 s/mm^2. Hence the estimate of D of the perfusate was typically calculated using only 5 of the 8 images. To compare the results obtained in the brain slice with those previously obtained *in vivo* (Benveniste et al., 1992) data from the ROI encompassing the brain slice in the first five images (b = 76 – 1169 s/mm^2) were fitted to Eqn. 5.1 and estimates of the best fit single ADC were also extracted.

Estimates of the various parameters and their standard deviations are presented in the table and text. Comparisons between the parameters estimated from brain slices in aCSF and 1 mM ouabain were made using a paired t-test.

Results

Nine brain slices from 5 rats were successfully examined in both aCSF and 1 mM ouabain. The diffusion coefficient measured in both aCSF and 1 mM ouabain was 1.95 (±0.02) x 10^{-3} mm^2/s. The diffusion coefficients measured in isopropanol and DMSO were 0.50 x 10^{-3} mm^2/s and 0.63 x 10^{-3} mm^2/s respectively (Fig. 5.1). Considering the temperature at which our experiments were conducted (18-19°C) (Le Bihan et al., 1989) the values measured in perfusate match well with previous results measured in free water and the values measured in isopropanol and DMSO are similar to previous studies (Niendorf et al., 1996 and Yongbi et al., 1996).

Data from the brain slices exhibited biexponential diffusion behavior in all cases. The data were fitted to Eqn. 5.5 and the results are shown in Table 5.1. In all cases the data fitted the model well ($r^2 = 0.99$). Single exponential ADCs estimated from the lower b values are also shown in Table 5.1. Figure 5.2 shows typical diffusion weighted images ($b = 1980$ s/mm^2) collected with the brain slice in aCSF (Fig. 5.2a) and then in 1 mM ouabain (Fig. 5.2b). Signal attenuation curves obtained from this example are shown in Fig. 5.3. Note the significant change in signal attenuation with increasing b when the brain slice is perfused in 1 mM ouabain, yet there is little change in the ADCs of the 2 components.

The effect of changing the echo time upon the estimated tissue water ADC is demonstrated in Fig. 5.4. The signal attenuation curves obtained at echo times of 24.2, 30, and 100 ms have all been normalized (based upon the respective estimates of S_0). Similarly, the effect of different diffusion times upon the estimated tissue water ADC is demonstrated in Fig. 5.5. For comparison the signal attenuation curves obtained at diffusion times of 6.5, 11.8, and 19.7 ms have been normalized.

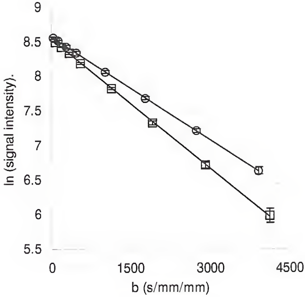

Figure 5.1: Signal attenuation (logarithm) measured in isopropanol (open circles) and DMSO (open squares). Error bars represent standard deviation from the mean. The lines passing through the data points are best fits to Eqn. 5.1.

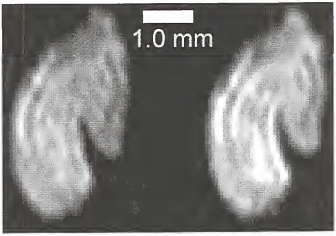

Figure 5.2: NMR diffusion weighted images ($b = 1980\ s/mm^2$) of a brain slice in (a) aCSF (left) and (b) 1 mM ouabain (right). Each image was acquired in 4.3 minutes as part of a series of 8.

Discussion

Our results indicate that rat hippocampal slices, perfused with both aCSF and 1 mM ouabain, demonstrate biexponential diffusion behavior across a range of diffusion times, τ. The estimated ADCs correspond to fast and slowly diffusing compartments. However, while these ADC measurements compare favorably with measurements of extracellular and intracellular water ADCs (van Zijl et al., 1991), (Schoeniger et al., 1994), (Assaf, Cohen, 1996) the corresponding fractional volumes do not match literature values (Perez-Pinzon et al., 1995). When subjected to 1 mM ouabain, the diffusion weighted signal in the slices is seen to increase and the single exponential ADC decrease (Table 5.1), consistent with previous results (Benveniste et al., 1992). However, no significant change is observed in the estimate of either ADC when biexponential diffusion is measured. Significant changes are observed in the sizes of both diffusing fractions. The rapidly diffusing fraction decreases by 10% of the total tissue volume and the slowly diffusing fraction increases by 10% (Table 5.1). While a number of groups have seen large changes in the ADC of water in the brain following ischemia (Moseley et al., 1990a), (Benveniste et al., 1992), (van der Toorn et al., 1996) or in models of ischemia (Verheul et al., 1994), few have identified and measured biexponential signal attenuation. Niendorf et al. (Niendorf et al., 1996) described biexponential diffusion attenuation in both healthy and ischemic rat brains. Our results, in rat hippocampal slices, resemble those of Niendorf et al. with a number of important distinctions, which are discussed below. An important similarity is that the estimates made of the fractional volumes of the fast and slow diffusing compartments do not match the fractional volumes of the extracellular and intracellular spaces. The fast diffusing compartment over estimates the extracellular compartmental size.

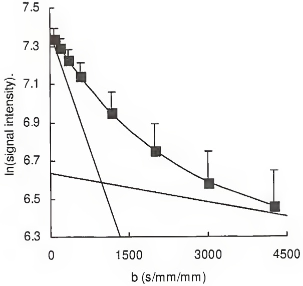

a

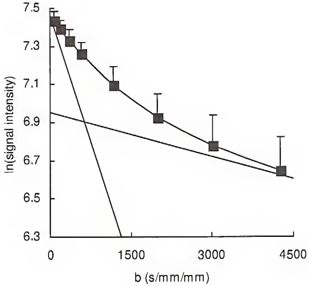

b

Figure 5.3: Signal attenuation (logarithm) measured in (a) aCSF and (b) 1 mM ouabain obtained from the brain slices shown in Fig. 5.2. Error bars represent standard deviation from the mean. The lines passing through the data points are best fits to Eqn. 5. The straight lines show the diffusion behavior of each compartment. Note the increase in the fraction of slowly diffusing water from 48% of the baseline signal (a) to 60% (b).

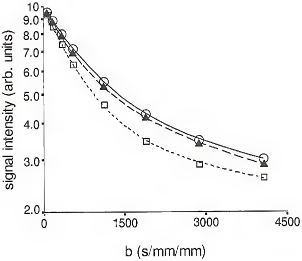

Figure 5.4: Signal attenuation (logarithmic scale) as a function of echo time. All curves have been normalized to their estimated signal intensity at b=0. Data collected at echo times, TE, of 24 ms (open circles), 30 ms (closed triangles), and 100 ms (open squares). In each case the lines represent best fits to the biexponential model (Eqn. 5.5).

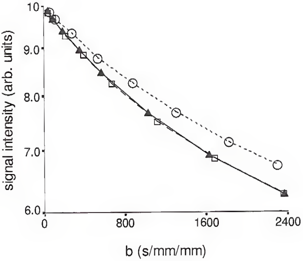

Figure 5.5: Signal attenuation (logarithmic scale) as a function of diffusion time. All curves have been normalized to their estimated signal intensity at b=0. Data collected at diffusion times, τ, of 19.7 ms (open circles), 11.8 ms (closed triangles), and 6.5 ms (open squares).

The discrepancy between the two diffusing fractions measured in these studies and previous measurements of the intracellular and extracellular fractions may be due to water exchange between the compartments. If so, we would expect to see a difference in the signal attenuation curves as a function of τ. We have investigated this possibility and the results are shown in Fig. 5.5. As τ decreases the curves approach the slow exchange limit. At $\tau = 11.8$ ms (close to the value employed in our regular experiments) the slow exchange limit may have been reached, since the attenuation curve overlaps that of $\tau = 6.5$ ms. However, at a diffusion time of 20 ms the exchange assumption is challenged as the curve is seen to decay less steeply rather than more steeply. This behavior is indicative of restricted diffusion, though the basis of this restriction is not clear. Further studies are required to address these issues using a wider range of diffusion times.

A difference in the T2 relaxation rate of the extracellular and intracellular spaces may contribute to our findings. To further complicate the picture, T2 is also affected by water exchange (Hazlewood et al., 1974), though the timescale of this effect (TE) is longer than the timescale over which the ADC is measured (τ). Figure 4 shows the effect of echo time upon the measured ADCs. If the T2 of the two diffusing components were equal, we would expect to see no difference in the diffusion curves as a function of TE. This is clearly not the case and contradicts the findings of Niendorf et al. (Niendorf et al., 1996) obtained at echo times of between 50 and 90 ms. The T2 of the intracellular space is likely to be much shorter than that of the extracellular (Schoeniger et al., 1994). If these experiments were obtained in the slow exchange regime (with respect to TE) then water in the extracellular space would diffuse away completely at higher values of b (van Zijl et al., 1991). The estimates of f_1 and f_2 would then be biased by the T2 of each compartment. If this was the case in our experiments, and assuming values for f_1 and f_2 of 0.8 and 0.2 respectively (Perez-Pinzon et al., 1995), the T2 of the intracellular space would need to be 20 ms or less to explain our results. A T2 of 29 ms has been reported for the cytoplasmic compartment of single *Aplysia* neurons using NMR microscopy (Schoeniger et al., 1994). Although not as low as 20 ms, it seems likely that a reduced T2 will be a significant contributor to the compartmental fraction discrepancy, mediated by the intermediate exchange regime that is probably in effect. In addition, Schoeniger et al. have reported T2 and ADC values for the nuclear compartment of *Aplysia* neurons that were closer to values obtained in extracellular water than those in the cytoplasm (Schoeniger et al., 1994). The nuclear compartment, though relatively small, may contribute to f_2 rather than f_1. More information about the NMR properties of the individual compartments of the brain slice is needed to further investigate these findings.

Differences in the compartmental T1 relaxation rates are unlikely to explain our results. The T1 of the extracellular space is presumably longer than that of the intracellular space (Schoeniger et al., 1994). As TR decreases we would expect the intracellular space to contribute to a greater fraction of the total signal. Our estimates of f_2 are already larger than the extracellular volume fraction and could not be explained by a T1 effect resulting from the TR employed. It is also possible that the surrounding perfusate may be contributing to the signal due to partial volume effects and artificially increasing the observed size of f_2. However, estimates of the possible partial volume effect suggest that perfusate outside the slice could only be contributing between 5 and 10% of the total signal. The perfusate contribution would need to increase to over 40% to account for our excessive estimate of f_2.

It is possible that the limited number of data points has biased our estimate of f_2. However, parameter estimates obtained over the same range of b-values but with more data points produced similar results (unpublished data) and the estimated time constants of the signal attenuation differ by an order of magnitude (Clayden, Hesler, 1992). Data points obtained at higher b values would improve the precision of our estimates and these considerations will drive future studies. Nevertheless, with 9 complete data sets, we were able to identify a significant change in f_2 following the application of ouabain ($p<0.0005$). Indeed, all 9 slices showed decreases in f_2. Furthermore there is no evidence for a consistent change in either D_1 or D_2 ($p>0.6$).

These results support the findings of Krizaj et al. obtained with tetramethylammonium ions in the turtle cerebellum during osmotic perturbation (Krizaj et al., 1996). The decrease in the single exponential ADC is due primarily to cell swelling and the concomitant movement of water from the extracellular to the intracellular space. Norris et al. (Norris et al., 1994b) have suggested that the increased tortuosity of the extracellular space following cell swelling decreases the ADC of this compartment thereby decreasing the overall tissue water diffusion. Krizaj et al. propose that changes in the extracellular tortuosity are generally small and only significantly influence diffusion at the extremes of cell swelling and contraction (Krizaj et al., 1996). They argue that changes in the size of the interstitial spaces have little effect since tortuosity is a measure of the topology or connectivity of the extracellular space. Our results support this hypothesis. We see no change in the fast ADC following the addition of 1 mM ouabain, but see a significant decrease in the fraction of the faster diffusing compartment. The changes in tortuosity may become significant upon more severe cellular perturbations. van der Toorn et al. used tetramethylammonium ions to measure large changes in extracellular tortuosity following the induction of global ischemia in rat brains (van der Toorn et al., 1996). This magnitude of change may represent an extreme referred to by Krizaj et al. (Krizaj et al., 1996) since the extracellular volume fraction in white matter decreased from 0.4 to 0.04 (van der Toorn et al., 1996). The magnitude of the changes observed in the current study are considerably smaller than this (Table 5.1).

In summary, we have demonstrated that water diffusion in the rat hippocampal slice is compartmentalized. Following disruption of the Na+/K+ ATPase using ouabain we observe an increase in the fraction of slowly diffusing water but no change in the ADC of either the fast or the slowly diffusing water fractions. These results suggest that cell swelling explains the early change in ADC following ischemia. Changes in the fast ADC were insignificant thus an increase in the tortuosity of the associated tissue space is not a factor. We speculate that the difference in apparent volume fraction obtained in this study compared with previously established measures of extracellular volume fraction is due primarily to differences in the T2 of the compartments. Taken together our data further demonstrate the potential of the brain slice model for understanding the origins of NMR signals. We anticipate that the brain slice model will contribute to the development of quantitative models that in turn will support the examination of a variety of neurological disease states.

Table 5.1 Estimates of the diffusion parameters of equation 5 (n=9)

	value in aCSF mean (SD)	value in 1 mM ouabain mean (SD)	p value*
S_0 (arb. units)	1600 (71)	1697 (71)	<0.0005
f_2 (no units)	0.533 (0.064)	0.438 (0.050)	<0.0005
D_2 ($\times 10^{-3}$ mm^2/s)	1.015 (0.155)	1.027 (0.178)	0.68
D_1 ($\times 10^{-3}$ mm^2/s)	0.089 (0.026)	0.086 (0.011)	0.62

*comparing parameter values obtained in aCSF and 1 mM ouabain using a paired t-test

CHAPTER 6
THE EFFECT OF NMDA INDUCED EXCITOTOXICITY ON WATER DIFFUSION IN THE PERFUSED HIPPOCAMPAL SLICE

Significant changes in the apparent diffusion coefficient (ADC) of water are observed in nuclear magnetic resonance (NMR or MR) images of patients with acute ischemic stroke. However, the underlying mechanisms of these ADC changes are still unresolved. To analyze possible mechanisms, this study applies NMR imaging on a 14.1 Tesla narrow-bore magnet to quantitatively study water diffusion in individually perfused brain slices following exposure to NMDA excitotoxicity. The results indicate that brain slices have at least two distinct diffusing water compartments with ADCs of $0.96 \pm 0.10 \times 10^{-3}$ mm^2/s and $0.06 \pm 0.01 \times 10^{-3}$ mm^2/s. When excitotoxicity was induced with NMDA, there was a significant decrease in the fraction of the fast diffusing water component in the slices ($p<0.001$). However, neither ADC changed significantly. Prior treatment with MK-801 depressed the effects of NMDA ($p<0.01$, ANOVA).

The results demonstrate brain slice compartmental changes resulting from direct receptor stimulation and provide evidence for tissue water redistribution as an important mechanism for ADC changes seen in clinical MRI. The brain slice preparation affords a well-controlled method to study the mechanisms of tissue NMR contrast, bridging the gap between basic NMR studies and clinical MRI. The brain slice model also offers a new way to test the utility of potential anti-stroke drugs using high field NMR imaging.

Introduction

Shortly after an ischemic insult to the brain, the apparent diffusion coefficient of water decreases, but the underlying mechanisms are not clear (Moseley et al., 1995). At least 4 mechanisms have been postulated to explain this finding. One states that water redistribution during ischemia plays an important role. In this model the ADC decrease following ischemia is attributed to cytotoxic edema resulting from water shifting from the faster diffusing extracellular matrix into the slower diffusing intracellular compartment and thus, the average ADC decreases (Benveniste et al., 1992). The model of water redistribution would therefore predict that the individual intra and extracellular ADCs do not change during an ischemic insult but that the fractional volumes would change. A second explanation states that cytotoxic edema results in a decrease in the extracellular compartmental volume, restricting diffusion such that extracellular water ADC decreases (Norris et al., 1994a). A third mechanism proposed is that ischemia decreases cell membrane permeability to water, leading a decrease in ADC. Currently, the evidence indicates that membrane permeability changes are unlikely to explain the observed changes in ADC (Latour et al., 1994; Szafer et al., 1995b). A fourth mechanism is that ischemia leads to a reduction in intracellular water ADC because of a decrease in active cell streaming or an increase in cellular viscosity (Neil et al., 1996). To analyze these different possibilities, we have developed a perfused tissue preparation to study water ADC with NMR imaging.

Previous studies on isolated perfused single neurons undergoing osmotic challenges suggest that water redistribution contributes significantly to the clinically observed ADC changes (Hsu et al., 1996). To provide a more realistic extracellular compartment, we implemented NMR imaging studies on perfused brain slices. Brain slices can be maintained and imaged at high resolution (figure 6.1). Data on slices perturbed with 20% tonicity changes suggest that NMR microscopy is sensitive to water redistribution following a physiologically relevant osmotic stress (Blackband et al., 1997). Quantitative studies of water diffusion coefficients in the brain slices revealed biexponential diffusion behavior allowing the identification of fast and slow diffusing compartments (Buckley et al., 1998). In addition, blockade of the Na^+/K^+ ATPase by 1 mM ouabain resulted in changes in the relative sizes of the slow and fast diffusing compartments but not in the respective ADCs of the two compartments. Since crippling of the Na^+/K^+ ATPase is one of the cellular events that occur during ischemia induced cytotoxic edema, this information supports the hypothesis of tissue water redistribution during stroke.

Although stroke related neuronal death results from a complicated pathophysiologic cascade, death due to free radical injury and excitotoxicity from increased extracellular excitatory amino acids are well recognized (Choi and Rothman, 1990). The glutamate NMDA receptor is thought to mediate many of the damaging effects of ischemia. Multiple lines of evidence indicate that blocking this receptor and other components of the glutamate cascade result in amelioration of ischemia induced neuronal injury (Marini et al., 1997; Silver et al., 1996; Small, Buchan, 1997). Clinically, one of the earliest detectable consequences of ischemic stroke is a change in water diffusion.

In this study, we applied quantitative NMR imaging to measure water diffusion in isolated perfused hippocampal slices in an excitotoxic model of cerebral ischemia to further validate the brain slice as a model to study the mechanisms underlying *in vivo* NMR experiments. The brain slice model allowed measurement of two distinct diffusing compartments with very different ADCs. We used it here to address the question of whether these ADCs change during chemical ischemia (induced by high dose NMDA treatment). This is the first application of the perfused brain slice model to study direct neurochemical stimulation. The study further tested the ability of NMR imaging to detect blockade of NMDA action by its antagonist MK-801 in the isolated perfused brain slice preparation.

Experimental Procedures

Animal experiments were carried out in accordance with National Institutes of Heath guidelines and approved by the University of Florida Institutional Animal Care and Use Committee. Efforts were made to minimize the number of animals used.

Rat hippocampii were isolated from male Harlan Sprague-Dawley rats (180-200g) and cut into 500 μm thick coronal slices. The slices were bathed in ice cold artificial cerebrospinal fluid [aCSF] prior to experiments. The aCSF comprised 120 mM NaCl, 3 mM KCl, 10 mM Glucose, 26 mM $NaHCO_3$, 2 mM $CaCl_2$, 1.5 mM KH_2PO_4, 1.4 mM $MgSO_4$ and was gassed with 95% O_2 and 5% CO_2 at pH 7.4. During the NMR experiments the perfusate (aCSF) was maintained at room temperature, 19°C.

The brain slice was placed in a perfusion chamber and lowered into a standard 10 mm NMR tube (Blackband et al., 1997). Data were collected using a Doty microimaging probe interfaced to a Varian 14.1 Tesla narrow-bore instrument. Images were acquired using a diffusion-weighted spin echo sequence (TR=2 s, TE=30 ms) with diffusion gradient lobes placed on either side of the 180° radiofrequency pulse. Diffusion weighting was aligned with the slice select gradient in all experiments. Microimages can be collected (Fig. 1) but for quantitative analysis, images were collected at a resolution of 120 x 230 μm with a 300 μm imaging slice. ADCs were estimated from a series of 8 images acquired in a total of 35 minutes with a range of gradient amplitudes ($\Delta - \delta/3$ = 12.3 ms, b=35-7935 s/mm^2). To avoid flow related image artifacts, perfusion was stopped during image acquisition. An initial series was collected with the slice in aCSF. The perfusate was then exchanged for either aCSF (n=10) or 50 μM MK-801 in aCSF (n=10) and the samples re-imaged. Finally the slices were then perfused in NMDA (12 in 500 μM NMDA and 8 in 1mM NMDA) and a further image series collected.

In a standard diffusion weighted NMR sequence the apparent diffusion coefficient can be calculated from:

$$S(b) = S_0 \exp(-bD) \tag{6.1}$$

where S(b) is the measured signal intensity, S_0 is the signal intensity in the absence of diffusion weighting, b represents the integrated effect of all of the imaging and diffusion gradients upon the signal, and D is the ADC. Equation 1 describes signal attenuation in samples with a single compartment. However, brain tissue contains at least 2 compartments, typically intracellular and extracellular water. The signal attenuation measured in such tissue is dependent upon the rate of water exchange between these compartments and the diffusion time employed. With the gradients, temperature and short diffusion time used in these experiments, we approach the slow exchange limit (Buckley et al., 1998; Li et al., 1998). Additionally, at a short diffusion time, the diffusion curve shape does not depend strongly on exchange rate (Li et al., 1998). Taken together, a slow exchange biexponential model is appropriate to analyze brain tissue. In the limit of slow exchange (when the water molecules remain in one or other of the compartments during the diffusion time), signal attenuation becomes:

$$S(b) = S_0 \left[f_1 \exp(-bD_1) + f_2 \exp(-bD_2) \right] \tag{6.2}$$

where f_1 and f_2 are the relative fractions of the fast and slow diffusing water respectively and $f_1=1-f_2$. D_1 and D_2 correspond to the ADCs of the fast and slow diffusing fractions respectively.

The data collected in these studies were analyzed using the above equations. Equation 6.1 was used to evaluate a region of interest in the perfusate, while equation 6.2 was employed for a region of interest encompassing the entire brain slice. Estimates of S_0 and D of the perfusate, were obtained by fitting eqn. 6.1 to the mean signal intensity at each b-value. Eqn. 6.2 was fitted to the mean signal intensity at each b-value within the brain slice region using the Levenberg-Marquardt non-linear least squares fitting routine and estimates of S_0, f_2, D_1, and D_2 were extracted. Comparisons between parameter estimates before and after NMDA treatment and the influence of NMDA dose and MK-801 treatment were made using repeated measures analysis of variance (ANOVA) and expressed as mean ± standard deviation.

Results

Twenty hippocampal brain slices were successfully examined. A high resolution NMR microimage of a typical hippocampal slice (20 μm in plane resolution) is shown in figure 6.1a. Figure 6.1b is representative of the 120 μm x 230 μm images acquired in 4.3 minutes utilized for quantitative diffusion measurement on perfused slices. Signal attenuation curves for a typical slice in aCSF and NMDA are shown in figure 6.2. Figure 2(a) represents signal attenuation in a brain slice not treated with MK-801 while figure

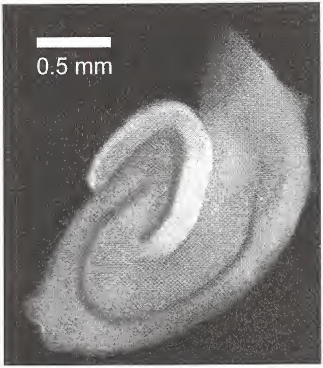

(a)

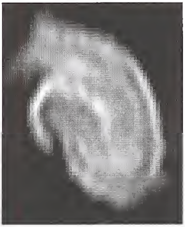

(b)

Figure 6.1 NMR images of rat hippocampal brain slices. (a) NMR microimage at 20 μm in plane resolution acquired in 14 hours. (b) NMR image at 120 μm x 230 μm resolution acquired in 4.3 minutes for experiments on live perfused brain slices.

2(b) represents signal attenuation in a slice treated with 50 μM MK-801. Data from all slices exhibited non-monoexponetial diffusion behavior, which fitted well to a biexponential model. (r^2=0.99). Two diffusing fractions were distinguished. The fast diffusing fraction had a diffusion coefficient of $0.957 \pm 0.099 \times 10^{-3}$ mm^2/s, and made up 55±5% of the total NMR signal while the slow diffusing fraction had a diffusion coefficient of $0.060 \pm 0.006 \times 10^{-3}$ mm^2/s. When stimulated with NMDA there was a significant decrease in the fraction of rapidly diffusing water by 5% ($p<0.001$). The diffusion coefficients of the slow and fast diffusing components did not change significantly after treatment with either dose of NMDA. There were no significant differences in the effects of 500 μM and 1mM NMDA on water fractions ($p=0.42$). Prior treatment with 50 μM MK-801 significantly depressed the effect of NMDA ($p<0.02$).

Discussion

This study examines changes in water diffusion following NMDA induced excitotoxicity in perfused hippocampal slices. There were two detectable diffusing water fractions in the slices. Following treatment with NMDA, the slices showed increases in the fraction of slowly diffusing water but the ADCs of the fast and slow diffusing volume fractions did not change. Further, we showed that prior treatment with MK-801 blocked NMDA induced changes in the NMR signal. These results indicate that NMR imaging is sensitive to neurochemically induced compartmental changes in perfused hippocampal slices and provide new data illustrating the utility of the of the brain slice as model for *in vivo* NMR changes in clinical pathology.

Previously, we applied NMR microscopy to our perfused brain slice preparation to study cellular changes following osmotic perturbations (Blackband et al., 1997).

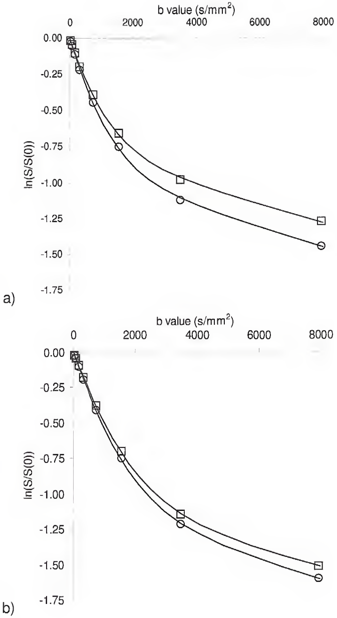

Figure 6.2 Normalized signal attenuation (logarithm) measured in (a) an untreated brain slice and (b) a brain slice treated with MK-801. In each graph, the circles represent data obtained with the brain slice in aCSF. Upon treatment with NMDA (data represented by squares) the fraction of fast diffusing water decreased by 6% (a) and 1% (b). The lines passing through the data points are best fits to Eqn. 6.2.

Subsequently, we quantitiated water diffusion in the slices and showed that it was compartmentalized (Buckley et al., 1998) which is similar to the findings of others using NMR spectroscopy(Norris et al., 1994a). Numerous groups have reported decreases in the average ADC following ischemic stroke (Moseley et al., 1990a) and NMDA exposure (Benveniste et al., 1992). In fact, Niendorf et al.(1996) studied NMDA excitotoxicity and MK-801 treatment using NMR spectroscopy *in vivo* and a biexponential analysis but did not report changes in individual ADCs. In our study, no changes were observed in the individual ADCs when fitted to a biexponential model. The techniques used herein afford an opportunity to distinguish two distinct diffusing fractions, which may correspond to physiological water compartments. That the ADCs did not change in our study is consistent with the widely held model of tissue water redistribution. It is likely that cytoskeletal structures present a diffusion barrier resulting is a lower intracellular water ADC. With NMDA treatment cytotoxic edema ensues, resulting in a net shift of water into the intracellular compartment such that it now contributes more to the average ADC. Our results of no change in the individual ADCs and an increase in the volume fraction of the slowly diffusing compartment support this view. Clinically, a decrease in the ADC is reported shortly after an ischemic insult while T2 changes are seen hours later. We believe that cytotoxic edema stemming from ischemia induced release of glutamate and stimulation of the NMDA receptor results in the initial decrease in the average ADC. It should be noted, however, that while an increase in the fraction of the slow diffusing compartment in our study after NMDA treatment suggest that this may represent the water in the intracellular compartment, the fractions do not match literature values of intra and extracellular volumes (Perez-Pinzon et al., 1995). The possible explanations for this difference may be accounted for by considering several issues, including differences in slice preparation and methods of measurement. For example, Newman et al. (1995) measured an extracellular compartment of 33% in the hippocampal slice using a radiotracer (^{14}C-PEG) technique, while Perez-Pinzon et al.(Perez-Pinzon et al., 1995) measured a 20% extracellular compartment using iontophoresis. The radiotracer technique measures the average ECS over the entire slice, including the cut edges. Iontophoresis measures small regions inside the slice at the tip of the microelectrodes. The method used in the present study resulted in a fast diffusing compartment larger than either technique. There are several possibilities for this. This estimate did not consider the difference in spin density of the intra and extracellular compartments which has been estimated in erythrocytes at 0.71 and 0.95 respectively (Pirkle et al., 1979); this would lead to an overestimate of extracellular space. Furthermore, ADC and T2 measurements in single *Aplysia* neurons (Schoeniger et al., 1994), suggest that the nuclear compartment has characteristics more akin to the extracellular than intracellular compartment which would result in overestimation of the extracellular compartment. The rest of the difference may be due to T2 relaxation effects. The evidence suggests that the T2 of the intracellular space is much shorter than that of the extracellular space (Hsu et al., 1996; Schoeniger et al., 1994). Buckley et al. reported that the diffusion curves in hippocampal slices varied as a function of echo time. The longer T2 of the extracellular compartment could account for an overestimation of extracellular volume. A more in depth discussion of these issues may be found in a previous paper by Buckley et al.(Buckley et al., 1998) Nevertheless, since we found no changes in the ADCs of either the fast or slow diffusing water compartments in our perfused slices, it is unlikely that the model of a decreased extracellular ADC is involved in our brain slice model. Recent NMR spectroscopic studies of compartment specific tracer molecules suggest that their extracellular and intracellular ADCs are similar and both decrease with ischemia (Duong et al., 1998; Neil et al., 1996). Our study indicates that water ADCs do not change in the same manner. Since most of the tracer molecules used have a molecular weight many times that of water and they usually have a large hydration sphere, it is likely that their diffusion behavior is different than that of water. Taken together, our findings support the hypothesis that water redistribution plays a critical role in ischemia related changes in ADC.

The perfused brain slice model is widely used in physiological studies because it allows detailed measurements that are difficult to carry out *in vivo*. One of the inherent problems with *in vivo* models of ischemic stroke is the myriad of pathophysiolgic sequelae that complicate the analysis of the mechanisms underlying ischemia related neuronal death. The brain slice preparation offers a more controlled model to study these processes and therefore, has been used extensively to study numerous biological processes with multiple techniques (Collingridge, 1995). These cell and molecular biology techniques provide unrivaled details about the cellular basis of disease. The advantage of NMR over most other techniques is the possibility of extending measurements directly to the *in vivo* clinical setting. The results of this study are consistent with previous *in vivo* and *in vitro* studies and serve as further validation of the brain slice model for evaluating the origins of contrast in clinical MR imaging.

CHAPTER 7

GADODIAMIDE ENCHANCED NMR IMAGING MEASUREMENT OF INTRACELLULAR VOLUME IN THE PERFUSED HIPPOCAMPAL SLICE

T1-weighted NMR imaging of the isolated perfused rat hippocampal slice was used to estimate cell volume fraction. Brain slices were studied in artificial cerebrospinal fluid (aCSF) doped with 0, 1 and 4 mM gadodiamide using a 600 MHz narrow bore spectrometer and a home built perfusion chamber. The relaxivity of gadodiamide in aCSF was measured and used to estimate cell volume in fraction in four brain slices (0.67 ± 0.04). The effect of 60 mM mannitol on a further brain slice was also demonstrated. The technique provides a simple means of estimating cell volume fraction and can be extended to produce maps of cell density.

Introduction

The mammalian brain slice is an established model for the measurement of water distribution and diffusion (Nicholson and Sykova, 1998) and has been used to investigate the cellular mechanism of ischemic tissue damage (Pérez-Pinzón et al., 1995). NMR studies of brain slice metabolism have been reported (Bachelard et al., 1994; Pirttila, Kauppinen, 1994; Ting, Degani, 1993) and microimages of rat hippocampal slices have been obtained using NMR (Blackband et al., 1997). Recently, we demonstrated that two diffusing water fractions could be observed in the slices and the sizes of these fractions change significantly in response to the administration of ouabain (Buckley et al., 1999).

Cell volume fraction is an important determinant of the NMR characteristics of a tissue and is altered in a number of pathologic states. In particular, cell swelling is known to occur during the early stages of ischemia (Pérez-Pinzón et al., 1995) and leads to a significant change in the average diffusion coefficient of water (Moseley et al., 1990b). The perfused hippocampal slice provides a useful model for NMR studies of the brain but has not been well characterized. In the following note we describe a method of determining the cell volume fraction of perfused hippocampal slices using the paramagnetic contrast agent, gadodiamide (Gd-DTPA-BMA).

Materials and Methods

Theory

The NMR signal obtained from an inversion recovery spin echo sequence is given by:

$$S = S_0\left(1 - \exp\left(-\frac{TR}{T_1}\right) + 2.\exp\left(-\frac{TR - TE/2}{T_1}\right) - 2.A.\exp\left(-\frac{TI}{T_1}\right)\right) \qquad [7.1]$$

where S is the measured signal intensity, S_0 is the T2-weighted signal intensity obtained from a fully relaxed sample, A is a factor (≤ 1) characterizing the inversion efficiency of the 180° pulse and TR, TE, and TI are the repetition, echo, and inversion times respectively.

Equation 7.1 describes the signal intensity in samples relaxing with a single T1. Brain tissue contains at least two compartments, typically the intracellular space (ICS) and the extracellular space (ECS). The intravascular contribution to the NMR signal is neglected in the following model. The T1 measured in such tissue is dependent upon the size and intrinsic T1 of each compartment and the rate of water exchange between compartments

(Donahue et al., 1994). In the limit of fast exchange (when the rate of water exchange between compartments is greater than the difference in intrinsic relaxation rates of the compartments), T1 can be written:

$$\frac{1}{T_1} = \frac{f_{ICS}}{T_{1(ICS)}} + \frac{f_{ECS}}{T_{1(ECS)}}$$

and $$f_{ECS} = 1 - f_{ICS} \qquad [7.2]$$

where f_{ICS} and f_{ECS} are the spin population fractions originating from the ICS and ECS respectively and T1(ICS) and T1(ECS) are the intrinsic relaxation times of ICS and ECS respectively. If the system is not in the fast exchange regime, the T1 recovery becomes biexponential in nature.

Gadodiamide is a paramagnetic contrast agent that is distributed in the ECS of most tissues and does not normally enter the cell (Normann, Hals, 1995). Gadodiamide increases the relaxation rate of nearby protons thereby reducing the T1 in the ECS, thus in the fast exchange regime:

$$\frac{1}{T_1} = \frac{f_{ICS}}{T_{1(ICS)}} + (1 - f_{ICS})\left(\frac{1}{T_{1(ECS)}} + r_1.[Gd]\right) \qquad [7.3]$$

where [Gd] is the concentration (mM) and r_1 is relaxivity ($mM^{-1}s^{-1}$) of gadodiamide. This may rearranged to give:

$$\frac{1}{T_1} = \frac{1}{T_{1(0)}} + (1 - f_{ICS})r_1.[Gd] \qquad [7.4]$$

where T1(0) is the tissue T1 in the absence of gadodiamide.

NMR Acquisition

All NMR data were collected using a commercial Doty microimaging probe (Doty Scientific Inc.; Columbia, SC) interfaced to a Varian 600 MHz narrow bore instrument and Unity console (Varian Associates; Palo Alto, CA). An inversion recovery spin echo sequence, employing a hyperbolic secant adiabatic inversion pulse, was used to obtain the data. All images were acquired using a 300 μm slice thickness and 230 x 230 μm in plane resolution (64 x 64 matrix over a 15 mm field of view, TR = 5 s, TE = 8 ms).

Relaxivity of Gadodiamide

To assess its relaxivity, various quantities of gadodiamide (Nycomed Inc.; Princeton, NJ) were added to artificial cerebrospinal fluid (aCSF, composition outlined below) to produce solutions of 0, 0.125, 0.25, 0.5, 1.25, 2.5, and 4 mM gadodiamide. The solutions (each 2.5 ml) were placed in 5 mm NMR tubes and their temperature allowed to equilibrate to room temperature (19°C). The T1 of each solution was measured from a series of profiles; TR = 35 s, TE = 9 ms, 2 averages, and 9 inversion times logarithmically spaced between 0.01 and 33 s. The T1 was estimated by a non-linear least squares fit of Eq. [1] to the data. The relaxivity was subsequently obtained by linear regression to a plot of 1/T1 Vs gadodiamide concentration.

Brain Slices

Rat hippocampii were isolated from male Sprague-Dawley rats (150 - 200 g) using standard methods (Palovcik, Phillips, 1986b) and cut into 500 μm thick coronal slices using a McIlwain tissue chopper (Blackband et al., 1997). The brain slices were then placed in ice-cold aCSF prior to imaging. The aCSF comprised 120 mM NaCl, 3 mM KCl, 10 mM Glucose, 26 mM $NaHCO_3$, 2 mM $CaCl_2$, 1.5 mM KH_2PO_4, 1.4 mM $MgSO_4$ and was gassed with 95% O_2 and 5% CO_2 at pH 7.4. During all experiments, the aCSF was perfused at room temperature (19°C). The brain slice was placed in a perfusion chamber and lowered into a standard 10 mm NMR tube as previously described (Blackband et al., 1997). The slice was perfused (2 ml/min) with isotonic aCSF. Immediately prior to image acquisition flow was suspended and a series of 11 images, each with an increasing inversion recovery period (TI = 0.015, 0.027, 0.048, 0.085, 0.152, 0.272, 0.485, 0.866, 1.546, 2.760, 4.926 s), was collected in 60 minutes. The slice was then perfused for 15 minutes with a 1 mM gadodiamide solution and the imaging sequence was repeated. Finally, the slice was perfused for 15 minutes with a 4 mM gadodiamide solution and the imaging sequence was again repeated. Previous studies have demonstrated the stability of the slice preparation during such a protocol (Bui et al., 1998b).

To assess the influence of a change in cell volume on the T1 measurements a further slice was imaged in aCSF and then in 0.125 mM gadodiamide. 60 mM mannitol was added to the gadodiamide doped aCSF, the slice was perfused, and a further image series was acquired. For these acquisitions a shorter protocol of 5 TI values was employed (TI = 0.033, 0.122, 0.407, 1.35 and 4.95 s).

Data Analysis

A region of interest was traced on the images to encompass the entire brain slice. The mean signal intensity within the region encompassing the slice in each image and at each gadodiamide concentration was recorded and all the data were combined. This data was then used to simultaneously fit the combination of Eqns. 7.1 and 7.4 using the downhill simplex technique to minimize the sum of squared differences between the model predictions and the data. From this analysis estimates of $S_0(0)$, $S_0(1)$, $S_0(4)$ (fully relaxed signal at each gadodiamide concentration), f_{ICS}, T1(0), and A can be extracted. Values of the various parameter estimates and their standard errors are presented in the text unless otherwise indicated.

Results

The relaxivity of gadodiamide measured in aCSF was 3.75 ± 0.02 $mM^{-1}s^{-1}$. This result, obtained from 14 individual measurements, is summarized in figure 1. As expected, the T1 recovery curves measured in the aCSF were all monoexponential in nature. These results compare favorably with previous room temperature measurements made in plasma, saline and cartilage at 360 MHz (Donahue et al., 1994).

Five hippocampal slices were studied in total. Four brain slices were examined in aCSF, 1 mM gadodiamide, and 4 mM gadodiamide. In each case, the data were well fitted by Eqs. [7.1] and [7.4]. The results are summarized in table 7.1. An example data set is shown in figure 7.2. The data and model predictions are well matched and there is no evidence of biexponential (intermediate to slow exchange) behavior in the data. In the fifth slice, where 60 mM mannitol was added to the gadodiamide doped perfusate, a change in the T1 recovery curve was observed. The T1 of the slice was estimated at 1.90 ± 0.09 s in aCSF, 1.33 ± 0.05 s in 0.125 mM gadodiamide, and 1.23 ± 0.04 s in 60 mM mannitol. Assuming a gadodiamide relaxivity of 3.75 $mM^{-1}s^{-1}$, this corresponds to a cell fraction of 0.53. The addition of 60 mM mannitol produced an increase in the distribution volume of gadodiamide and a decrease in the cell fraction to 0.41.

Figure 3 (a) shows an image in which the signal intensity is proportional to the fractional ECS volume of the voxel. This ECS map was calculated as the difference in 1/T1 at each voxel with the slice in aCSF and 1 mM gadodiamide ($=f_{ECS}.r_1.[Gd]$, Eqn. 7.4). The ICS fraction, computed as $1-f_{ECS}$, is displayed in figure 3 (b).

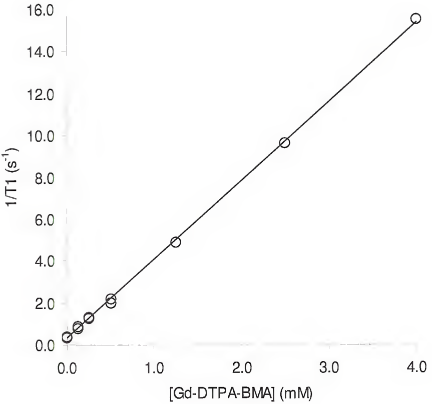

Figure 7.1: Relaxivity of gadodiamide in aCSF. Data were obtained from 14 experiments using 7 separate concentrations of gadodiamide. By linear regression the relaxivity was estimated at 3.75 ± 0.02 mM^{-1}s^{-1}.

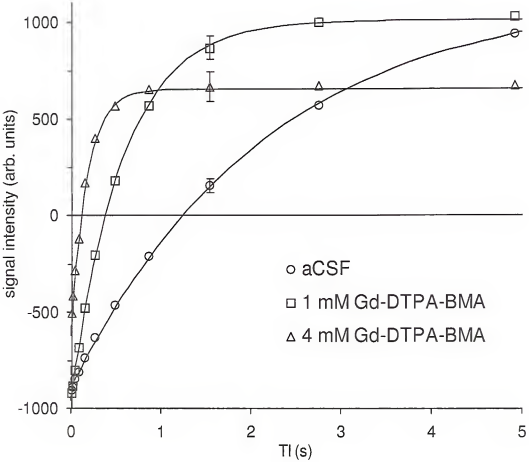

Figure 7.2: Inversion recovery data obtained from a hippocampal slice perfused with aCSF (circles), 1 mM gadodiamide (squares) and 4 mM gadodiamde (triangles). Error bars representing the SD of the mean within the brain slice are shown at one inversion time (remaining error bars were removed for clarity). The lines passing through the data points represent the best fit of Eqs. [7.1] and [7.4] to the data.

Discussion

The technique employed to measure cell volume fraction is broadly similar to previously published methods (Braunschweiger et al., 1986; Donahue et al., 1995; Larcombe-McDouall et al., 1994). That is, a paramagnetic substance with an ECS distribution volume is added to the tissue and the change in relaxation rate is measured. This approach requires a number of assumptions. Firstly, the gadodiamide does not enter the cells. There is little evidence of this occurring in healthy cells, even at 10 mM concentrations of Gd-DTPA (Larcombe-McDouall et al., 1994). However, we cannot discount this possibility in damaged cells, probably arising close to the cut edge of the slice and in cells that may be compromised following slice extraction (Newman et al., 1995). The second assumption is that the concentration of gadodiamide in the perfusate is the same as that in the ECS. There is evidence that the interstitium of certain tissues has a strong net negative charge density that may reduce the concentration of an ionic contrast agent (Donahue et al., 1994). Gadodiamide, however, is nonionic and is expected to be largely unaffected by such a charge density. Further, the 15 minute period allowed for perfusate exchange is likely sufficient for an equilibrium to develop between gadodiamide in the perfusate and ECS.

A more difficult assumption to address is that of the proton exchange rate between ICS and ECS. It is normally accepted that this rate is fast when clinical doses of gadodiamide are administered (Donahue et al., 1994). However, in the third T1 measurement of the brain slices the ECS concentration of gadodiamide is 4 mM, 40 times the clinical whole-body concentration. Following the method of Barsky et. al. (Barsky et al., 1997), fast exchange may be assumed provided:

$$\frac{k}{10} > (1 - f_{ICS})\left(\frac{1}{T_{1(ECS)}} + r_1.[Gd] - \frac{1}{T_{1(ICS)}}\right) \qquad [7.5]$$

Table 7.1. Estimates of the parameters defined in Eqs. [1] and [4] obtained from four brain slices.

	$S_0(0)^1$	$S_0(1)^1$	$S_0(4)^1$	A (no units)	T1(0) (s)	f_{ICS} (no units)
Slice 1	896	885	538	0.97	2.12	0.57
Slice 2	1039	1007	655	0.98	2.15	0.64
Slice 3	991	955	586	0.97	2.07	0.57
Slice 4	1039	1009	665	0.98	2.16	0.65
Mean				**0.97**	**2.12**	**0.61**
SD				**0.01**	**0.04**	**0.04**

[1] Estimates of the fully relaxed signal, S_0, in aCSF, 1 mM gadodiamide and 4 mM gadodiamide.

where k is the exchange rate. If we assume that T1(ECS) = T1(perfusate), and that the perfusate contains 4 mM gadodiamide, then the exchange rate must exceed 50 s^{-1}. Very little data has been published on the exchange rate of protons in brain tissue. A rate of 33 s^{-1} was estimated for glial cells in bovine optic nerve at 20°C (Stanisz et al., 1997b) and a rate of 50 s^{-1} was estimated for cultivated perfused glial cells at 37°C (Pfeuffer et al., 1998). We are unlikely to be significantly slower than an exchange rate of 50 s^{-1} and our data provides strong support for the fast exchange assumption. There is no evidence for biexponential behavior in any of the T1 recovery curves and each brain slice showed a linear increase in 1/T1 as a function of gadodiamide concentration.

The application of this approach to measuring changes in cell volume fraction was demonstrated in a single brain slice. Following a hypertonic challenge to the slice (adding 60 mM mannitol to the perfusate), the ECS volume fraction is expected to increase by approximately 25% (Huang, Somjen, 1995). Before the challenge, addition of 0.125 mM gadodiamide indicated an ECS fraction of 0.47. Upon addition of the mannitol, this fraction grew to 0.59, a 26% increase in ECS volume.

According to our model, the average fraction of the NMR signal arising from the cellular volume of our 4 slices is 0.61. This value is somewhat larger than the value of 0.47 measured previously using a diffusion analysis (Buckley et al., 1999). The shorter TE used in the present design reduces the influence of the difference in T2 relaxation time of the ICS and ECS. One issue neglected in our previous study (Buckley et al., 1999) is the difference in spin density between the ICS and ECS. If we assume relative spin density values of 0.71 and 0.95 for the ICS and ECS respectively (Pirkle et al., 1979), the cell volume fraction estimate increases to 0.67 and the ECS volume fraction

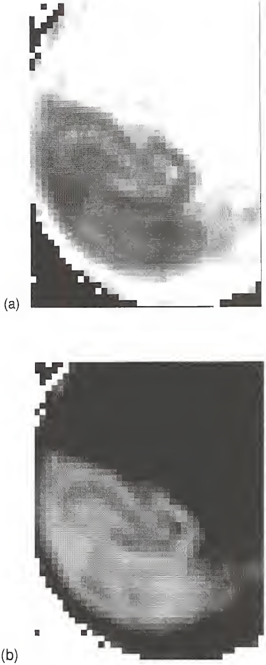

Figure 7.3: Compartmental volume fraction maps. Signal intensity is proportional to the difference of 1/T1 in aCSF and 1 mM gadodiamide (a) and (1 – difference) (b). Note the brightness and darkness of the perfusate in (a) and (b) respectively (effective ECS fraction ≈ 1 and ICS fraction ≈ 0) and the heterogeneity of volume fractions in the brain slice (mean ECS volume fraction 0.28, range 0.13 to 0.61).

is reduced to 0.33. This is the same as that measured by Newman et. al. (Newman et al., 1995) in the hippocampal slice using a radiotracer (^{14}C-PEG) technique, but still larger than that measured by Perez-Pinzon et. al. (Pérez-Pinzón et al., 1995) using iontophoresis.

A number of distinctions between these studies may explain the variable estimates of ECS fraction. Differences in slice preparation methods (e.g., age of animals, temperature of animals during slice extraction, aCSF composition) are known to result in differences in slice physiology. These differences have been estimated to account for an additional 0.05 to 0.08 ml/g in the measured ECS (Newman et al., 1995). Moreover, the radiotracer technique measures the average ECS over the entire slice, including the cut edges. The iontophoresis measurement is limited to small regions inside the slice surrounding the tip of the microelectrodes. A significant advantage of the NMR imaging technique is in its ability to produce maps of ECS fraction. Though we have reported mean values of cell volume fraction, calculated from regions of interest encompassing the entire slice, estimates can be made on a voxel by voxel basis. In figure 7.3 it is clear that there exists an intra-slice heterogeneity of ECS fraction.

In summary, the technique described provides a simple method of determining cell volume fraction in the perfused rat hippocampal slice. The assumptions required appear to be satisfied up to the 4 mM dose of gadodiamide and the results match previous estimates of ECS volume fraction. With the theory established above within the limits of fast exchange, subsequent measurements require only a single dose of gadodiamide.

CHAPTER 8
COMPARTMENTAL WATER DIFFUSION IN PERFUSED HEART SLICES

In order to further understand the origins of bi-exponential water diffusion in situ, experiments on an isolated perfused heart slice preparation was carried out using the same perfusion chamber as described in chapter 3 for brain slices. The results indicate that like brain the heart exhibits bi-exponential water diffusion behavior.

Introduction

Recent reports in the literature have used myocardial diffusion imaging to provide information regarding the micro-structural organization of the heart (Hsu et al., 1998;Scollan et al., 1998; Garrido et al., 1994) and uncovered alterations in the apparent diffusion coefficient (ADC) of water that occur during myocardial ischemia (Hsu et al., 1998). Moreover, the prior demonstration that myocardial diffusion imaging can be performed *in vivo* has dramatic implications for clinical applications. Findings from rat brain slices (chapters 5, 6) the *in vivo* rat brain (Niendorf et al., 1996) and recently the human brain (Mulkern et al., 1999) suggest that the ADC of water may be biexponential in these tissues, raising the possibility that multiple water compartments are being observed. A recent report has shown the feasibility of performing multi-exponential diffusion imaging in a clinical MR scanner (Mulkern et al., 1999), providing evidence that multi-compartmental diffusion imaging may eventually have direct clinical application. The current study was performed to determine if non-mono-exponential water diffusion exists in the heart as previously reported for neuronal tissue.

Myocardial fiber orientation plays a significant role in the patterns of electrical depolarization, the development of myocardial stress and strain, and indirectly has a role in local myocardial perfusion and oxygen consumption. Hsu et al. (1998) recently reported the first quantitative correlation of histologically determined myocardial fiber orientations in the excised right ventricle with the principle eigenvector of the diffusion tensor. Subsequently, a correlation between the anatomical microstructure of the intact perfused rabbit heart (myocardial fiber angle orientation and laminar sheet structure) with the principle and tertiary eigenvectors of diffusion was reported (Scollan et al., 1998). This work provided direct evidence that diffusion tensor imaging could furnish information regarding anatomical structure that was previously available through laborious histological examination on fixed tissue.

In addition, myocardial fibers are altered in a number of disease states, such as ischemia (Olivetti, White, 1990), diabetes, hypertensive cardiomyopathy (Olivetti et al., 1988), and hypertrophy. Recent advances have permitted the clinical application of diffusion weighted imaging techniques to the study of the heart, where it may provide new information regarding the efficacy of treatment or enhanced detection of pathophysiological alterations. We have previously reported decreased ADC in the myocardium following acute regional ischemia (Hsu et al., 1998). In contrast to the temporal characteristics of diffusion changes that have been observed in the brain following ischemia (Hsu et al., 1998), changes in the ADC of water in the ischemic heart are delayed, and changes in T2-weighted images precede observed changes in ADC images. The decrease in ADC reported in both brain and heart has been attributed to cytosolic swelling due to a loss of ionic homeostasis, though other mechanisms may contribute to changes in ADC.

Previous studies in the heart (Hsu et al., 1998; Scollan et al., 1998; Garrido et al., 1994; Niendorf et al., 1994), were limited by the strength of the diffusion gradient strengths and subsequently small b-values. As a result, the tensors that were calculated (Hsu et al., 1998; Scollan et al., 1998) were biased toward the fast component of diffusion (assuming two compartments); the slow component (if present) may not be apparent at b-values less than 1000 s/mm^2. The slow component might have a substantial contribution to the overall tensor calculations depending on relative sizes of the compartments corresponding to the fast and slow components. Moreover the decreased diffusion that has been observed in the heart (Hsu et al., 1998) following ischemia could be a result of alterations in the relative size of these compartments, rather than a uniform reduction of water ADC in the affected region. The goal of the present study was thus to determine if the ADC in heart tissue is mono or multiexponential and discuss the impact of this on the measurement of the ADC and the diffusion tensor in the heart.

Materials and Methods

Sample Preparation

New Zealand White male rabbits (1.5 kg) were sacrificed by anesthetic overdose (ketamine 44 mg/kg, i.m.; xylazine 15 mg/kg, i.m.) followed by rapid exsanguination. Hearts were isolated and placed in ice-cold (4°C) modified St. Thomas' cardioplegic solution that had been equilibrated with 95% O_2 / 5% CO_2. Perfusate contained (in mM): NaCl, 110, KCl, 16; $MgCl_2$, 16; $NaHCO_3$, 10. Dextrose (5mM) and adenosine (1mM) were added to improve long term viability, and the pH was adjusted to 7.4. Hearts were perfused for approximately 10 minutes (at 19°C) to remove blood from the vascular compartment and to arrest the heart. The hearts were then removed, placed into ice-cold buffer, and sectioned perpendicular to the long axis of the left ventricle (see Figure 1). A section of the left ventricular free wall was isolated and coarse sectioned into a block of tissue approximately 5 mm^2 by 3 mm thickness. This was subsequently finely sectioned into several slices spanning the transmural direction of the left

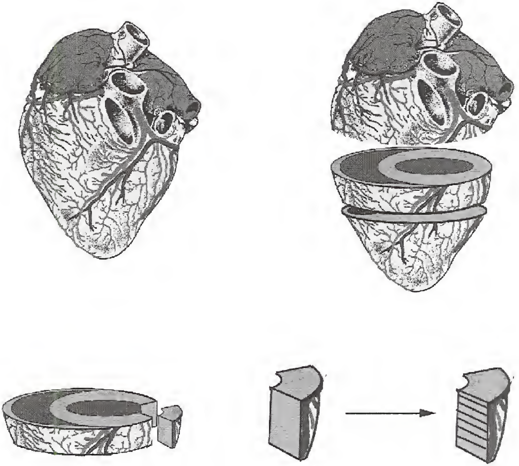

Figure 8.1. Schematic representation of the myocardial tissue slice preparation. The heart (top left) is sectioned axial to make a disc of tissue (top right). A segment is cut from the ventricular wall in the disc (bottom left) and sliced axially to produce the heart slices (bottom right).

ventricular free wall (400-700 μm thickness). In three of the hearts, the papillary muscle was also isolated and sectioned perpendicular to the long axis of the ventricle (2 mm diameter, 500-900 μm thickness). The tissue slices were placed into a tissue perfusion chamber described in chapter 3 which was inserted into a 10mm NMR tube, the temperature maintained at 19°C, and the perfusion rate adjusted to 1 ml/min. The flow was stopped during the diffusion imaging sequences to minimize motion artifacts.

NMR Imaging

Images were acquired on a Varian 600 MHz spectrometer. A diffusion weighted sequence was used with a spatial resolution of 117 x 156 x 300 microns, TR=2s, TE=30ms, 128x64, NA=2, for a total imaging time of 4.3 minutes per image. Diffusion time was 12 ms. The range of b-values (applied in the z-axis) used was: 166, 220, 321, 490, 918, 1734, 3602, 6408 (s/mm^2). A bi-exponential function was fitted to the data as previously described (chapter 5):

$$SI = M(0) \bullet \left[f_1 \bullet e^{(-bD_1)} + (1 - f_1) \bullet e^{(-bD_2)} \right] \qquad [8.1]$$

where SI is the signal intensity, M(0) is the magnetization in the absence of diffusion gradients, f_1 is the signal fraction characterizing the slow diffusion component, D_2 is the fast diffusion coefficient, and D_1 is the slow diffusion coefficient.

Statistical analysis

Data was analyzed by defining regions of interest that corresponded to the tissue, the surrounding superfusate, and the area outside the coil (for determination of signal to noise ratio). Statistical analysis was performed using non-linear curve-fitting with statistical significance established at $p < 0.05$.

Results

A total of 10 slices were obtained from 4 hearts. Seven of the slices were from the LV free wall, and three were samples of papillary muscle from different hearts. Figure 8.2 shows diffusion weighted images from one slice. At the higher diffusion weighting (Figure 8.2b) the signal from the faster diffusing surrounding perfusate is suppressed leaving signal only from the heart slice itself. At these spatial resolutions the image is unremarkable and no internal structure is discerned with the diffusion gradient in the z-orientation, as expected. All tissue samples exhibited a similar bi-exponential decline in signal intensity when plotted as a function of diffusion gradient b-values. Preliminary analysis of the ADC based on anatomic location showed no differences between the tissue obtained from the papillary muscle and the LV free wall; as a result, all tissue samples have been grouped for clarity (see Figure 8.3). Of the ten slices that we studied, three did not give reliable bi-exponential fits in the early time points, and thus seven slices were analyzed. The results indicate the calculated ADC of the fast component of diffusion (D_2) corresponds to $7.2 \pm 0.7 \times 10^{-4}$ $\text{mm}^2\text{sec}^{-1}$, and comprises 82±3% of the total diffusion constant. The slow component of diffusion (D_1) was estimated at $6.0 \pm 3.3 \times 10^{-5}$ $\text{mm}^2\text{sec}^{-1}$.

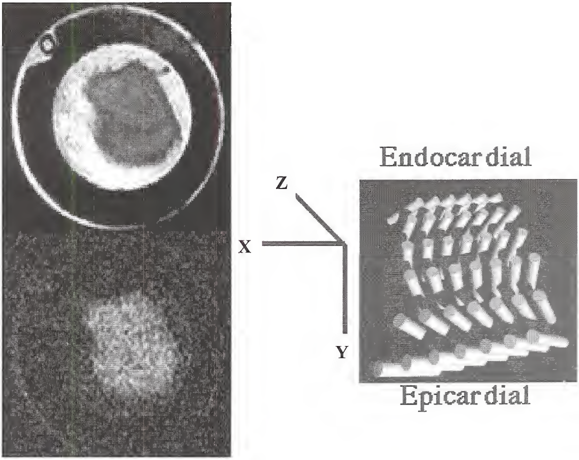

Figure 8.2. Representative images and illustration of myocardial fiber angle orientation. (a) Lightly diffusion weighted image of the heart slice surrounded by perfusate, b = 166 s/mm^2 . (b) Heavily diffusion weighted of the same slice (different windowing), b = 1734 s/mm^2. The perfusate signal has dropped below noise level. Both images show relatively homogeneous tissue contrast. (c) Schematic of myocardial fiber angle orientation relative to the images as one progresses from epicardial to endocardial regions. The diffusion gradient is oriented along the z direction (out of the page as indicated).

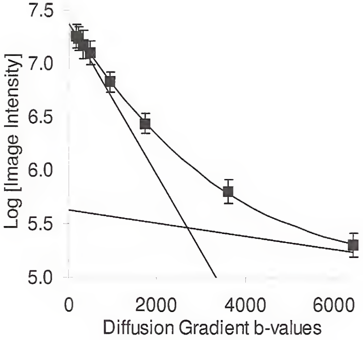

Figure 8.3. Plot of the signal intensity as a function of diffusion gradient b-values. Data points represent the mean intensity of ten separate slices, and are shown with the corresponding standard deviation. Also shown are the exponential fits for both the fast and slow components of diffusion. Note that a mono-exponential dependence would be evident as a linear fit on such a semi-log plot, rather than curvilinear behavior as observed here.

Discussion

These data demonstrate for the first time that diffusion in myocardial tissue is non-mono-exponential, and can be fitted by a bi-exponential expression as previously reported for brain tissue (chapter 5, 6). This has been speculated to arise from water compartmentation which may possibly arise from the intra- and extracellular compartments. Evidence for the source of the two compartments remains circumstantial, although experiments performed with ouabain (chapter 5) and NMDA (chapter 6) in brain tissue slices have indicated that the increased intracellular volume that accompanies ouabain or NMDA administration corresponded to similar changes in the compartment size for the slow component of diffusion. Further experiments are required to elucidate the origin of this compartmentation.

The ADCs that were measured in heart tissue slices ($7.2 \pm 0.7 \times 10^{-4}$ mm^2s^{-1} for the fast component, and $6.0 \pm 3.2 \times 10^{-5}$ mm^2sec^{-1} for the slow component) are similar to those previously reported in brain slice preparations ($9.6 \pm 1.0 \times 10^{-4}$ mm^2sec^{-1} and $6.0 \pm 0.6 \times 10^{-5}$ mm^2sec^{-1}, respectively) (chapter 6). However, if a two compartment model is used, the relative distribution between the fast and slow compartments are different in heart slices compared to the brain slice preparation (0.82±0.03 vs. 0.55±0.05 for the fast component, respectively). As discussed in our previous work (chapters 5, 6), this may be due to differences in the T2 of the tissues. Cardiac tissue is known to have a T2 when fit to a monoexponential that is nearly half that of the brain (Bottomley, 1988), and one group (Donahue et al., 1994) has measured the T2 in isolated rat hearts to be biexponential. Presuming the short T2 component to be intracellular, then a small ratio of the intracellular to the extracellular T2 would explain both the short average T2 obtained by a monoexponential fit and the increased volume fraction of the fast diffusing compartment. This speculation is further evidenced by the observation that Niendorf et al. (Niendorf et al., 1996) reported a fast diffusion compartment size of 0.80±.02 for healthy adult rat brain measured *in vivo* (i.e. larger than in the brain slice) but used longer echo times in their measurements which would also weight their results toward the longer T2 compartment. Further studies measuring T2 on isolated brain and heart slices are required, with cell volume perturbations and verification by alternate techniques. Additionally, the heart has a larger vascular volume than that of the brain (14-22% versus approximately 5%). Since the vascular compartment may contain perfusate with a longer T2 and diffusion coefficient it is likely to contribute to the fast diffusion component. Additional studies are underway to determine if the vascular compartment can be identified (e.g., if the diffusion data are tri-exponential - see below).

Non-monoexponential diffusion has been observed in excised tissue *in vitro* using spectroscopic techniques (Henkelman et al., 1994), but no attempt was made to interpret these findings. Although cardiac tissue was not examined, a biexponential fit to data from excised muscle (bovine quadriceps) gave fast and slow diffusion components with ADCs of 1.3 x 10^{-3} mm^2s^{-1} and 7 x 10^{-5} mm^2s^{-1}, and a fast component fraction of 96%. Bearing in mind that this bovine tissue was not perfused, not cardiac tissue, was examined at 25°C and with a different diffusion time of 20msecs, these data are comparable to those reported in this paper on perfused heart slices. It is interesting to note that biexponential behaviour was observed on several other tissue types in Henkelman et als *in vitro* study (Henkelman et al., 1994), implying that the compartmental nature of biological tissue with respect to the water diffusion coefficient may be generally applicable.

These observations also have important implications for both the interpretation of diffusion tensor measurements in myocardial tissue (Hsu et al., 1998), (Scollan et al., 1998), as well as the temporal changes that have been observed in the ADC of ischemic myocardial tissue (Hsu et al., 1998). It is reasonable to assume that the small b-values that were applied in the previous determination of the eigenvalues and eigenvectors of diffusion in the heart (Hsu et al., 1998), (Scollan et al., 1998) reflect a general bias toward the fast diffusing component. However, information regarding the tensor orientations of the slow component remain unresolved. Furthermore, it is not known if the relative size of the diffusion compartments change under pathophysiological conditions. The progressive decrease in ADC observed in the isolated heart following ischemia could reflect a relative redistribution of water within the two diffusion compartments, without a change in the diffusion coefficients of the compartments themselves. This would be similar to the changes recently reported in brain slices following administration of ouabain (chapter 5) and NMDA (chapter 6).

However, the apparent diffusion coefficient of the fast component in our isolated heart slice preparations is significantly less than the ADC values determined for the intact perfused arrested heart (Garrido et al., 1994) even when temperature effects are taken into account ($1.1 - 1.8 \times 10^{-3}$ mm^2s^{-1}). This may reflect myofibrillar size and angle reorientation (resulting from either tissue sectioning or ischemia), increased cytosolic swelling of the slice preparation, or a collapse of the intravascular compartment in the slice preparation (reported to be approximately 14-22% of the myocardial volume.

Myofibrillar Orientation and Cell Size Effects

Although acknowledged to occur relatively rapidly (2 hours) following myocardial ischemia, there is no evidence that a rearrangement of myofibrillar orientation occurs in the time frame encompassed by these studies (approx. 35 minutes). Moreover, the orientation of the diffusion gradients (along the z-axis) should result in a relatively homogenous image intensity since the fiber orientation would be largely parallel to the gradients. This homogenous image intensity was observed in all of the tissue slice preparations that were examined, suggesting that gross rearrangements of myofibrillar orientation did not occur in this preparation (see Figure 8.2). It is interesting to note that under pathophysiological conditions (e.g.hypertrophy, diabetes, or ischemia/reperfusion) changes in myocyte fiber orientation may complicate issues of analysis based solely on ADC calculations. Perhaps of greater concern to this study is the observation that the rabbit myocyte is approximately 80-100 µm in length (10), which raises the possibility that a significant portion of the cells that border the cleavage planes for the ventricular slice preparation may be damaged. Since the tissue slice itself is approximately 400-800 µm in thickness, a fraction of the cells will be compromised, and this will presumably be reflected by elevated values for the apparent diffusion coefficient of water in the tissue. However, by limiting the through-plane MR slice thickness to 300 µm, we sought to minimize any contribution from damaged cells located along the cleavage planes. The observation that the fast component of the ADC that was measured is consistent with that previously reported at this temperature suggests we were successful in avoiding this potential artifact. Moreover, ADC measurements made in tissue slices isolated from papillary muscle (500-800 µm) had ADC values that were not significantly different from the tissue slices isolated from the LV free wall (400-800 µm).

Cytosolic Swelling in Myocardial Tissue

Cell swelling within the myocardial tissue might be expected to lower the apparent diffusion coefficient, although work from this laboratory suggests that the ADC of the two compartments do not change with cytosolic swelling, but rather that the relative size of the compartments is varied (chapter 5). Moreover, issues of cell swelling might be expected to become somewhat more relevant under normothermic conditions (i.e., 39°C), with tissues at the limit of diffusion for oxygen or metabolic substrate delivery (>500 µm thickness), or under conditions of low- or zero-flow. This was not the case in these experiments. Combined with the decreased temperature, the presence of the cardioplegic solution results in very low oxygen consumption for this tissue (Scollan et al., 1998). Recent diffusion estimates have also been reported using the excised canine right ventricle (Hsu et al., 1998). The size of the right ventricular tissue sample that Hsu et al. examined was 1.7 x 2 x 0.55 cm, and the total time required for the study was 3.5 hours. The tissue was rinsed and maintained in a chilled Ringer's solution during the imaging protocol. In contrast, the LV free wall slices that were studied in this report were approximately 0.4 x 5 x 5 mm, and were superfused at a rate of 1 ml/min with well oxygenated cardioplegic solution. Although the flow was turned off during the diffusion measurements, the entire diffusion imaging protocol did not exceed thirty five minutes. Papillary slices tended to be somewhat thicker (500-800 µm), yet did not result in diffusion coefficients that were different from those measured in the LV free wall, suggesting that viability was not compromised in the tissue samples that we studied.

Vascular Component to Diffusion

The recent report by Hsu et al. (Hsu et al., 1998) examined the histological correlation of myofibrillar orientation with respect to the principle eigenvector of diffusion. This study was performed in excised (i.e., non-perfused) tissue samples of canine right ventricle at 20°C, and measured an average principle eigenvalue of $0.94 \pm 0.28 \times 10^{-3}$ mm^2sec^{-1}. Subsequently, our laboratory reported histological validation of the correlation between the observed eigenvectors of diffusion with myocardial micro-architecture in the intact perfused rabbit heart (Scollan et al., 1998). Although the measurements were made at the same temperature as those by Hsu et al., the values determined for the principle eigenvalue ranged from $1.5\text{-}1.8 \times 10^{-3}$ mm^2sec^{-1} (depending on their transmural position within the ventricular wall). Since the value reported by Hsu et al. is similar to that reported in this study (0.72 ± 0.07 x 10^{-3} mm^2sec^{-1}), and both tissues were not perfused by direct vascular flow (although the tissue slice preparation was bathed in a exchanging nutrient- and oxygen-rich cardioplegic solution), it is possible that the decreased value for the diffusion coefficient that was observed in both studies might be due to the collapse of the vascular compartment prior to measurement. If true, then a more appropriate model for fitting diffusion in the myocardium might be a tri-exponential, rather than the bi-exponential model that was employed here. This will require a range of b-values employed to adequately sample the very fast, the fast, and the slow components of diffusion; these studies are currently underway.

In conclusion, multiexponential behavior has been observed for the first time in the diffusion coefficient of water in heart tissue. It is speculated that the diffusion is at least biexponential, and may reflect intra/extracellular compartmentation. However other compartments must be considered (e.g. vascular). Thus macroscopic MR measurements in tissues appear to provide quantitative compartmental information at the microscopic, cellular level. These observations have major implications for the interpretation of diffusion tensor measurements in cardiac tissue and changes in the ADC following pathophysiological insults (e.g., ischemia).

CHAPTER 9
WATER DIFFUSION MEASUREMENTS IN A MIDDLE CEREBRAL ARTERY OCCLUSION MODEL OF FOCAL ISCHEMIA

To further test the results of experiments described in previous chapters on perfused tissue slices, a middle cerebral artery occlusion model of focal ischemia is developed and tested in this chapter. The results indicate that this intact animal model behaves in a similar fashion as human brain in clinical MR imaging experiments with a decrease in the average ADC following ischemia. In addition, the neuroprotective effects of estrogen is tested with the MCA occlusion model with reperfusion injury.

Introduction

As discussed in chapter 3, stroke is the third leading cause of death and the most common cause of disability in the United States (Choi 1990). The majority of strokes occur when perfusion to the middle cerebral artery is reduced secondary to occlusion, producing a region of focal cerebral ischemia and a subsequent cascade of neuronal and microvascular changes ultimately leading to infarction (Macdonald and Stoodley 1998). The clinical goal is rapid identification of an ensuing stroke and then restore flow to the ischemic tissue. However, reperfusion of previously ischemic tissue is not without risks. In fact, the evidence is that reperfusion may have associated reperfusion associated injury and the therapeutic window for restoring flow is within the first 3 to 6 hours of the onset of ischemia (del Zoppo et al., 1997). With the availability of thrombolytic therapy like TPA and streptokinase, it is essential to develop new neuroprotective approaches to project injured neurons and thus, prolong the effective therapeutic window (del Zopoo et al., 1997).

Observations from several laboratories indicate that estrogens are potent neuroprotective agents and decrease focal ischemia-induced infarction size by about 50% (Simpkins et al., 1997; Shi et al 1997; Toung et al., 1998; Dubal et al., 1998). The histologic methods used in these previous studies gave insight into the basis for estrogen action but dynamic assessment of estrogens' protective effects during occlusion and reperfusion was difficult. In the present study, we applied NMR imaging techniques to analyze noninvasively, for the first time, estrogen's temporal and spatial effects in focal cerebral ischemia.

Materials and Methods

Animals

Sprague-Dawley female rats (200-225 grams body weight) purchased from Charles Rivers Laboratories, Inc. (Wilmington, MA) were housed in pairs in hanging, stainless steel cages in a temperature controlled room (25+/-1 ^{O}C) with daily light cycle (light on 0700 to 1900 h daily) for a minimum of 3 days before surgery. All rats had free access to Purina Rat Chow and tap water. All procedures performed on animals were reviewed and approved by the Institutional Animal Care and Use Committee of the University of Florida before initiation of the study. Two weeks before the focal ischemia was induced, all rats were ovariectomized (OVX) to eliminate endogenous estrogens. Rats in the OVX + E_2 group were administrated a single dose of 17 β-estradiol (E_2) (100 μg /kg) two hours before focal ischemia surgery, while those in the OVX group received no estrogen replacement.

Focal Ischemic Model

Middle cerebral artery (MCA) occlusion was used to achieve focal ischemia. Following administration of anesthetics, the left common carotid artery (CCA), external carotid artery (ECA) and internal carotid artery (ICA) on the left side were exposed and dissected through a midline cervical incision. A 3-0 monofilament suture was introduced into the left ICA lumen and gently advanced until resistance was felt, indicating MCA occlusion and compromised blood flow. The suture was kept in place for 60 minutes and then withdrawn to return flow to MCA during the reperfusion phase. The operating procedure was performed within 20 minutes with minimal blood loss. Rectal temperature was monitored and maintained between 36.5 and 37.0 ^{0}C during the entire surgical procedure.

NMR Imaging

Imaging was performed at 4.7 T 33 cm magnet with a Brucker Console, using an actively shielded gradient set capable of 220 mT/m. The animals were supported on a cradle and their heads placed in a home-built birdcage coil with a 5 cm outer diameter (operating in quadrature transmit/receive mode). Following the acquisition of scout images, 6 coronal plane images were prescribed beginning 3 mm behind the olfactory bulb. The slices were each 1.5-mm thick and were separated by 2 mm. All images were acquired over a 5 cm field of view using a 128 x 128 matrix (0.39 x 0.39 mm in-plane resolution) with a repetition time (TR) of 1.75 s and 2 signals averaged. Each set of 6 images was acquired in 7.5 min. Diffusion-weighted images (DWI) were acquired using a standard pulsed gradient spin echo technique with an echo time (TE) of 33 ms. The gradient pulses were each applied for 9 ms and were separated by 13 ms around the 180° refocusing pulse. The gradient amplitude used was 152 mT/m resulting in a b-value of 1400 s/mm^2. The T2-weighted images (T2WI) were acquired using a standard spin echo technique with a TE of 75 ms. Both DWI and T2WI were captured sequentially for each animal 30 minutes into the MCAO (the occlusion interval), and 2, 4, 6 hours after withdrawal of the monofilament (the reperfusion period).

Histological Staining

The animals were decapitated, and whole brains were dissected coronally from the olfactory bulb to the cerebellum in a metallic brain matrix (model RBM 4000C, ASI Instruments, Inc., Warren, MI). Sections were then made at 3, 5, 7, 9 and 11 mm posterior to the tip of olfactory bulb and were correlated to the MRI dissection. Sections were immediately stained by immersion in 2% 2, 3, 5-triphenyl tetrazolium chloride (TTC) at 37 ^{0}C for 30 minutes (2) and preserved in 10% formalin solution.

Quantitation of Ischemic Lesion Size and Intensity

The ischemic lesion sizes, as well as lesion intensity, of MR and TTC staining images were anatomically matched and measured using the Image-Pro Plus software (Media Cybernetics). The lesion area was sub-divided to cortical and sub-cortical areas according to neuroanatomic landmarks. The percentage of the lesion size over the whole brain coronal section was calculated. The lesion intensity ratio was calculated when the intensity of the non-lesioned hemisphere was taken as 1.

Statistics

The Mann-Whitney U test was applied to determine the significance of the difference between OVX and OVX + E_2 groups. The linear regression statistics was used to correlate measurements of lesion sizes between TTC staining and MRI. R square was calculated to analyze the coherence of the two measurements. A value of $p< 0.05$ was considered significant.

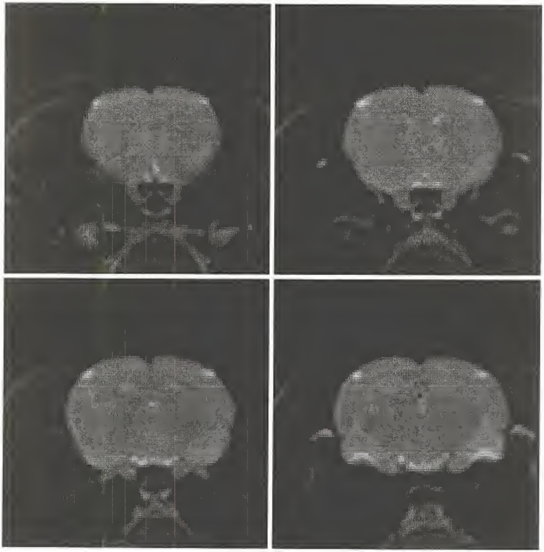

Figure 9.1. T2 weighted NMR images acquired 30 minutes into a one hour MCA occlusion. The panels show that conventional T2 images are not sensitive to early ischemic changes

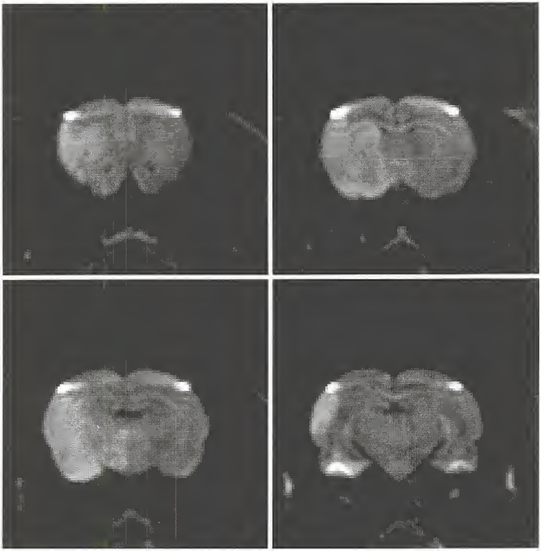

Figure 9.2. Diffusion weighted NMR images were acquired 30 minutes into a one hour MCA occlusion (same animal as in figure 9.1). Ischemica regions are hyperintense.

Results

Figure 1 illustrates that conventional T2 weighted NMR imaging is insensitive to early ischemic changes while figure 9.2 shows that diffusion weighted (DW) NMR imaging can reveal ischemia induced changes as early as 30 minutes post occlusion. The total lesion size in the occlusion phase was similar in both groups (33.7% and 33.5% of the whole slice in the control and E_2 treated groups, respectively), but was larger in cortical regions in the control group (26.5% vs. 17.1% in E_2 treated). During the reperfusion phase, the lesion size remained constant in the control group but decreased in the E_2 treated group by 50-60% ($p<0.05$). This lesion size reduction was maintained at all time points after reperfusion (2, 4, and 6 hours). (figure 9.3). Figures 9.4 and 9.5 are representative image sets showing lesion sizes in a control and an E_2 treated animal respectively. This size reduction was primarily located in cortical regions (figure 5). For comparison, figure 9.6 shows the extent of an ischemic lesion 24 hours after a 1 hour transient MCA occlusion using a TTC staining which is a histological technique which requires animal sacrifice. The lesion size is similar to that measured with conventional T2 and DW imaging at 24 hours.

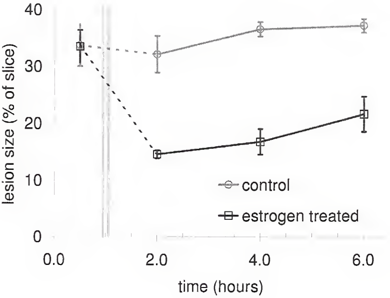

Figure 9.3. Ischemic lesion sizes (total). The red line indicates mean lesion size in non-treated control animals (n=4). The blue line represents mean lesion size in E_2 treated animals (n=3). Data expressed as % of total slice, mean + SEM

DISCUSSION

Early detection and localization of potentially reversible ischemic damage is crucial for designing clinical therapeutic interventions against stroke. The present study demonstrates that MR imaging can provide a wealth of information about the initiation, progression and localization of cerebral ischemic events. This is applied in this study to define the location and the component of the developing ischemic lesion affected by estrogens. Diffusion weighted MR imaging which is sensitive to the random movement of water molecules is thought to reveal the early changes associated with stroke induced-cytotoxic edema. On the other hand, conventional T2 weighted MR imaging is sensitive to vasogenic edema which occurs later in the pathophysiology of stroke. It can detect subacute ischemic damages, although it fails to show acute ischemic changes. Histological TTC staining of ischemic lesions requires disruption of normal mitochondria function to detect the ischemic area. TTC staining lesions are indicative of neuronal dysfunction. It is noteworthy that TTC staining during MCAO does not reveal the lesion, while diffusion weighted MR imaging does, but by 6 hours of reperfusion, TTC staining correlates well with MRI measures of reperfusion-associated neuronal damages.

The early detection of ischemic lesion volumes by diffusion-weighted imaging is predictive of clinical severity and outcome of stroke patients. In the present study, DW imaging was the earliest detected evidence of cerebral ischemia and was the parameter most affected by E_2-treatment. This reduction in DW signal intensity by E_2-treatment can account for most of the observed beneficial effects of estrogen pre-treatment (Simpkins et al., 1997; Shi et al 1997; Toung et al., 1998; Dubal et al., 1998).

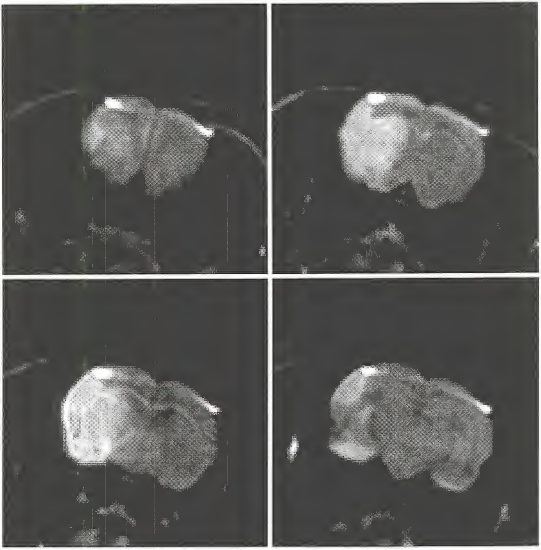

Figure 9.4. Non-E_2 treated controls Panels are DW images showing lesion sizes 2 hours after reperfusion in a control rat.

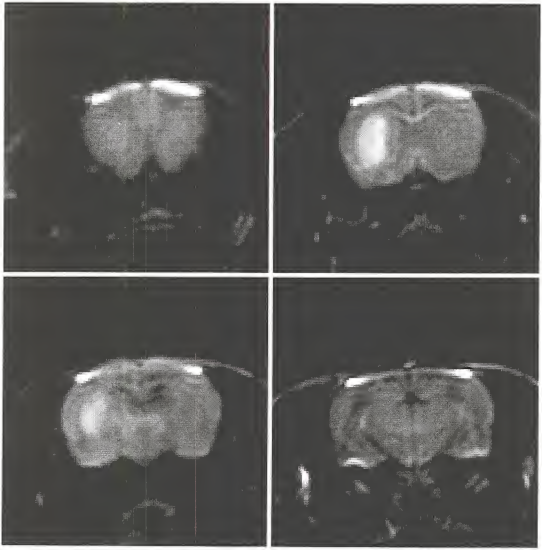

Figure 9.5. E_2 pre-treatment. Panels are DW images showing lesion sizes 2 hours after reperfusion in an estrogen treated rat. The size of the lesion is markedly reduced (compare with figure 9.4).

E_2-treatment appears to exert part of its protective effects by preventing permanent damage associated with reperfusion. Reperfusion causes structure alteration of the Golgi apparatus and compromises the energy supply to brain cells. Hoehn et al. (1996) applied biolumninescence and fluorescence techniques to correlate DW imaging and energy disturbance during MCAO, and found a depletion of ATP in the ischemic core while the area of tissue acidosis spreads beyond the ATP-depleted core region. These findings are consistent with our TTC staining observation that the white core infarct region is surrounded by the pink ischemic penumbra (Simpkins et al., 1997; Shi et al 1997; Toung et al., 1998; Dubal et al., 1998). The close correlation between DW imaging and TTC staining suggests DW imaging is predictive of energy deficits during early stroke. Part of the estrogen effect occurs during the reperfusion phase which may explain the finding that estrogen treatment is effective up to 3 hours after the onset of ischemia (Simpkins et al., 1997)

Reperfusion of ischemic tissue can produce an influx of oxygen followed by an accumulation of oxygen-derived free radicals (Macdonald and Stoodley 1998). The oxidative stress may damage unsaturated fatty acids in the plasma membrane, which in turn could increase calcium influx into the cell and worsen ischemia-initiated neuronal injuries. The evidence indicate that estrogens can attenuate free radical-induced peroxidative damage (Behl et al., 1997; Green and Simpkins, 1998.), modulate calcium homeostasis in the neurons (Mermelstein et al., 1996), and interact with neurotrophins, their receptors and signaling pathways (Sohrabji et al. 1994). All these effects of estrogen may contribute to its protective effects during reperfusion.

The suggestion that estrogens may have significant protective properties during reperfusion could have profound impact on the treatment of stroke. Many centers

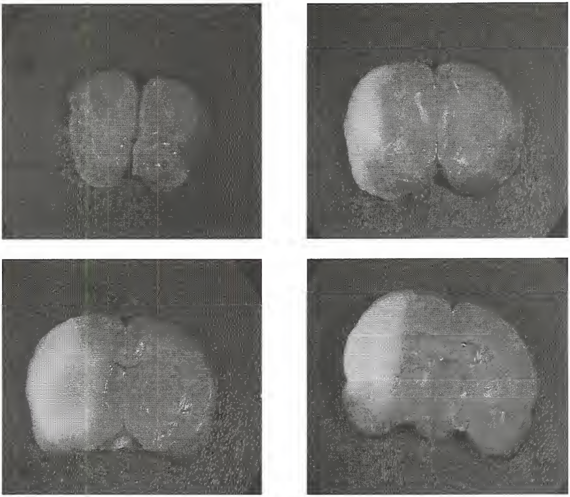

Figure 9.6. TTC stained histological sections. Panels indicate extent of ischemic lesion 24 hours after a 1 hour transient MCA occlusion. Infracted areas appear white. The main limitation of TTC staining is that it is a terminal experiment.

in the United States are now treating stroke acutely, using thrombolytic agents to dissolve the offending clot. Clinical trials have demonstrated a significant clinical improvement in such patients, especially when the treatment is delivered within 3 hours of stroke onset. However, reopening an occluded intracranial vessel, have lead to may include acute or delayed intracerebral hemorrhage, and reperfusion hyperemia and progressive to infarction despite a patent lumen. The identification of an agent that can protect against such mechanisms, if delivered before or early after vessel patency is restored, could rescue an otherwise pre-programmed infarction, and perhaps also decrease hemorrhagic risks by stabilizing energy metabolism in vascular endothelium.

The present study suggests that estrogens are good candidates for producing such effects. As during reperfusion, E_2 treatment dramatically decreases ischemic lesion sizes and intensities experimentally, as demonstrated by both DW and T2W iamging, and these decreases are almost exclusively located in cortical regions.

In summary, we applied MR imaging techniques to demonstrate the temporal and spatial ischemic changes in a focal ischemic animal model. We have demonstrated that estrogens selectively protect cortical tissue from ischemic damage and that this protection is primarily exerted during the reperfusion phase of damage. This study strongly suggests that estrogen could have direct clinical applications and potentially could widen the therapeutic window by protecting against thrombolytic-induced reperfusion injury.

CHAPTER 10
CONCLUSION

This work involves the development of a perfused tissue slice preparation for use in high field NMR imaging to quantitatively study the origins of NMR contrast in biological tissue, particularly water diffusion behavior in the central nervous system following various physiological stressors using an isolated perfused brain slice preparation. It is the first to report NMR imaging studies of isolated perfused brain slices. It reports high resolution NMR microimages of isolated hippocampal slices with anatomic architecture discernable at 15 μm resolution. Subsequently this model was utilized to analyze the mechanisms, which underlie diffusion changes that might be seen under various neuropathologies. Initial experiments showed that with adequate perfusion the slices could be maintained for physiologically relevant studies. Preliminary work following 20% tonicity challenges indicated that diffusion weighted NMR imaging was sensitive to these changes. Later, quantitative diffusion measurements revealed a bi-exponential water diffusion behavior in the slices with fast and slow diffusing components. Furthermore, after ouabain blockade of the Na+/K+ ATPase and NMDA excitotoxicity, there was a significant change in the relative sizes of the water compartments but the individual apparent diffusion coefficients remained constant. The change in compartment sizes is consistent with cytotoxic edema seen following ischemic stroke or ouabain and NMDA induced toxicity. Experiments using gadodiamide enhanced NMR imaging provided another way to measure cell volume sizes. Following a hypertonic perturbation, the changes observed with gadodiamide enhanced imaging were consistent with those measured with diffusion NMR. Experiments on heart slices also revealed bi-exponential water diffusion. These experiments provide added confidence that the fast and slow diffusing components represent true physiological water compartments. Finally, *in vivo* experiments using middle cerebral artery (MCA) occlusion show decreases in water ADC following ischemia which may be explained mechanistically by compartmental water shifts as measured in the perfused slice preparation. Furthermore, unpublished preliminary data in our laboratory suggest that bi-exponential water diffusion can be seen in MCA occluded animals with compartmental changes similar to that in the hippocampal slice. Together the data is consistent with ADC measurements in the clinical setting.

These results may be discussed in light of the 4 mechanisms that have been postulated to explain ADC changes following an acute ischemic stroke. The data collected herein is most consistent with the postulate that water redistribution during ischemia plays an important role in the observed ADC changes clinically. In this model the ADC decrease following ischemia is attributed to cytotoxic edema resulting from water shifting from the faster diffusing extracellular matrix into the slower diffusing intracellular compartment and thus, the average ADC decreases (Benveniste et al., 1992). The model of water redistribution would therefore predict that the individual intra and extracellular ADCs do not change during an ischemic insult but that the fractional volumes would change which is what we see in our experiments with ouabain and NMDA. Preliminary studies with MCA occlusion also support this hypothesis. A second explanation states that cytotoxic edema results in a decrease in the extracellular compartmental volume, restricting diffusion such that extracellular water ADC decreases (Norris et al., 1994a); although this may be true we were not able to measure a change in ADC therefore, at least in our model this is not the major contributor to diffusion changes. A third mechanism proposed is that ischemia decreases cell membrane permeability to water, leading a decrease in ADC. Our experiments and other evidence indicate that membrane permeability changes alone are unlikely to explain the observed changes in ADC (Latour et al., 1994; Szafer et al., 1995b). A fourth mechanism is that ischemia leads to a reduction in intracellular water ADC because of a decrease in active cell streaming or an increase in cellular viscosity (Neil et al., 1996). Recent NMR spectroscopic studies of compartment specific tracer molecules suggest that their extracellular and intracellular ADCs are similar and both decrease with ischemia (Duong et al., 1998; Neil et al., 1996). Our study indicates that water ADCs do not change in the same manner. Since most of the tracer molecules used have a molecular weight many times that of water and they usually have a large hydration sphere, it is likely that their diffusion behavior is different than that of water.

In short this work describes development of a perfused tissue preparation for NMR imaging studies which have yield information regarding tissue water diffusion behavior and may shed light on ADC changes observed clinically. We anticipate that further studies with the brain slice model will contribute to the development of quantitative models that in turn will support the examination of a variety of neurological disease states both experimentally and clinically.

REFERENCES

Aitken PG, Breese GR, Dudek FF, Edwards F, Espanol MT, Larkman PM, Lipton P, Newman GC, Nowak TSJ, Panizzon KL (1995) Preparative methods for brain slices: a discussion. J.Neurosci.Methods 59:139-149

Andrew ER (1956) Nuclear Magnetic Resonance. Cambridge University Press, Cambridge

Asahi M, Hoshimaru M, Uemura Y, Tokime T, Kojima M, Ohtsuka T, Matsuura N, Aoki T, Shibahara K, Kikuchi H. (1997) Expression of interleukin-1 beta converting enzyme gene family and bcl-2 gene family in the rat brain following permanent occlusion of the middle cerebral artery. J Cereb Blood Flow Metab. 1997 17(1): 11-8.

Assaf Y, Cohen Y (1996) Detection of different water populations in brain-tissue using ^{2}H single- and double-quantum-filtered diffusion NMR spectroscopy. J.Magn.Reson.B. 112:151-159

Bachelard H, Badargoffer R, Morris P, Thatcher N (1994) Magnetic resonance spectroscopy studies on Ca2+, Zn2+ and energy metabolism in superfused brain slices. Biochem.Soc.Trans. 22:988-991

Barsky D, Putz B, Schulten K (1997) Theory of heterogeneous relaxation in compartmentalized tissues. Magn.Reson.Med. 37:666-675

Behl C, Skutella T, Lezoualc'h F, Post A, Widmann M, Newton CJ, Holsboer F (1997). Neuroprotection against oxidative stress by estrogens: structure-activity relationship. Mol Pharmacol. 51(4):535-41.

Benveniste H, Hedlund LW, Johnson GA (1992) Mechanism of detection of acute cerebral ischemia in rats by diffusion weighted magnetic resonance microscopy. Stroke 23:746-754

Bernard, Claude (1865) Introduction à L'étude de la Médecine Expérimentale. Baillière Paris

Blackband SJ, Bui JD, Buckley DL, Zelles T, Plant HD, Inglis BA, Phillips MI (1997) MR microscopy of perfused brain slices. Magn.Reson.Med. 38:1012-1015

Bloch F, Hansen WW, Packard M (1946) The nuclear induction experiment. Phys.Rev. 70: 474-485

Bottomley PA (1988) Frequency Dependence of Tissue Relaxation Times. In: Partain CL, Price RR, Patton JA, et al (eds) Magnetic Resonance Imaging. W.B. Saunders, Philadelphia, pp 1075-1098

Bottomley PA, Hardy CJ, Argersinger RE, Allen-Moore G (1987) A review of 1H nuclear magnetic resonance relaxation in pathology: are T1 and T2 diagnostic? Med.Phys. 14:1-37

Braunschweiger PG, Schiffer L, Furmanski P (1986) The measurement of extracellular water volumes in tissues by gadolinium modification of 1H-NMR spin lattice (T1) relaxation. Magn.Reson.Imaging 4:285-291

Buckley DL, Bui JD, Phillips MI, Zelles T, Inglis BA, Plant HD, Blackband SJ (1999) The effect of ouabain on water diffusion in the rat hippocampal slice measured by high resolution NMR imaging. Magn.Reson.Med. 41:137-142

Bui JD, Buckley DL, Phillips MI, Blackband SJ (1998a) Quantitating functional responses of hippocampal slices to NMDA recpetor stimulation using high-resolution NMR imaging. Int.Soc.Magn.Res.Med.6th Annual Meeting (Abstract)

Bui JD, Buckley DL, Phillips MI, Blackband SJ (1998b) Studies of perfused brain slices with MR microscopy. In: Blümler P, Blümich B, Botto RE, et al (eds) Spatially resolved magnetic resonance. Wiley-VCH, Weinheim, pp. 337-44

Bui JD, Buckley DL, Phillips MI, Blackband SJ (1999) Nuclear magnetic resonance imaging measurements of water diffusion in the perfused hippocampal slice during N-methyl-D-aspartate-induced excitotoxicity. Neuroscience. 93(2):487-90

Chan PH (1996) Role of oxidants in ischemic brain damage. Stroke 27, 1124-1129

Choi DW (1990) Cerebral hypoxia: Some new approaches and unanswered questions. J Neurosci 10, 2493-2501

Choi DW, Rothman SM (1990) The role of glutamate neurotoxicity in hypoxic-ischemic neuronal death. Annu.Rev.Neurosci. 13:171-182

Clayden NJ, Hesler BD (1992) Multiexponential analysis of relaxation decays. J.Magn.Reson. 98:271-282

Collingridge GL (1995) The brain slice preparation: a tribute to the pioneer Henry McIlwain. J.Neurosci.Methods 59:5-9

Damadian R (1971) Tumor detection by nuclear magnetic resonance. Science 171:1151-1153

del Zoppo GJ, Schmid-Schonbein GW, Mori E, Copeland BR, Chang CM. (1991) Polymorphonuclear leukocytes occlude capillaries following middle cerebral artery occlusion and reperfusion in baboons. Stroke 22(10):1276-83.

del Zoppo GJ, Wagner S, Tagaya M (1997) Trends and future developments in the pharmacological treatment of acute ischaemic stroke. Drugs 54:9-38

Donahue KM, Burstein D, Manning WJ, Gray ML (1994) Studies of Gd-DTPA relaxivity and proton-exchange rates in tissue. Magn.Reson.Med. 32:66-76

Donahue KM, Weisskoff RM, Parmelee DJ, Callahan RJ, Wilkinson RA, Mandeville JB, Rosen BR (1995) Dynamic Gd-DTPA enhanced MRI measurement of tissue cell-volume fraction. Magn.Reson.Med. 34:423-432

Dubal DB, Kashon ML, Pettigrew LC, Ren JM, Finklestein SP, Rau SW, Wise PM. (1998) Estradiol protects against ischemic injury. J Cereb Blood Flow Metab. 18(11):1253-8.

Duong TQ, Ackerman JJ, Ying HS, Neil JJ (1998) Evaluation of extra- and intracellular apparent diffusion in normal and globally ischemic rat brain via 19F NMR. Magn.Reson.Med. 40:1-13

Garrido L, Wedeen VJ, Kwong KK, Spencer UM, Kantor HL (1994) Anisotropy of water diffusion in the myocardium of the rat. Circ.Res. 74:789-793

Green PS, Gridley KE, Simpkins JW. (1998) Nuclear estrogen receptor-independent neuroprotection by estratrienes: a novel interaction with glutathione. Neuroscience. 84(1):7-10

Hahn EL. (1950). Spin Echoes. Phys. Rev. 80(4):580-94

Hazlewood CF, Chang DC, Nichols BL, Woessner DE (1974) Nuclear magnetic resonance transverse relaxation times of water protons in skeletal muscle. Biophys.J. 14:583-606

Helpern JA, Ordidge RJ, Knight RA (1992) The effect of cell membrane water permeability on the apparent diffusion coefficient of water Proc.Soc.Magn.Reson.Med. 1201-1201(Abstract)

Henkelman RM, Stanisz GJ, Kim JK, Bronskill MJ (1994) Anisotropy of NMR properties of tissues. Magn.Reson.Med. 32:592-601

Hille B (1992) Ionic Channels of Excitable Membranes. Sinauer. Sunderland, MA pp 170-201.

Lehre KP, Levy LM, Ottersen OP, Storm-Mathisen J, Danbolt NC. (1995) Differential expression of two glial glutamate transporters in the rat brain: quantitative and immunocytochemical observations. J Neurosci. 15(3Pt1):1835-53.

Hosokawa T, Bliss TV, Fine A (1994) Quantitative three-dimensional confocal microscopy of synaptic structures in living brain tissue. Microsc.Res.Tech. 29:290-296

Hossmann KA (1974) Development and resolution of ischemic brain swelling. In Pappius HM and Feindel W (eds) Dynamics of Brain Edema Springer-Verlag, Heidelberg. pp 219-227

Hsu EW, Aiken NR, Blackband SJ (1996) Nuclear magnetic resonance microscopy of single neurons under hypotonic perturbation. Am J.Physiol.Cell Physiology 40:C1895-C1900

Hsu EW, Muzikant AL, Matulevicius SA, Penland RC, Henriquez CS (1998) Magnetic resonance myocardial fiber-orientation mapping with direct histological correlation. Am.J.Physiol. 274:H1627-H1634

Hsu EW, Xue R, Holmes A, Forder JR (1998) Delayed reduction of tissue water diffusion after myocardial ischemia. Am.J.Physiol. 275:H697-H702

Huang R, Somjen GG (1995) The effect of graded hypertonia on interstitial volume, tissue resistance and synaptic transmission in rat hippocampal tissue slices. Brain Res. 702:181-187

Joo F (1987) A unifying concept on the pathogenesis of brain oedemas. Neuropathol.Appl.Neurobiol. 13:161-176

Karger J, Pfeifer H, Heink W (1988) Principles and application of self-diffusion measurements by nuclear magnetic resonance. Adv.Magn.Reson. 12:1-89

Katz B (1966) Nerve, Muscle and Synapse. McGraw-Hill, New York

Krizaj D, Rice ME, Wardle RA, Nicholson C (1996) Water compartmentalization and extracellular tortuosity after osmotic changes in cerebellum of *Trachemys scripta*. J.Physiol.(Lond) 492:887-896

Larcombe-McDouall JB, Seo Y, Steward MC (1994) Continuous measurement of cell volume changes in perfused rat salivary glands by proton NMR. Magn.Reson.Med. 31:131-138

Lascola CD, Kraig RP (1997) Astrocyte reaction in global ischemic brain injury. In Primer on Cerebrovascular Diseases (Welsh M, Caplan L, Siesjo B, Weir B and Reis DJ, eds.), San Diego, CA, Academic, pp 114-117.

Latour LL, Svoboda K, Mitra PP, Sotak CH (1994) Time-dependent diffusion of water in a biological model system. Proc.Natl.Acad.Sci.USA 91:1229-1233

Lauterbur PC (1973) Image formation by induced local interactions: examples employing nuclear magnetic resonance. Nature 242:190-191

Le Bihan D, Delannoy J, Levin RL (1989) Temperature mapping with MR imaging of molecular diffusion: application to hyperthermia. Radiology 171:853-857

Li JG, Stanisz GJ, Henkelman RM (1998) Integrated analysis of diffusion and relaxation of water in blood. Magn.Reson.Med. 40:79-88

Lipton P, Aitken PG, Dudek FE, Eskessen K, Espanol MT, Ferchmin PA, Kelly JB, Kreisman NR, Landfield PW, Larkman PM (1995) Making the best of brain slices: comparing preparative methods. J.Neurosci.Methods 59:151-156

Macdonald RL and Stoodley M. (1998) Pathophysiology of cerebral ischemia. Neurol Med Chir (Tokyo). 38(1):1-11. Review

MacManus JP, Hill IE, Preston E, Rasquinha I, Walker T, Buchan AM. (1995) Differences in DNA fragmentation following transient cerebral or decapitation ischemia in rats. J Cereb Blood Flow Metab. 1995 15(5):728-37.

Mansfield P (1977) Multi-planar image formation using NMR spin echoes. J.Phys.C: Solid State Phys. 10:L55-L58

Mansfield P, Grannell PK (1973) NMR diffraction in solids. J.Phys.C: Solid State Phys. 6:L422-L426

Marini AM, Spiga G, Mocchetti I (1997) Toward the development of strategies to prevent ischemic neuronal injury. In vitro studies. Ann.N.Y.Acad.Sci. 825:209-219

Marquardt DW (1963) An Algorithm for Least-Squares Estimation of Nonlinear Parameters. J.Soc.Ind.Appl.Math. 11:431-441

Martin DL and Shain W (1979) High affinity transport of taurine and beta-alanine and low affinity transport of gamma-aminobutyric acid by a single transport system in cultured glioma cells. J Biol Chem. 254(15):7076-84.

McIlwain, H., Buchel, L., and Chesire, J. D. (1951) The inorganic phosphate and phosphocreatine of brain espcially during metabolism in vitro. J.Biochem. 48, 12-20.

Mermelstein PG, Becker JB, Surmeier DJ. (1996) Estradiol reduces calcium currents in rat neostriatal neurons via a membrane receptor. J Neurosci. 15;16(2):595-604.

Mohr JP, Clap LR, Melski JW, Goldstein RJ, Duncan GW, Kistler JP, Pessin MS, Bleich HL (1978). The Harvard Cooperative Stroke Registry: a prospective registry. Neurology 28, 754-762

Moseley ME, Butts K, Yenari MA, Marks M, de Crespigny A (1995) Clinical aspects of DWI. NMR Biomed. 8:387-396

Moseley ME, Cohen Y, Mintorovitch J, Chileuitt L, Shimizu H, Kucharczyk J, Wendland MF, Weinstein PR (1990) Early detection of regional cerebral ischemia in cats: comparison of diffusion and T2-weighted MRI and spectroscopy. Magn.Reson.Med. 14:330-346

Mulkern RV, Gudbjartsson H, Westin CF, Zengingonul HP, Gartner W, Guttmann CRG, Robertson RL, Kyriakos W, Schwartz R, Holtzman D, Jolesz FA, Maier SE (1999) Multi-component apparent diffusion coefficients in human brain. NMR Biomed. 12:51-62

Neeman M, Freyer JP, Sillerud LO (1990) Pulsed gradient spin echo diffusion studies in NMR imaging: effects of the imaging gradients on the determination of diffusion coefficients. J.Magn.Reson. 90:303-312

Neil JJ, Duong TQ, Ackerman JJ (1996) Evaluation of intracellular diffusion in normal and globally-ischemic rat brain via 133Cs NMR. Magn.Reson.Med. 35:329-335

Newman GC, Hospod FE, Qi H, Patel H (1995) Effects of dextran on hippocampal brain slice water, extracellular- space, calcium kinetics and histology. J.Neurosci.Meth. 61:33-46

Nicholson C and Sykova E (1998) Extracellular space structure revealed by diffusion analysis. Trends Neurosci. 21:207-215

Niendorf T, Dijkhuizen RM, Norris DG, Campagne MV, Nicolay K (1996) Biexponential diffusion attenuation in various states of brain- tissue - implications for diffusion-weighted imaging. Magn.Reson.Med. 36:847-857

Niendorf T, Norris DG, Leibfritz D (1994) Detection of apparent restricted diffusion in healthy rat brain at short diffusion times. Magn.Reson.Med. 32:672-677

Normann PT, Hals PA (1995) In vivo stability and excretion of gadodiamide (GdDTPA-BMA), a hydrophilic gadolinium complex used as a contrast enhancing agent for magnetic resonance imaging. Eur.J.Drug Metab.Pharm. 20:307-313

Norris DG, Niendorf T, Leibfritz D (1994) Healthy and infarcted brain-tissues studied at short diffusion times - the origins of apparent restriction and the reduction in apparent diffusion-coefficient. NMR Biomed. 7:304-310

Olivetti G, Ricci R, Lagrasta C, Maniga E, Sonnenblick EH, Anversa P (1988) Cellular basis of wall remodeling in long-term pressure overload- induced right ventricular hypertrophy in rats. Circ.Res. 63:648-657

Olivetti L, White RD (1990) Evaluation of myocardial function with magnetic resonance imaging. Imaging strategies and state of the art. Radiol.Med.(Torino.) 79:663-673

Olson JE, Sankar R, Holtzman D, James A, Fleischhacker D. (1986) Energy-dependent volume regulation in primary cultured cerebral astrocytes. J Cell Physiol. 128(2):209-15.

Palovcik RA, Phillips MI (1986b) A biphasic excitatory response of hippocampal neurons to gonadotropin releasing hormone. Neuroendocrinology 44:137-141

Palovcik RA, Phillips MI (1986a) A constant perfusion slice chamber for stable recording during the addition of drugs. J.Neurosci.Meth. 17:129-139

Pauli W (1924) The theoretical significance of the satellites of some spectral lines and the effect on them of magnetic fields. Naturwissenschaften 12:741-743

Pérez-Pinzón MA, Tao L, Nicholson C (1995) Extracellular potassium, volume fraction, and tortuosity in rat hippocampal CA1, CA3, and cortical slices during ischemia. J.Neurophysiol. 74:565-573

Pfeuffer J, Flogel U, Dreher W, Leibfritz D (1998) Restricted diffusion and exchange of intracellular water: theoretical modelling and diffusion time dependence of H-1 NMR measurements on perfused glial cells. NMR Biomed. 11:19-31

Pilatus U, Shim H, Artemov D, Davis D, van Zijl PCM, Glickson JD (1997) Intracellular volume and apparent diffusion constants of perfused cancer cell cultures, as measured by NMR. Magn.Reson.Med. 37:825-832

Pirkle JL, Ashley DL, Goldstein JH (1979) Pulse nuclear magnetic resonance measurements of water exchange across the erythrocyte membrane employing a low Mn concentration. Biophys J. 25:389-406

Pirttila TM, Kauppinen RA (1994) Regulation of intracellular pH in guinea pig cerebral cortex ex-vivo studied by P-31 and H-1 nuclear magnetic resonance spectroscopy: role of extracellular bicarbonate and chloride. J.Neurochem. 62:656-664

Purcell EM, Torrey HC, Pound RV (1946) Resonance absorbtion by nuclear magnetic moments in a solid. Phys.Rev. 69:37-38

Rabi II, Millman S, Kusch P, Zacharias JR (1939) The molecular beam resonance method for measuring nuclear magnetic moments. The magnetic moments of $_3Li^6$, $_3Li^7$ and $_9F^{19}$. Phys.Rev. 55:526-535

Schilling L, Wahl M (1997) Brain edema: pathogenesis and therapy. Kidney Int.Suppl. 59:S69-75

Schoeniger JS, Aiken N, Hsu E, Blackband SJ (1994) Relaxation-time and diffusion NMR microscopy of single neurons. J.Magn.Reson.B. 103:261-273

Scollan DF, Holmes A, Winslow R, Forder J (1998) Histological validation of myocardial microstructure obtained from diffusion tensor magnetic resonance imaging. Am.J.Physiol. 275:H2308-H2318

Shi J, Zhang YQ, Simpkins JW. (1997) Effects of 17beta-estradiol on glucose transporter 1 expression and endothelial cell survival following focal ischemia in the rats. Exp Brain Res. 117(2):200-6.

Silver B, Weber J, Fisher M (1996) Medical therapy for ischemic stroke. Clin.Neuropharmacol. 19:101-128

Simpkins JW, Rajakumar G, Zhang YQ, Simpkins CE, Greenwald D, Yu CJ, Bodor N, Day AL. (1997) Estrogens may reduce mortality and ischemic damage caused by middle cerebral artery occlusion in the female rat. J Neurosurg. 87(5):724-30

Slichter CP (1989) Principles of magnetic resonance. Springer-Verlag, Berlin

Small DL, Buchan AM (1997) NMDA antagonists: their role in neuroprotection. Int.Rev.Neurobiol. 40:137-171

Sohrabji F, Greene LA, Miranda RC, Toran-Allerand CD. (1994) Reciprocal regulation of estrogen and NGF receptors by their ligands in PC12 cells. J Neurobiol. 25(8):974-88.

Stanisz GJ, Szafer A, Wright GA, Henkelman RM (1997) An analytical model of restricted diffusion in bovine optic nerve. Magn.Reson.Med. 37:103-111

Stejskal EO, Tanner JE (1965) Spin diffusion measurements: spin echoes in the presence of a time-dependent field gradient. J.Chem.Phys. 42:288-292

Szafer A, Zhong JH, Anderson AW, Gore JC (1995a) Diffusion weighted imaging in tissues: theoretical models. NMR Biomed. 8:289-296

Szafer A, Zhong J, Gore JC (1995b) Theoretical model for water diffusion in tissues. Magn.Reson.Med. 33:697-712

Ting YT, Degani H (1993) Energetics and glucose metabolism in hippocampal slices during depolarization: P-31 and C-13 NMR studies. Brain Res. 610:16-23

Toung TJ, Traystman RJ, Hurn PD. (1998) Estrogen-mediated neuroprotection after experimental stroke in male rats. Stroke. 29(8):1666-70.

van der Toorn A, Sykova E, Dijkhuizen RM, Vorisek I, Vargova L, Skobisova E, Campagne MVL, Reese T, Nicolay K (1996) Dynamic changes in water ADC, energy metabolism, extracellular space volume, and tortuosity in neonatal rat brain during global ischemia. Magn.Reson.Med. 36:52-60

van Gelderen P, de Vleeschouwer MHM, DesPres D, Pekar J, van Zijl PCM, Moonen CTW (1994) Water diffusion and acute stroke. Magn.Reson.Med. 31:154-163

Van Harreveld A and Fifkova E. (1971) Light- and electron-microscopic changes in central nervous tissue after electrophoretic injection of glutamate. Exp Mol Pathol. 15(1):61-81.

van Zijl PCM, Moonen CTW, Faustino P, Pekar J, Kaplan O, Cohen JS (1991) Complete separation of intracellular and extracellular information in NMR spectra of perfused cells by diffusion- weighted spectroscopy. Proc.Natl.Acad.Sci.USA 88:3228-3232

Verheul B, Balazs R, van der Sprenkel JWB, Tulleken CAF, Nicolay K, Tamminga KS, Campagne MV (1994) Comparison of diffusion-weighted MRI with changes in cell volume in a rat model of brain injury. NMR Biomed. 7:96-100

Yongbi MN, Ding SJ, Dunn JF (1996) A modified sub-second fast STEAM sequence incorporating bipolar gradients for *in vivo* diffusion imaging. Magn.Reson.Med. 35:911-916

Curriculum Vitae

Jonathan D. Bui
Born: 2nd March 1972
E-mail: jdbui@ufbi.ufl.edu

Education

The University of Florida College of Liberal Arts & Sciences	Associate of Arts 1992 University Honors Program
The University of Florida College of Liberal Arts & Sciences Department of Biochemistry & Molecular Biology	BS (Highest Honors) 1994 Biophysical Chemistry & Molecular Biology
The University of Florida College of Liberal Arts & Sciences Department of Zoology	BS (Highest Honors) 1994 Zoology
The University of Florida College of Medicine Department of Physiology	PhD* 1994-2000 Physiology & Biophysics (NMR imaging and Neurophysiology)
The University of Florida College of Medicine	MD* (Honors) 1994-2001

*UF MD/PhD Program

Awards and Honors

1990	Presidential Honor Roll (4.0 GPA)
1991	Exceptional Honors Trophy (4.0 GPA)
1993	President's Spring Recognition for Outstanding Students
1993	Zoology Honor Award
1993	Outstanding Undergraduate Research Award
1994	American Heart Association Summer Research Fellowship
1994	M.D./Ph.D. Fellowship, UF MD/PhD Program
1995	NIH Medical Student Summer Research Fellowship
1996	American Heart Association Medical Student Research Fellowship
1996	National Dean's List
1997	ISMRM Student Travel Award, Vancouver Meeting
1997	American Heart Association Predoctoral Fellowship (2 year grant)
1998*	ISMRM Student Travel Award, Sydney Meeting (*could not accept)
1999	ISMRM Student Travel Award, Philadelphia Meeting

Society Memberships

The International Society for Magnetic Resonance in Medicine
The American Physiological Society
The American Physical Society
The Society for Neuroscience
The American Medical Association

Publications

1. **Bui JD**, Kimura B, Phillips MI. Losartan potassium, a nonpeptide antagonist of angiotensin II, chronically administered p.o. does not readily cross the blood brain barrier. Eur.J.Pharmacol. 1992;219(1):147-51.
2. Blackband SJ, **Bui JD**, Buckley DL, Zelles T, Plant HD, Inglis BA, Phillips MI. MR microscopy of perfused brain slices. Magn.Reson.Med. 1997;38(6):1012-5.
3. Wu P, Phillips MI, **Bui J**, Terwilliger EF . Adeno-associated virus vector-mediated transgene integration into neurons and other nondividing cell targets. J.Virol. 1998;72(7):5919-26.
4. **Bui JD**, Buckley DL, Phillips MI, Blackband, SJ. In Spatially resolved magnetic resonance. (Blümler P, Blümich B, Botto RE, Fukushima E, editors) Weinheim: Wiley-VCH; 1998; 30, Studies of perfused brain slices with MR microscopy. pp. 337-44.
5. Buckley DL, **Bui JD**, Phillips MI, Zelles T , Inglis BA, Plant HD, Blackband SJ. The effect of ouabain on water diffusion in the rat hippocampal slice measured by high resolution NMR imaging. Magn.Reson.Med. 1999; 41:137-142
6. **Bui JD**, Nammari DR, Buckley DL, Inglis BA, Silver XS, Mareci TH, Phillips MI. In vivo dynamics and distribution of intracerebroventricularly administered gadodiamide, visualized by magnetic resonance imaging. Neuroscience. 1999; 90(3):1115-22.
7. **Bui JD**, Buckley DL, Phillips MI, Blackband SJ (1999) Nuclear magnetic resonance imaging measurements of water diffusion in the perfused hippocampal slice during N-methyl-D-aspartate-induced excitotoxicity. Neuroscience. 93(2):487-90
8. **Bui JD**, Zelles T, Lou HJ, Gallion VL, Phillips MI, Tan W. Probing intracellular dynamics in living cells with near-field optics. J Neurosci Methods. 1999; 89(1):9-15.
9. Buckley DL, **Bui JD**, Phillips MI, Blackband SJ. MRI measurement of cell volume fraction in the perfused rat hippocampal slice. Magn Reson Med. 1999 42(3):603-7
10. Blackband SJ, Buckley DL, **Bui JD**, Phillips MI. NMR microscopy--beginnings and new directions. MAGMA. 1999; 9(3):112-6
11. Zhang YC, **Bui JD**, Shen L, Phillips MI. Antisense inhibition of beta(1)-adrenergic receptor mRNA in a single dose produces a profound and prolonged reduction in high blood pressure in spontaneously hypertensive rats. Circulation. 2000;101(6):682-8.
12. Shi J, **Bui JD**, Yang SH, Lucas TH, Buckley DL, Blackband SJ, King MA, Day AL, and Simpkins JW, Estrogens decrease reperfusion-associated cortical ischemic damage: an MRI analysis in a transient focal ischemia model, Stroke accepted with revision.

Letters

Bui, JD "Medical Scientist Training Program," Gubernaculum 2000. University of Florida College of Medicine 1995

Theses

Bui JD Regulation of gene expression of the renin-angiotensin system by antisense oligonucleotides, Undergraduate thesis in Biochemistry & Molecular Biology with Highest Honors, The University of Florida, 1994.

Bui JD Losartan potassium, a nonpeptide antagonist of angiotensin II, chronically administered p.o. does not readily cross the blood-brain barrier. Undergraduate thesis in Zoology with Highest Honors, The University of Florida, 1994.

Abstracts

Bui, J.D. and Phillips, M.I. Losartan potassium, a non-peptide antagonist of angiotensin II, chronically administered p.o. does not readily cross the blood-brain barrier, *FASEB J.* 6(5), #5413, 1992.

Phillips, M.I., Gyurko, R., Bui, J.D., Sernia, C. and Wielbo, D. Uptake and stability of angiotensin receptor type-1 mRNA antisense oligonucleotides studied by laser scanning confocal microscopy, *Hypertension* 24(3)378, 1994.

Bui, J.D., Zelles, T., Buckley, D.L., Plant, H.D., Inglis, B.A., Phillips, M.I. and Blackband, S.J., NMR microscopy of perfused brain slices, International Society for Magnetic Resonance in Medicine 5th Annual Meeting, Vancouver, April 1997.

Bui, J.D., Inglis, B.A., Nammari, D.R., Silver, X.S., Mercer, E., Toffolo, S., Phillips, M.I. and Mareci, T.H. Visualization of neuronal activation after chemical stimulation of the brain using fMRI, International Society for Magnetic Resonance in Medicine 5th Annual Meeting, Vancouver, April 1997.

Bui, J.D., Buckley, D.L., Zelles, T., Plant, H.D., Inglis, B.A., Phillips, M.I. and Blackband, S.J. "MR microscopy of osmotically perturbed hippocampal slices", Society for Neuroscience 27th Annual Meeting, New Orleans, October 1997.

Nammari, D.R., Bui, J.D., Inglis, Silver, X.S., Mercer, E.,Phillips, Mareci, T.H., and Phillips, M.I. "fMRI of direct neuronal activation by NMDA in rat brain in vivo." Society for Neuroscience 27th Annual Meeting, New Orleans, October 1997.

Wu P., Bui J., Phillips M.I., Terwilliger E.F., Adeno-Associated Virus Vector-Mediated Transgene Integration into rat brain, Society for Neuroscience 27th Annual Meeting, New Orleans, October 1997.

Bui, J.D., Zelles, T., Buckley, D.L., Plant, H.D., Inglis, B.A., Phillips, M.I. and Blackband, S.J. "Osmotic Stress in perfused brain slices visualised by MR microscopy." South East Nerve Net Conference March 1997

Nammari, D.R., Bui, J.D., Inglis, B.A., Silver, X.S., Bossart E.L, Mareci, T.H., and Phillips, M.I. "In vivo kinetics and distribution of a chemical injected intracerebroventricularly visualized by Gd-DTPA MR imaging." South East Nerve Net Conference March 1997

Gallion, V.L., Bui, J.D., Zelles, T., Phillips, M.I., and Tan, W. Utilizing a near field optical probe for detection of intracellular [Ca2+] in single cells." South East Nerve Net Conference March 1997

Bui, J.D., Buckley, D.L., Phillips, M.I. and Blackband, S.J., The effect of ouabain on water diffusion in the rat hippocampal slice measured by high resolution NMR imaging, British Chapter of the ISMRM Annual Meeting, Manchester, December 1997.

Blackband, S.J., Bui, J.D., Buckley, D.L., and Phillips, M.I., Neurochemically induced signal changes in MR microimaging studies of perfused brain slices, 39th Experimental NMR Conference, Asilomar, March 1998.

Bui, J.D., Buckley, D.L., Phillips, M.I. and Blackband, S.J., Quantitating functional responses of hippocampal slices to NMDA receptor stimulation using high resolution NMR imaging, International Society for Magnetic Resonance in Medicine 6th Annual Meeting, Sydney, April 1998.

Buckley, D.L., Bui, J.D., Phillips, M.I., Zelles, T., Inglis, B.A., Plant, H.D., and Blackband, S.J., The effect of ouabain on water diffusion in the rat hippocampal slice measured by high resolution NMR imaging, International Society for Magnetic Resonance in Medicine 6th Annual Meeting, Sydney, April 1998.

Bui, J.D., Buckley, D.L., Phillips, M.I. and Blackband, S.J., High resolution NMR imaging of NMDA receptor stimulation in perfused hippocampal slices, Society for Neuroscience 28th Annual Meeting, Los Angeles, November 1998.

Bui JD, Buckley DL, Blackband SJ, Forder JR, Biexponential Diffusion Observed in Myocardial Tissue Slices, International Society for Magnetic Resonance in Medicine 7th Annual Meeting, Philadelphia, April 1999. (oral)

Bui JD, Shi J, Yang SH, Lucas TH, Buckley DL, King MA, Day AL, Simpkins JW, Blackband SJ NMR imaging of the neuroprotective effects of estrogen. International Society for Magnetic Resonance in Medicine 7th Annual Meeting, Philadephia, April 1999.

Buckley DL, Bui JD, Phillips MI, Blackband SJ. MRI measurement of cell volume fraction in the perfused rat hippocampal slice. International Society for Magnetic Resonance in Medicine 7th Annual Meeting, Philadelphia, April 1999.

Mohr CM, Bui JD, Jones HC, Blackband SJ ^{1}H MRS and quantitative MRI of the pathophysiology of neonatal rat hydrocephalus. International Society for Magnetic Resonance in Medicine 7th Annual Meeting, Philadelphia, April 1999.

Submitted Manuscripts

1. Forder JR, **Bui JD**, Buckley DL, Blackband SJ. MR Imaging Measurement of Compartmental Water Diffusion in Perfused Heart Slices. Submitted to Amer. J. Physiol
2. Mohr CM, **Bui JD**, Blackband SJ, Jones HC Changes in T_2 with brain maturation in normal and hydrocephalic H-Tx rat pups. Submitted to Magn Reson Med
3. Hsu EW, Buckley DL, **Bui JD**, Blackband SJ, Forder JR Two-Compartment Diffusion Tensor MRI of Isolated Perfused Hearts. Submitted to Magn Reson Med

BIOGRAPHICAL SKETCH

Jonathan Dzung Bui was born in Vietnam during the war and spent the first 6 years in Hue. He escaped via boat to Macau along with his family some twenty years ago where they lived for a year in a refugee camp. When his family came to the sates, JD went to first and second grade in Lancaster, Pennsylvania. He then finished grade school in Rosemead, California. Subsequently, he went to junior high and high school in Vancouver, Washington for 5 years; subsequently he finished his last year of high school in Auburndale, Florida. JD came here to the University of Florida as an undergraduate in 1990 and has been here since. He hopes to carry on with research.

I certify that I have read this study and that in my opinion it conforms to acceptable standards of scholarly presentation and is fully adequate, in scope and quality, as a dissertation for the degree of Doctor of Philosophy.

M Ian Phillips

M. Ian Phillips, Chair
Professor of Physiology

I certify that I have read this study and that in my opinion it conforms to acceptable standards of scholarly presentation and is fully adequate, in scope and quality, as a dissertation for the degree of Doctor of Philosophy.

Stephen J. Blackband, Cochair
Associate Professor of Neuroscience

I certify that I have read this study and that in my opinion it conforms to acceptable standards of scholarly presentation and is fully adequate, in scope and quality, as a dissertation for the degree of Doctor of Philosophy.

Thomas H. Mareci

Thomas H. Mareci
Associate Professor of Biochemistry
and Molecular Biology

I certify that I have read this study and that in my opinion it conforms to acceptable standards of scholarly presentation and is fully adequate, in scope and quality, as a dissertation for the degree of Doctor of Philosophy.

Edwin M. Meyer
Associate Professor of Pharmacology
and Therapeutics

I certify that I have read this study and that in my opinion it conforms to acceptable standards of scholarly presentation and is fully adequate, in scope and quality, as a dissertation for the degree of Doctor of Philosophy.

Colin Sumners
Professor of Physiology

This dissertation was submitted to the Graduate Faculty of the College of Medicine and to the Graduate School and was accepted as partial fulfillment of the requirements for the degree of Doctor of Philosophy.

August 2000

Dean, College of Medicine

Winfred M Phillips

Dean, Graduate School